Clathrin-mediated Endocytosis with Cell Confinement and during Neutrophil Polarization

by

Xinyu Tan

A dissertation submitted in partial fulfillment
of the requirements for the degree of
Doctor of Philosophy
(Mechanical Engineering)
in The University of Michigan
2018

Doctoral Committee:

Assistant Professor Allen P. Liu, Chair
Associate Professor Jianping Fu
Assistant Professor Indika Rajapakse
Assistant Professor Qiong Yang

Xinyu Tan

xinyutan@umich.edu

ORCID iD: 0000-0003-3733-5683

ACKNOWLEDGEMENTS

First, I would like to express my gratitude to my advisor Prof. Allen Liu for his continuous support and help. I thank Allen for this great opportunity to study and work at University of Michigan and for introducing me to cell biology. Allen has been very supportive in my research and other aspects of life, giving me a lot of freedom to explore what I want to do.

I would like to thank my committee members, for their insightful comments and encouragement. I also want to thank my fellow labmates for their friendship, stimulating discussions and memorable moments. I am blessed to join two student groups, Michigan Data Science Team and Michigan Student Artificial Intelligence Lab. They not only taught me many computational and analytical skills but also the integrity as a knowledge worker. Their guidance and friendship make the past two years tremendously more fun and open many doors for my life. I would like to thank my friends for their support, many deep discussions about career and life, and encouragement. Graduate school in a foreign country sometimes can be really hard, and it is they who have helped me through many difficult times and have shaped who I am today to some degree. I am extremely thankful for Prof. Edgar Meyhofer, who patiently taught me to be honest with my heart and to see a better side of life. Lastly, I want to thank my parents, Zhengkun Tan and Qingyue Wang, and my sister, Xinrui Tan, for their unfailing support and love.

TABLE OF CONTENTS

LIST OF FIGURES

Figure

LIST OF APPENDICES

Appendix

LIST OF ABBREVIATIONS

CME clathrin-mediated endocytosis

CCP clathrin-coated pit

CCS clathrin-coated structure

CCV clathrin-coated vesicle

RPE retinal pigment epithelial

eGFP-CLCa enhanced green fluorescent protein clathrin light chain a

AP2 adaptor protein 2

PDMS polydimethoxysiloxane

TIRF total internal reflection fluorescence

TIR-FM total internal reflection fluorescence microscopy

PBS phosphate buffered saline

fMLP N-formylmethionyl-leucyl-phenylalanine

FPR formyl peptide receptors

GPCR G protein-coupled receptor

GRK G-protein-coupled receptor kinase

EPS15 epidermal growth factor receptor pathway substrate 15

EGFR epidermal growth factor receptor

EGF epidermal growth factor

EHD3 Eps15 homology (EH) domain-containing protein 3

ABSTRACT

Clathrin-mediated endocytosis (CME) is one of the major pathway through which cells internalize nutrients and membrane proteins. It occurs on the membrane via clathrin-coated pits (CCPs). In this thesis, we studied CCPs' behavior when cells are under spatial constraints. In the first two projects, the constraint was applied using micro-contact printing. CCPs presented differential phenotypes on different-sized but the same shaped cells. In particular, CCPs were smaller with larger spreading area. We further showed that this might be due to the higher cortical tension associated with large spreading area. Seeding cells on anisotropic fibronectin patterns, we were able to manipulate where and how long CCPs appear on the cell. Together, these results showed that CCPs' distribution and behavior are regulated by mechanical cues in a cell.

In the last project, HL-60 differentiated neutrophils were used as the experimental system. They undergo rapid polarization in the presence of N-formylmethionyl-leucyl-phenylalanine (fMLP), during which cells not only present anisotropic morphology but also have asymetric distribution of cellular structures and signaling molecules. We found that CCPs did not have as polarized distribution upon the stimulation of fMLP, but they revealed differential interation with formyl peptitde recepter, actin, and β-arrestin with and without fMLP. Disruption of CME blocked effective neutrophil polarization as well as major signaling pathways. The results suggest a regulatory role of CME in neutrophil polarization.

CHAPTER I

Introduction

1.1 Endocytosis

Plasma membrane is the barrier that separates the cell and their environment. It is mainly made of phospholipids, which provide the flexibility and semi-permeability of plasma membrane. Flexibility ensures that cells can adapt to the environment rapidly without too much damage, be it passing narrow passage like capillaries or experiencing a sudden external force. Due to the amphipathicity of lipid bilayer, without any other structure or mechanisms, only limited number of molecules can pass membrane freely driven by simple diffusion. The passive and unregulated mechanism is not sufficient for effective transport required by the cell. Indeed, many small molecules, like ions, glucose, and water, have their dedicated channel proteins or carrier proteins to ensure regulated and efficient transport. Even though dedicated channels and carrier proteins solved the non-specificity and efficiency problems from simple diffusion, there exists limitations:

1. Nutrients uptake through channels may not be efficient
2. Some cargoes, like hormones, require more sophisticated interaction with cells
3. These channel proteins and other membrane proteins also need to be regulated on the membrane

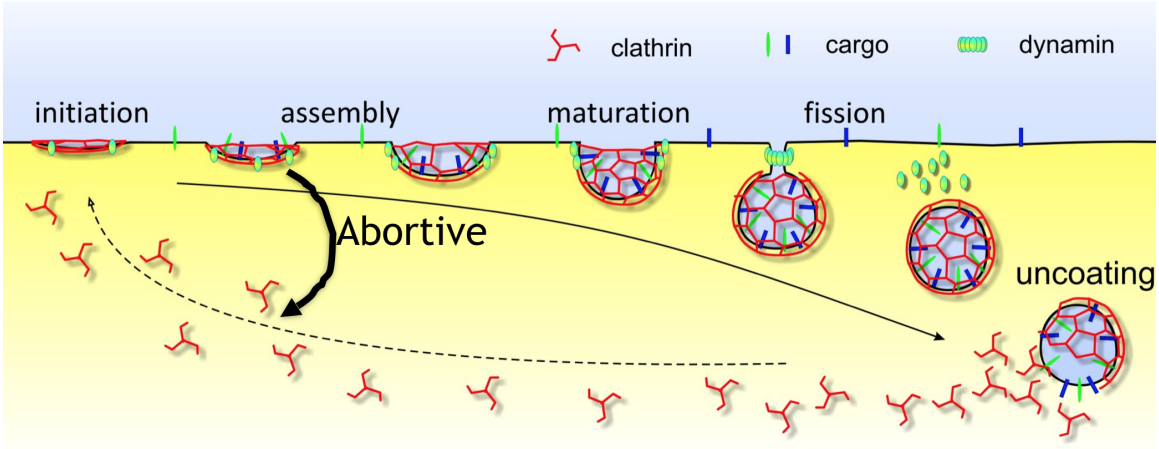

Figure 1.1: Schematic of CCP's life cycle.

Endocytosis provides a larger spectrum of regulated portals of entry into the cells (*Conner and Schmid*, 2003) and overcomes the limitations mentioned above. Depending on the cargo type and cell types, endocytosis occurs through multiple mechanisms, but all of them follow a similar process: part of membrane invaginates into a pit-like structure, following by getting pinched off to form a vesicle and then entering into cytosol (*Doherty and McMahon*, 2009). Among all of the endocytic pathways, clathrin-mediated endocytosis (CME) is the best studied. CME occurs via its fundamental unit, CCP, a macro-molecular machineary that assembles and disassembles timely. Its simplified life cycle is illustrated in Figure 1.1. Briefly, it is initiated by a clustering of clathrin and other adaptor proteins, grows by recruiting more endocytic proteins, gets pinched off into cytosol with the help of dynamin, and eventually releases the coated proteins and goes on to endosome pathway (*Conner and Schmid*, 2003). As indicated in Figure 1.1, sometimes CCPs don't finish the complete cycle, aborting at the early stages. There are hundreds to thousands of CCPs on the cell membrane, all of which are different from each other. It is a by nature stochastic process, yet highly regulated. This process will be discussed in detail in the next section.

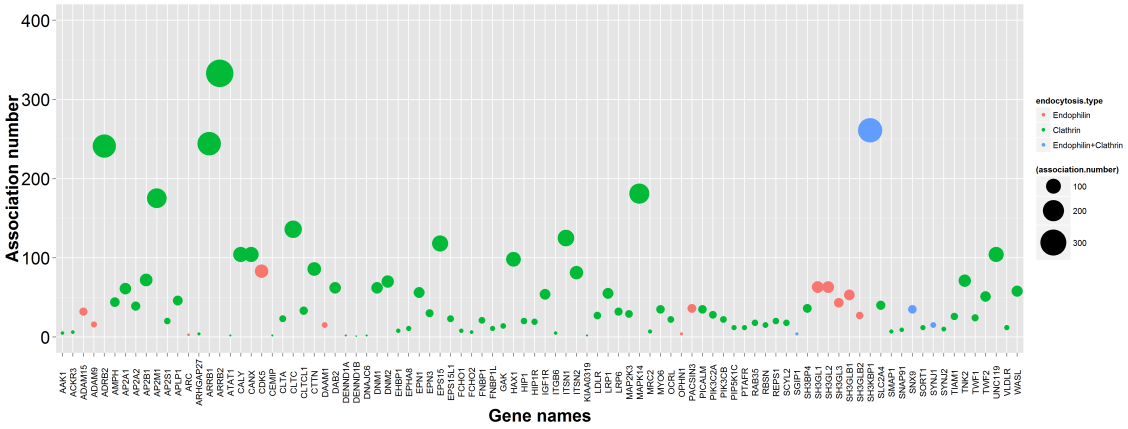

Figure 1.2: Most active clathrin associated proteins. Data was scraped from BioGrid websete *Stark et al.* (2006). Association number denotes the number of types of proteins the corresponding protein interacts with. The plot was created on 07-01-2015, subject to change.

1.1.1 Molecular Machinary and CCP dynamics

By comparing the protein components of clathrin-coated vesicle (CCV) fraction in control cells and cells with silenced clathrin-heavy chain using mass spectrometry, *Borner et al.* (2006) have identified 63 bona fide CCV-associated proteins. Using curated protein-protein interaction database BioGrid (*Stark et al.*, 2006) that condensed decades of biomedical research, we also identified the most active clathrin-associated proteins (Figure 1.2). Among these proteins, we observed that β-arrestin 1/2 were among the most active proteins, indicating that they are crucial in downstream cellular events. The same technique can be used to created a huge CME protein-protein interaction network.

However, viewing CCV as a complicated protein mass or just one dimension protein-protein interaction is too simple a picture. As mentioned above, CME is a regulated dynamical process. Proteins are recruited in a timely manner, yet even within the same cell, none of the CCPs are identical.

To understand the role of each protein and their relationships in CME, at a high level, we relied on three major advances in science and technology: first, molecular

biology that allows us to perturb the process in a targeted manner; second, advances in microscopy to measure CME with unprecedented spatial and temporal resolution; third, improved algorithms to detect weak signal faithfully and be able to summarize the microscopic data into meaningful metrics. With these tools, we have established a relatively detailed picture of CME down to molecular level (*McMahon and Boucrot*, 2011), and instead of having one single central computing unit, we found several protein "hubs" that act as the guiding points for the process.

The first unbiased measurement of CCPs within a cell was possible thanks to the development of a robust tracking algorithm (*Jaqaman et al.*, 2008). Using this technique, *Loerke et al.* (2009) identified that cargo was not a key rate limiting factor of CME; instead, by expressing dysfunctional mutants or overexpressing widetype dynamin, it was found that the lifetime of CCPs can be modulated in either direction. This study, the combination of high-resoluted microscopy, robust computational analysis and molecular perturbation, marked an important experimental paradigm in studying CME, having an strong influence on many later studies. Using a similar experimental platform, the same group identified several endocytic accessory proteins and proposed the checkpoint model, in which each CCP's life cycle was monitored by a set of proteins; their heterogeneous lifetimes might be due to the differential recruitment of these "checkpoint" proteins.

It was once thought that clathrin is the initiator of CCP. However, *Henne et al.* (2010) found that prior to the appearance of clathrin, F-BARcontaining protein family FCHo1/2 [Fer/Cip4 homology domain-only (FCHo) proteins 1 and 2] defined where a CCP will form, and thus is considered to be the nucleators of CME. Using even more intricate analysis, *Cocucci et al.* (2012) pinpointed the first 5 seconds in the life of a CCP; they observed that all CCPs initiate by coordinating one clathrin triskelion and two AP2 molecules or sometimes two clathrin triskelion and four AP2 complexes. The process of CCPs forming CCVs was not clear, in particular the role of actin in

the process. Actin was found not required for mammalian cells' CME but essential for yeast endocytosis; however, actin is known as force generator, then how would CCP's invagination, the process that greatly deforms the membrane, does not require actin? *Boulant et al.* (2011) provided an unified explanation that in the cells with high tension, like yeast, actin is indeed needed; in mammalian cells where the tension is relatively low, then actin is dispensable. However, the interation between dynamin and actin remained incompletely understood. *Grassart et al.* (2014) utilized genome editing and quantitative microscopy with single-molecule sensitivity and determined that at the early stage of CCPs dynamin recruitment presents greater heterogeneity, but to the last 20 seconds of life cycle, most CCPs recruit about 26 dynamin molecules.

These studies have characterized CCPs' behavior from within - they perturbed CME by knocking out its major or accessory components and observed how these perturbation changed CCPs' phenotypes. However, CME connects outside world and brings in ligands and receptors. CME is a constitutive process, regardless of ligand binding to the receptor. However, does cargo affect CME at all?

Loerke et al. (2009) found that cargo is not the rate limiting factor of CME; a increase of 40 folds of transferrin receptor on the cell membrane only led to a slight decrease in lifetime and a two-fold increase in maturation efficiency. By changing the organization of receptor, *Liu et al.* (2010) were able to manipulate CCP's behavior in a more delicate way. Specifically, using biotinylated transferrin receptor and heterotetrameric streptavidin to control the clustering of transferrin receptor, *Liu et al.* (2010) found that receptor clustering promotes CCP initiation and the uptake of corresponding ligand, transferrin in this case.

Using mammalian cells as model systems, we have answered many questions to CCP's behavior. It was shown that knockout of AP2 was embryonic lethal in mouse, suggesting that CME is essential in organism development and growth (*Mitsunari et al.*, 2005). Then, what is the phenotype of CME in living organisms? Using a

novel data analysis technique that does not rely on a complete lifespan of CCPs, *Ferguson et al.* (2016) characterized the CCP dynamics in *Drosophila* amnioserosa; they found that CCP dynamics slows down during the dorsal closure of *Drosophila* embryos (*Ferguson et al.*, 2016).

1.1.2 Physiological Function

In addition to cell eating and drinking, CME is responsible for removing the receptors and their ligands from the plasma membrane and thereby for signal termination. More and more studies have shown that CME is involved much more actively in signal transduction. There are two major types of regulation:

1. The rich and heterogeneous composition of CCPs provides a scaffold for signal transduction

2. CME is a highly dynamic process. From initiation, which forms CCPs on the plasma membrane, to invagination, which generates endosomes entering into cytosol, it offers several layers of regulation.

Many CME components not only help to build CCPs, but also relay the signal from ligand binding to downstream effectors. For example, β-arrestin is one of best studied dual-function proteins (*Luttrell and Lefkowitz*, 2002). It was first discovered as a protein that desensitizes G protein-coupled receptor (GPCR) signaling by binding to the the phosphorylated GPCR from G-protein-coupled receptor kinase (GRK) and thereby end the signaling from G proteins effectors (*Lohse et al.*, 1992; *Lefkowitz*, 1993). Not until 1996 did two groups identify that β-arrestin recruits some GPCRs such as β_2-adrenergic recpetors to CCPs as an adaptor protein (*Goodman et al.*, 1996; *Ferguson et al.*, 1996) and leads to endocytosis of GPCR. However, more than damping the interaction between receptor and G proteins, β-arrestins are important signal transduers. First, they recruit Src family kinases to GPCRs. This recruitment

is essential in phosphorylation of dynamin (*Miller et al.*, 2000), MAPK signaling (*Luttrell et al.*, 1999; *Eichel et al.*, 2016) and neutrophil degranulation (*Barlic et al.*, 2000).

Similarly, epidermal growth factor receptor pathway substrate 15 (EPS15) was found to be the core scaffold protein in CCP that binds to AP2. Microinjection of EPS15 antibody to inhibit its function or knockdown of both EPS15 and EPS15R also blocked epidermal growth factor receptor (EGFR) and transferrin receptor internalization (*Carbone et al.*, 1997; *Huang et al.*, 2004), indicating the essential role of EPS15 in CME. Recently, *Amessou et al.* (2016) found that Eps15 homology (EH) domain-containing protein 3 (EHD3) as a potential brain tumor suppressor. In particular, EHD3 promotes EGFR's degradation by a increase in its ubiquitination and by diverting it from recycling endosome pathways (*Amessou et al.*, 2016).

β-arrestin and EPS15 are examples of the first type of effects of CME on signaling, i.e., many of the CME accessory proteins act as signal transducers beyond the building blocks of CCP. As we discussed, CME occurs through CCPs, which dynamically initiate and then invaginate as the start of endocytic pathway. There are more evidences showing that the temporal and spatial regulation aspects are important in signaling pathways.

CCPs concentrate cargoes and receptors and stay on the plasma membrane as they mature, providing a platform for certain signaling pathways. For example, inhibition of clathrin heavy chain and intersectin 2 decreased signaling of Janus Kinase 2 activated by ligand binding to GM-CSF receptor, whereas dominant-negative mutant of dynamin which prevents CCP to invaginate promotes the signaling (*Chen et al.*, 2012a). Similarly, clathrin heavy chain rather than dynamin is responsible for epidermal growth factor (EGF)-stimulated Gab1 and Akt phosphorylation (*Garay et al.*, 2015). Most CCPs' lifetime are around 1 min to 10 min, but there exists another type of clathrin structure, flat clathrin lattices. It was shown by super-resolution mi-

croscopy that these long-lived and large patch of clathrin structures lead to sustained recruitment of certain type of receptors and are important for signaling (*Grove et al.*, 2014; *Leyton-Puig et al.*, 2017).

Then, we can't help but to ask: except for attenuating the signal from the plasma, what is the significance of internalization? CME is the start of bigger endosomal pathway, which determines the fate of cargos and also provides a special signaling platform.

Instead of contributing to degradation of EGFR, *Sigismund et al.* (2008) found that EGFRs internalized through CME go through recycling, which allows a cell to replace the receptors on the membrane, and CME is essential for prolonged signaling. Their conclusions were mainly from bulk measurement such as Western blot or static microscopy. Using multi-color live cell imaging, *Lakadamyali et al.* (2006) characterized the endosome sorting process; they observed two dynamically distinct populations of early endosomes, one moving fast along microtubules and maturing rapidly to late endosomes that leads to receptor or cargo degration, another maturing more slowly in which the receptors recycles, and this sorting starts from plasma membrane aided by CME accessory protein AP2 (*Lakadamyali et al.*, 2006).

Just as CCPs on the plasma membrane that concentrate the cargos and thus are important signaling platforms, another important role of endosomes is as dynamic scaffolds for signal transduction. The endocytic vesicles, as they travel from plasma membrane into cytosol, changes their lipid composition, in particular, phosphoinositides. CCPs on the membrane are enriched in PtdIns(4,5)P_2, but after pinching off the plasma membrane, they increase PtdIns(3)P composition (*Pálfy et al.*, 2012). Different phosphoinositides bind to different group of proteins (*Di Paolo and De Camilli*, 2006), and thereby endocytic and endosomal pathways together provide the spatial regulation of signaling. For example, PtdIns(3)P is responsible for converting APPL endosomes to s early endosomal antigen positive endosomes, and thereby damps the

EGFR signaling as APPL enhances EGFR's signaling (*Zoncu et al.*, 2009).

1.2 Motivation and Dissertation Outline

As discussed above, we see that there are two lines of CME research in recent years - one focuses on characterizing the phenotype of CME, another on function. The initial studies in the field have focused more on the molecular composition and their dynamical behaviors. Not until recently, with the advancement of perturbation techniques and observation tools, has the field started to look at the functional aspect of CME and CCPs and to connect their phenotype to its function. It was shown that GPCRs are internalized through a subset of CCPs, which delay in dynamin recruitment and undergo abortion before successful internalization (*Puthenveedu and von Zastrow*, 2006).More recently, *Rosselli-Murai et al.* (2017) observed the similar subsets of CCPs for EGFR, which colocalize with phosphatase tensin homolog that increases the PtdIns(3,4,5)P_3 and thereby contributes to the shortened lifetime of CCPs. These mechanistic studies have advanced our understanding not only just to CME, but also to a systematic view of cell biology.

However, molecular compositions and biochemical environments are not the whole picture of a cell. Cells constantly experience and exert forces from and to their environment and each other. With the development of technology, we are able to manipulate the physical environment and measure the force at a cellular scale, and thereby to understand the mechanical aspects of the cell (*Liu et al.*, 2017). It has been revealed that mechanical forces are just like biochemical factors, with the ability to regulate cell behavior. Many proteins, cellular structures, and pathways have been found to be involved in the process, namely, mechanotransuction. (*Mammoto et al.*, 2013; *Kim et al.*, 2009; *Eyckmans et al.*, 2011; *Iskratsch et al.*, 2014; *Dupont et al.*, 2011)

CME occurs at the membrane that directly interacts with outside environment.

The formation and maturation of CCPs require dramatic deformation of the membrane, which has to overcome membrane tension. However, as we discussed earlier, most of the CME studies focus on the molecular composition and functional sides. Therefore, we would like to ask whether physical environment or stimuli can alter the CME behavior as well.

Compared to 15 years ago (*Conner and Schmid*, 2003), we have accumulated many evidence showing that CME is more than "cell drinking and eating", by understanding how stimulated receptors are internalized and how endocytosis affects the signal transduction. This "bottom-up" methodology, that solves the whole problem from simpler and smaller ones, make the original problem more tractable and helps us to distill the essence of cellular design. However, none of the proteins, or structures, or pathways are isolated in a cell. Neutrophil chemotaxis, describing neutrophils' ability to move towards the chemoattractant, can best illustrate this point. When stimulated by fMLP, neutrophil quickly changes its morphology and activates its motility mechanism. All these start from fMLP binding to formyl peptide receptors (FPR). Most studies have been focused on the downstream effectors and signaling pathways, but few on the other aspect of ligand binding, i.e., inducing CME.

Therefore, this thesis aims to answer two questions:

1. How does CCP respond to physical constraints?

2. What role does CME play in neutrophil polarization?

The rest of the thesis is organized as following. In Chapter II and III, we aim to answer the first question with the combination of micro-contact printing and live-cell total internal reflection fluorescence microscopy (TIR-FM). Specifically, in Chapter II, we patterned three sized cells and started by examining the cytoskeleton and adhesion structure. Next, we quantified CCP dynamics from TIR-FM images using quantitative image analysis. CCPs presented differential phenotypes on different-sized

but the same shaped cells. In particular, CCPs were smaller with larger spreading area. We further showed that this might be due to the higher cortical tension associated with large spreading area. In Chapter III, by seeding cells on anisotropic fibronectin patterns, we were able to manipulate where and how long CCPs appear on the cell. Together, these results showed that CCPs' distribution and behavior are regulated by mechanical cues in a cell.

In Chapter IV, HL-60 differentiated neutrophils were used as the experimental system. They undergo rapid polarization in the presence of N-formylmethionyl-leucyl-phenylalanine (fMLP), during which cells not only present anisotropic morphology but also have asymetric distribution of cellular structures and signaling molecules. We found that CCPs do not have as polarized distribution upon the stimulation of fMLP, but they revealed differential interation with formyl peptitde recepter, actin, and β-arrestin with and without fMLP. Disruption of CME blocked effective neutrophil polarization as well as major signaling pathways. The results suggest a regulatory role of CME in neutrophil polarization.

CHAPTER II

Cell Spreading Area Regulates CCP Dynamics

2.1 Introduction

For a long time, our understanding of cells is to think of them as a complex chemical system. They are made from well organized macro-molecules, and live in a liquid biochemical world, with signaling molecules and nutrients flowing around. Hence, many studies focused on investigations of various macro-molecules, understanding their properties and interactions between each other, and how cells respond to biochemical signals. In the past few decades, with the advances in biophyiscal and molecular technologies that allow us to manipulate cell's physical micro-environment, we started to understand the importance of mechanical force in cell function, differentiation, development, physiology and disease.

Cells experience all kinds of physical forces or constraints in their natural environment: different tissues have different stiffnesses, and all healthy cells tightly regulate their size and shape. A pioneering study using different elastic matrices showed that mesenchymal stem cells commit to different cell lineage in response to the tissue-level elasticity (*Engler et al.*, 2006). Specifically, soft substrates that mimic brain tissue are neurogenic, whereas stiff ones myogenic. *Chen et al.* (1997) and *McBeath et al.* (2004) demonstrated that cell size controls viability as well as determines the fate of mesenchymal stem cells to adipocyte or osteoblast.

Over the years, investigators have identified many structures and molecular mechanisms that allow the cells to sense the forces. Hair cells in our ear utilizes ion channels to transduce sound to neural signals (*Corey et al.*, 2004). In migrating cells, focal adhesions, which link the extracellular matrix to cytoskeleton, were found to be the key player of transudcing physical forces to cellular behaviors (*Hayakawa et al.*, 2012).

Membrane trafficking occurs at the plasma membrane, the physical barrier between physical environment and enclosed cytosol. It is expected that physical forces could modulate trafficking events, i.e., endocytosis and exocytosis. During cell spreading, a burst of exocytosis, which releases a large portion of the membrane, is activated due to the sudden increase in membrane tension (*Gauthier et al.*, 2011). During mitosis, when cell exhibits very high tension, transferrin uptake through CME was inhibited (*Warren et al.*, 1984). A more recent study further showed that caveolae, which are functional units of caveolae-mediated endocytosis, rapidly disassemble upon acute mechanical stress such as hypo-osmotic shock or uniaxial stretching, which both increase membrane tension (*Sinha et al.*, 2011).

CME, the best studied endocytic pathway, was less clear in the mechano-biology picture. First, actin, the key structure to support cell and provide forces, is essential for CME in yeast but not in mammalian cells (*Kaksonen et al.*, 2005). This remains elusive until *Boulant et al.* (2011) discovered that actin is required for CME only when membrane tension is high. Second, unlike caveolae or other mechanical sensors such as focal adhesion (*Shao et al.*, 2013), CCPs do not present the sudden response to the tension change (*Sinha et al.*, 2011).

However, using a subcellular-sized pattern of extracellular matrix proteins to control the spatial organization of focal adhesions, *Liu et al.* (2009) previously found that CCP lifetimes were significantly longer in the patterned regions that had higher cortical actin density. Subcellular patterning controls focal adhesion assembly and organization and in effect generates an atypical cytoskeletal phenotype. Reduction

of cortical actin abolished the increase in CCP lifetime, suggesting that the observed CCP lifetime changes could be controlled by cell morphology on these subcellular patterned substrates. The atypical cytoskeleton structure likely has a strong effect on the traction stresses exerted on the substrate and hence produced the local effects that were observed. This also indicates that CCP's response to physical forces is subtler that requires careful quantification.

Hence, to study CCPs' response to mechanical force at cellular level, more specifically, how cell morphology alters CCPs phenotype, we employed micro-contact printing of cell sized pattern to control the cell shape. Combining this microfabrication tool with live-cell imaging and quantitative image analysis, we examined three aspects of CCP properties: lifetime distribution, initiation density, and CCP fluorescence intensity. As these properties change with time, we call them CCP dynamics. We found that cells with larger spreading areas had more short-lived CCPs and a decrease in the maximum CCP fluorescence intensity. Furthermore, we showed that actin depolymerization and inhibition of myosin contractility increased the maximum CCP fluorescence intensity. These results reveal a novel facet of how resting cell size, and the associated actin cortical network, can regulate CCP dynamics.

2.2 Experimental Methods

2.2.1 Cell lines and antibodies

We used RPE cells as a model system to study CCP dynamics. RPE cells stably expressing eGFP-CLCa was generated by infection with retrovirus in a pMIEG3 vector followed by FACS sorting (*Liu et al.*, 2009). Cells were maintained in Dulbeccos Modified Eagle Medium with nutrient mixture F-12 (DMEM/F-12; GIBCO, Grand Island, NY) supplemented with 10% (v/v) fetal bovine serum (FBS) (Sigma, St. Louis, MO) and 2.5% (v/v) penicillin/ streptomycin (Invitrogen, Grand Island,

NY) at 37 °C and 5% CO2.

Anti-paxillin and all secondary antibodies were used at a dilution of 1:1000 (Invitrogen), anti-YAP was used at a dilution of 1:200 (Cell Signaling Technology, Danvers, MA), and anti- alpha adaptin (AP6) for AP2 was used at a dilution of 3:1000 (Abcam, Cambridge, MA).

2.2.2 Micro-contact printing

Standard soft lithography techniques were used to create the silicon master mold from which polydimethoxysiloxane (PDMS) stamps were made. PDMS stamps were prepared by mixing Sylgard-184 elastomer and curing agents (Dow Corning, Midland, MI) at a ratio of 10:1 to 20:1 (w/v), casting over the mold, and curing at 50 °C overnight. Inking solution made with 40 μg/ml 1 fibronectin (Sigma) and 20 μg/ml Alexa Flour 647 fibrinogen (Invitrogen) was added to the PDMS stamps and incubated for 1 hour at room temperature. After excess inking solution was removed and the stamp washed with deionized water and blown dry with a stream of filtered air, the stamp was placed in conformal contact with a UV-ozone treated PDMS-coated coverslip for approximately 5 s. PDMS-coated coverslips were prepared by spin-coating a layer of PDMS diluted in hexane (1:20) at 5000 rpm for 2 min, resulted in a thickness of 72 ± 14 nm (n = 4) as measured by a profilometer (*Chen et al.*, 2012b). PDMS-coated coverslips were used to promote efficient transfer of stamped proteins. After stamping was completed, the PDMS-coated coverslip was passivated with 0.1% Pluronic-F127 (Sigma) for 1 hour, washed with PBS, and kept in PBS at 4 °C for no more than 3 days before use.

2.2.3 Immnofluorescence

We first permeabilized and fixed the cells in 0.5% Triton X-100 (Sigma) and 2% paraformaldehyde (Electron Microscopy Sciences, Hatfield, PA) in PBS for 6 min

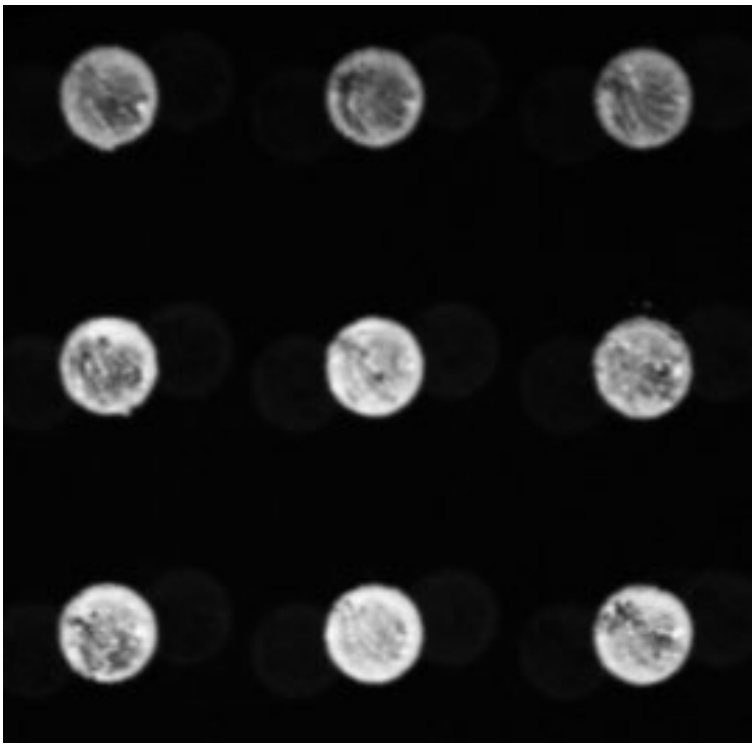

Figure 2.1: 32 µm (in radius) circular pattern.

followed by another 30 min fixation in 4% paraformaldehyde in PBS. Immunofluorescence images were taken using either an Olympus-IX81 microscope with spinning disk confocal scanner unit (CSU-X1; Yokogawa, Japan), EMCCD camera (iXon X3; Andor, South Windsor, CT), 60× objective (NA = 1.42) or an Nikon A1 confocal system mounted on a Nikon Ti2000E inverted, fluorescence microscope with DIC optics (Nikon, Japan). To quantify YAP localization, we manually classified the cells into three groups according to the contrast of nuclear to cytosol intensity of YAP and then calculated the percentage of cells with the distinct nuclear or cytosol staining for each sized cells.

2.2.4 Live cell imaging via TIRF microscopy

RPE cells expressing EGFP-CLCa were plated on microprinted surface at a low concentration and allowed to spread for 4 to 8 hours, and only individual cells that fully spread on the pattern were imaged. TIR-FM was performed on a Nikon TiE-

Perfect Focus System (PFS) microscope equipped with an Apochromat 100× objective (NA 1.49), a sCMOS camera (Flash 4.0; Hamamatsu Photonics, Japan), and a laser launch controlled by an acoustooptic tunable filter (AOTF). Cells were imaged at 2 s intervals for 10 min at 37 °C in a home-made imaging chamber consisting of the coverslip with seeded cells mounted on a slide with two strips of double-sided tape used as spacers. PDMS has an intermediate refractive index between glass and water that permitted the evanescent wave to be produced at the PDMSwater interface.23 25 nM latrunculin A (Fisher Scientific, Pitts- burg, PA) and 3 μM Y-27632 (Calbiochem, Billerica, MA) were applied to patterned cells and kept in the 37 °C incubator with 5% CO2 for 20 min before acquiring images. Imaging chamber was filled with the corresponding medium.

2.2.5 Image analysis for CCP dynamics

Image analysis was performed as described previously (*Aguet et al.*, 2013). Gaussian mixture model fitting was used to detect and localize CCPs. clathrin-coated structure (CCS) was modeled as

$$h(\mathbf{x};\mu,\sigma,A,c) = Ag(\mathbf{x};\mu,\sigma) + c + n(\mathbf{x})$$

where $\mathbf{x} = [x_1, x_2]$ are discrete pixel coordinates, A the CCS's fluoresecence amplitude, c the background and $n(\mathbf{x})$ the local noise. Specifically, we model microscope's point spread function as

$$g(\mathbf{x};\mu,\sigma) = \exp\left(-\frac{(x_1-\mu_1)^2 + (x_2-\mu_2)^2}{2\sigma^2}\right)$$

A, μ, and c were derived by solving the following optimization problem

$$\text{argmin} \sum_{\mathbf{x}\in S} \left(h(\mathbf{x};\mu,\sigma,A,c) - f(\mathbf{k}-\mathbf{x})\right)^2$$

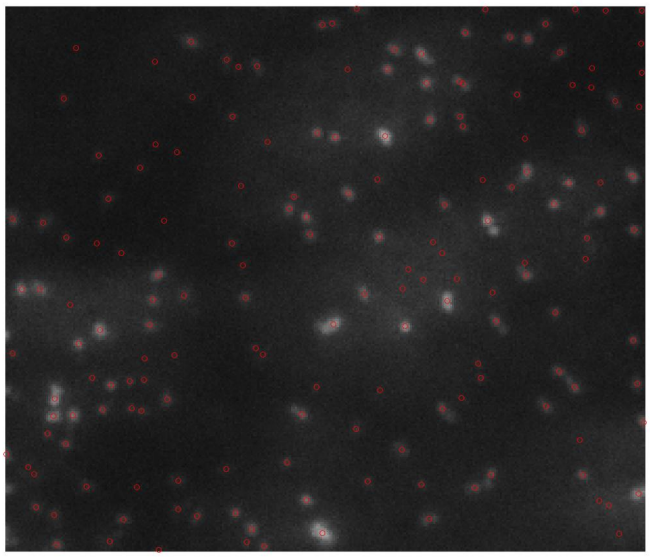

Figure 2.2: TIRF image of CCPs. CCPs were detected using Gaussian mixture and shown as red circles.

where **k** is the candidate of the CCS, yielded from the local maxima of Laplacian-of-Gaussian filtered image. The detected result is shown in Figure 2.2.

Then, CCP tracking was performed using the μ-track package with a gap-closing feature, which generates trajectories of CCPs by linking the corresponding CCPs in consecutive frames (*Jaqaman et al.*, 2008). CCPs with lifetime less than 10 s were considered as transient structures and removed from later analysis. To further filter out the transient structures on the membrane, we also removed structures whose maximum intensity was below an intensity threshold, which was set from maximum intensity in the first 6 s of all the CCPs.

From above results, we calculated three dynamic properties of CCPs: lifetime distributions, initiation density, and intensity profile. Lifetime of a CCP was calculated from the frame when it appeared to the frame it disappeared. Initiation density representing how frequent CCPs appear for a given unit area per unit time was calculated by dividing the median number of the newly appearing CCPs in each frame by the adhesive area of the cell and the interval (1/30 min). Intensity analysis

was performed as described previously (*Mettlen et al.*, 2010). CCPs were classified into six cohorts according to their lifetimes. Within each cohort, the procedure first realigned and averaged the first time point of intensity time course, yielding the appearance-aligned average. The time course was then aligned to the last time point and averaged, yielding the disappearance-aligned average. The global average was calculated as the weighted appearance and disappearance-aligned average, weighted towards appearance-aligned trace at the beginning and disappearance-aligned trace in the end. The plateau intensity was calculated as 95% of the maximum intensity values in the intensity profile of a cohort.

2.2.6 Statistical analysis

For lifetime distribution data sets, Komolgorov-Smirnov tests were performed to verify the statistical significance. For each data set, we first ran Anderson-Darling test for normality. For the data set that rejects the normality, Wilcoxon rank sum test was performed between that data set and the group which it compares with. Statistical difference of other data sets was determined by two-tailed Student's t test.

2.2.7 Quantification of static AP2 and clathrin light chain a intensity histograms

To quantify AP2 intensity histogram, alpha adaptin, a subunit of AP2, was immunostained and observed it using TIR-FM as described in above sections. MDA-MB-231 cells expressing stable mCherry-clathrin light chain a (CLCa) were generated by retroviral transduction followed by fluorescence-activated cell sorting. Cells were fixed similarly to RPE cells and imaged by TIRFM. To obtain CLCa intensity histogram, we fixed patterned EGFP-CLCa RPE cells with 4% PFA for 20 min, and then observed using an Olympus-IX81 microscope with a spinning disk confocal scanner unit. For both sets of images, the fluorescence structures were quantified using

Gaussian mixture model fitting. The MATLAB program (MathWorks, Natick, Massachusetts) is part of single particle tracking software described previously (*Jaqaman et al.*, 2008). The underlying algorithm is to iteratively fit each fluorescent structure with 2D Gaussian functions, until there is no statistical justification for adding another Gaussian function. The fluorescence intensity were extracted for all the detected structures in a group of cells with same size, and histograms with 500 bins were plotted for intensity of AP2 and 100 bins for intensity of eGFP-CLCa.

2.2.8 Micropipette aspiration and analysis

A homebuilt micropipette aspiration system with a graduated manometer was used for application of controlled suction pressure onto living cells. RPE cells were allowed to spread to patterned substrates onto 625 μm^2, 1024 μm^2, and 2500 μm^2 sized square patterns as described previously. Patterned substrates were integrated into a custom aspiration chamber and filled with culture medium. Glass micropipettes with inner diameters of 2-3 µm were filled with 0.2% bovine serum albumin (BSA) in 1X phosphate buffered saline (PBS) in order to allow smooth movement of the cell membrane inside the pipette. Negative pressure in the micropipette tip was generated by aspirating water from the manometer reservoir and increased gradually in -200 Pa increments. Nikon Advanced Modulation Contrast optics (NAMC) mounted on a Nikon Ti-S microscope and CoolSnap MYO CCD camera (Photometrics, Tucson, AZ) were used to acquire live-cell brightfield images. ImageJ (http://rsb.info.nih.gov/ij/) software was used to manually measure the pipette diameters (D_p) and plasma membrane projection length within the pipette (L_p) at 1.2 kPa negative pressure for 8-10 cells per pattern size.

2.2.9 Cell volume calculation

Z-stacks of images for micropatterned cells was acquired using an Olympus-IX81 microscope with spinning disk confocal scanner unit (CSU-X1; Yokogawa), EMCCD camera (iXon X3; Andor), 60x objective (NA = 1.42). Depending on the height of the cell, 15 to 30 sections at 0.5 µm steps were obtained. 3D reconstruction was performed using Fiji (http://fiji.sc/Fiji) to generate the y-z projection of the cell. To calculate cell volume, the areas from all the sections of a cell were integrated by stack step.

2.3 Results

2.3.1 Proportion of short-lived CCPs and initiation density increases with cell spreading area independent of cell shape

Micro-contact printing was previously used to precisely control cell shape and the extent of cell spreading (*McBeath et al.*, 2004). We employed this technique to generate cell-sized fibronectin islands onto PDMS-coated coverslip via a PDMS stamp and blocked the surrounding areas with Pluoronic F127 to prevent spreading of cells beyond the patterned areas (Figure 2.3 (A)). RPE cells stably expressing eGFP-CLCa spread on circular fibronectin islands of 625 μm^2, 1024 μm^2 and 2500 μm^2. Average RPE cells spread to about 1000 - 1200 μm^2 on unpatterned substrates, so the sizes appropriately sample both above and below the average cell spreading area.

When cells were plated on these substrates, actin stress fibers were found to localize along the circumference of the cells with focal adhesions marked by the focal adhesion protein paxillin concentrated at the periphery of the cells (Figure 2.3 (B)), forming fribrillar structures on larger cells. Actin filaments were much thicker and organized for the larger patterns (2500 μm^2), suggestive of a higher cytoskeletal stress developed in these cells similar to what was observed previously (*Tan et al.*, 2003).

CCPs, as imaged by confocal fluorescence microscopy, were found throughout the bottom surface of the cell.

To probe the dynamics of CCPs with different cell spreading areas, we combined time-lapse live cell TIRF imaging with single particle detection and tracking (*Jaqaman et al.*, 2008; *Aguet et al.*, 2013). Three dynamic properties could be obtained from these time lapse movies:

1. lifetime - defined as the time interval from CCP appearance to disappearance in the TIRF field

2. initiation density - defined as the number of CCP appearance per unit area and unit time

3. fluorescence intensity of fluorescently tagged CLCa

We first determined the CCP lifetime distribution and compared the distributions among three different sizes of patterned cells. For cells that were more spread ($2500\,\mu m^2$), there were more short-lived CCPs with lifetimes from 10 s to 18 s (Figure 2.4). It has been suggested that CCPs with short lifetimes are likely to disassemble before getting internalized and are categorized as abortive CCPs (*Ehrlich et al.*, 2004; *Loerke et al.*, 2009). Based on numerous work using a similar criterion (*Aguet et al.*, 2013; *Taylor et al.*, 2012; *Grassart et al.*, 2014; *Cocucci et al.*, 2014), we calculated the fraction of CCPs with lifetimes under 20 s for all cell areas. 29.1% of CCPs in $2500\,\mu m^2$ cells had lifetimes less than 20 s compared to 20.3% in $625\,\mu m^2$ ones (Figure 2.4 inset). Thus, in larger patterned cells, more short-lived CCPs, which presumably failed to internalize, were observed on the membrane.

We next asked whether cell spreading would alter CCP initiation. Cells on the largest pattern had an initiation frequency of $0.270\pm\ 0.065\,\mu m^2/min$ for $2500\,\mu m^2$ cells compared to the smallest pattern $0.225\pm\ 0.088\,\mu m^2/min$ for the $625\,\mu m^2$ cells (Figure 2.5).

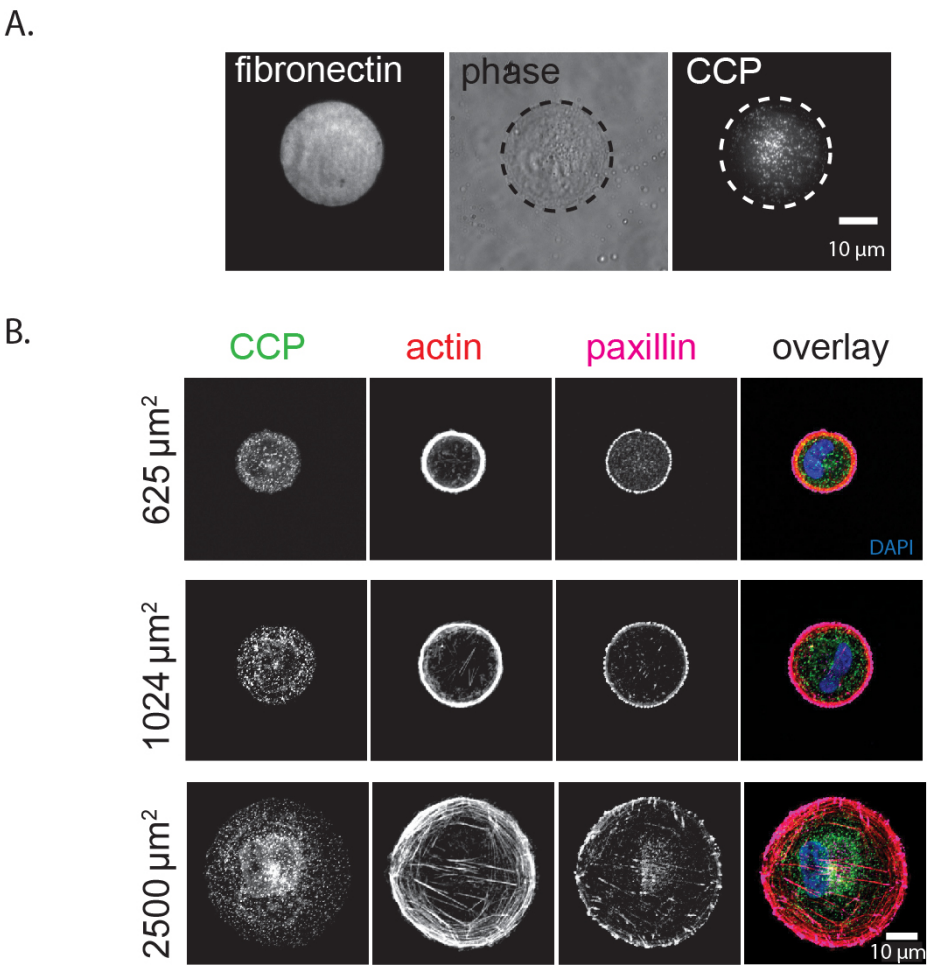

Figure 2.3: Representative RPE cells on micro-patterns. A. A eGFP-CLCa RPE cell spread on 1024 µm^2 circular fibronectin pattern (left). It is visualized using phase contrast microscopy (middle) and CCPs can be observed by TIRF microscopy (right). Dashed line highlights the outline of the cell. B. Laser scanning confocal images of CCP (green), actin (red), paxillin (magenta) and nucleus (blue) for 625 µm^2, 1024 µm^2 and 2500 µm^2 circular cells.

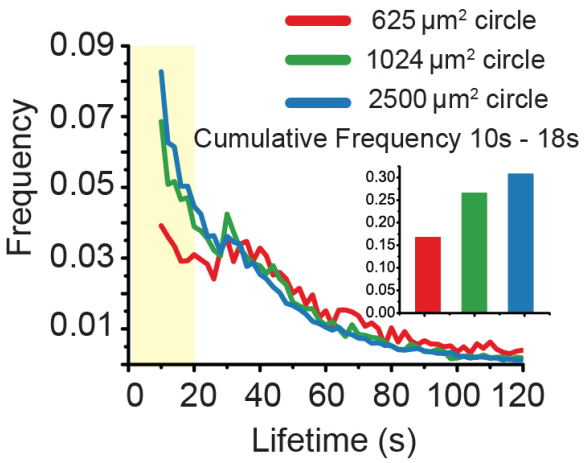

Figure 2.4: Lifetime distribution of CCP for three sized cells. Cells were imaged for 10 min, but lifetime distribution up to 120 s is plotted. Statistical significance between the distributions was confirmed using KolmogorovSmirnov test with a confidence level 0.05. Inset: Scatter plot of proportion of 1018 s CCPs of each cell for three groups. Mean ± S.D. is presented in the figure.

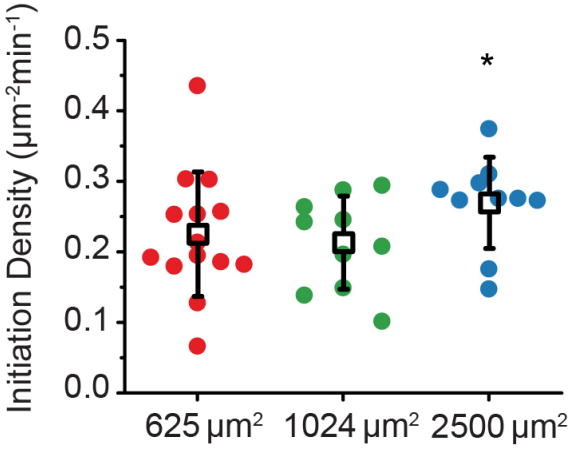

Figure 2.5: CCP initiation density for three sized cells. Scatter plot of initiation density of CCP of each cell for three sized cells (please refer to Methods section on how initiation density is calculated). Mean ± S.D. is also presented in the figure.Note in Figure 2.4 and here, N = 14, 10, 10 and N_{CCP} = 4372, 8667, 29351 for 625 µm^2, 1024 µm^2 and 2500 µm^2 circular cells respectively. Student's t test is performed between groups and p values are indicated in the figures

To test if the observed differential CCP dynamics was truly related to cell area, we also examined CCP dynamics on square fibronectin islands that had the same areas as the circular patterns (Figure 2.6 (A)). Though cells on smaller islands ($625\,\mu m^2$ and $2500\,\mu m^2$) still formed circumferential actin rings, $2500\,\mu m^2$ square cells formed distinct stress fibers (Figure 2.6 (B)). Despite the differences in actin and focal adhesion organization between circular- and square-shaped cells, CCP dynamics followed the same trends. There were more short-lived CCPs along with a higher initiation density in the largest square cells (Figure 2.6 (C) and (D)), confirming our results with circular patterned cells. This demonstrates that controlling cell spread area alone is sufficient to modulate CCP dynamics.

2.3.2 CCP fluorescence intensity is lower with larger cell spreading area due to a decreased rate of fluorescence change

To examine the effect of cell spreading on CCP intensity, we tracked the fluorescence intensity of the EGFP-tagged CLCa in CCPs imaged by TIRF microscopy over their lifetimes $625\,\mu m^2$, $1024\,\mu m^2$, $2500\,\mu m^2$ patterned cells. Due to the wide distribution of CCP lifetimes, CCPs with lifetime ranges from 20120 s were binned into six 20 s cohorts each with several thousands CCPs to obtain average trajectories in our analyses. The increase, plateau (i.e. maximum intensity), and the sudden decrease in intensity tracks of lifetime cohorts corresponded to the growth, maturation, and scission or disassembly of CCPs respectively (Fig. 3A). Comparing the three different sizes of circular cells, we found that fluorescence intensity decreased as cell spreading area increased (Fig. 3A). Average plateau intensity, which was defined as 95% level of the maximum intensity from the averaged intensities of each cohort, decreased with cell spreading in both circular and square cells (Fig. 3B). In freely spreading cells which assumes various sizes and shapes, the average plateau intensity was also lower for larger cells (Fig. 3C), consistent with our results from the patterned substrates.

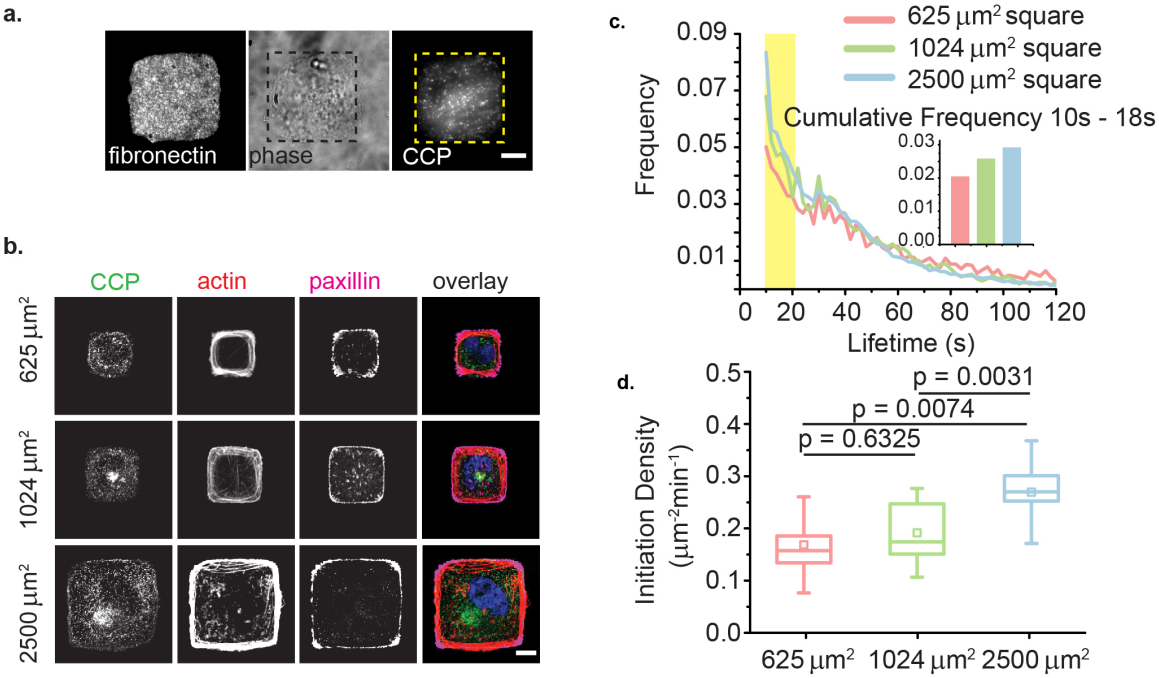

Figure 2.6: Lifetime distribution and initiation density of CCPs on three sized square cells. A. A eGFP-CLCa RPE cell spread on the 1024 µm^2 square fibronectin pattern (left), visualized by phase contrast (middle) and by TIRF microscopy for CCPs (right). Dotted lines represent outline of the cell. B. Confocal fluorescence images of CCP (green), actin (red), and paxillin (magenta) for 625 µm^2, 1024 µm^2, 2500 µm^2 square cells. C. Lifetime distribution of CCP for three sized cells. Statistical significance between the distributions was confirmed using KolmogorovSmirnov test with a confidence level 0.05. Inset: Proportion of 10 - 18 s CCPs of each cell for three groups. Mean ± S.D. is presented in the figure. D. Initiation density of CCP of each cell for three sized cells. Mean ± S.D. is presented in the figure. For (C) and (D), N = 21, 8, 10 and N_{CCP} = 7260, 5767, 32708 for 625 µm^2, 1024 µm^2, 2500 µm^2 square cells respectively. Student's t test is performed between groups and p values are indicated in the figures.

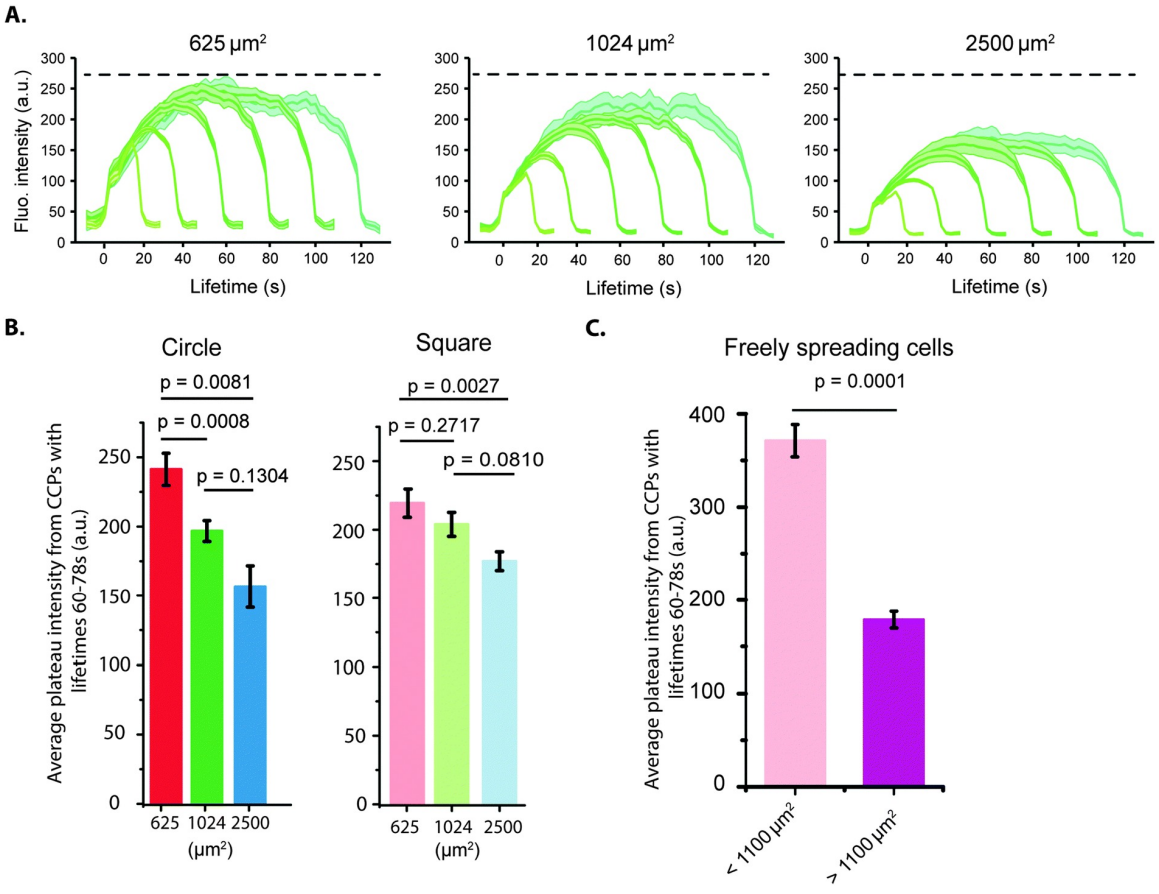

Figure 2.7: CCP intensity profile is modulated by cell spreading area. A. Average clathrin intensity traces in six lifetime cohorts (10-18, 20-38, 40-58, 60-78, 80-98, and 100-120 s) of 625 µm^2 (left), 1024 µm^2 (middle), and 2500 µm^2 (right) circular cells. Each trace is derived from all the cells in that specific group. The shaded colored bands represent the standard error. Black dashed line indicates the maximum intensity level for 625 µm^2 cells. B. Average plateau intensity of cohort 4 (60-78 s) for circular and square cells of different cell spreading area. Error bar represents standard error. N = 14, 10, 10 for 625 µm^2, 1024 µm^2, 2500 µm^2 for circular cells, N = 21, 8, 10 for 625 µm^2, 1024 µm^2, 2500 µm^2 for square cells. C. Average plateau intensity of cohort 4 for freely spreading cells, which are divided into two groups based on their size, ¡1100 µm^2 and ¿1100 µm^2. Cell numbers for two groups are 21, 25 and the number of CCPs are 9158 and 42408, respectively. Student's t test is performed between groups and p value is indicated in the figures.

To exclude the possibility that the exponential decay of the excitation field with the distance away from the glassaqueous interface in TIRF imaging affected our result, we used spinning disk confocal microscopy, which has a constant excitation power over the depth of focus (500 nm). These experiments showed the same results as with our live cell TIRF measurements and confirmed that the intensity of CCPs decreased with increasing cell spreading area in fixed cells (Figure 2.8 (A)). Since CLCa incorporation in clathrin triskelia is not critical for endocytosis (*Huang et al.*, 2004), it is possible that our results can be explained by less CLCa incorporation in CCPs in cells with larger spreading areas, while not changing the number of clathrin triskelia. By immunostaining for alpha adaptin, a subunit of the integral CCP adaptor protein AP2, we verified that AP2 intensity was also lower with increasing cell spreading area (Figure 2.8 (B)), supporting the idea that cell spreading decreases the fluorescence intensity of key endocytic components. Furthermore, we confirmed the decrease in CLCa fluorescence intensity in a different cell line with increasing cell spreading area (Figure 2.8 (C)). Together, these results show that CCP fluorescence intensity is lower with increasing the cell spreading area.

The decrease in CCP plateau intensity could arise from a slower clathrin polymerization rate or stalled clathrin polymerization at an earlier time, or a combination of the two. To differentiate between the two possibilities, the intensity profiles were examined and compared more closely. Figure 2.9 (A) showed examples of overlay of the CCP intensity trajectory averaged over all CCPs for small and large cells for three different lifetime cohorts. While the time to reach the plateau intensity did not differ significantly (Figure 2.9 (B)), the rate of CLCa intensity change was slower for cells on larger patterns (Figure 2.9 (C)), showing that larger cell areas result in slower, and likely reduced, clathrin accumulation in CCPs.

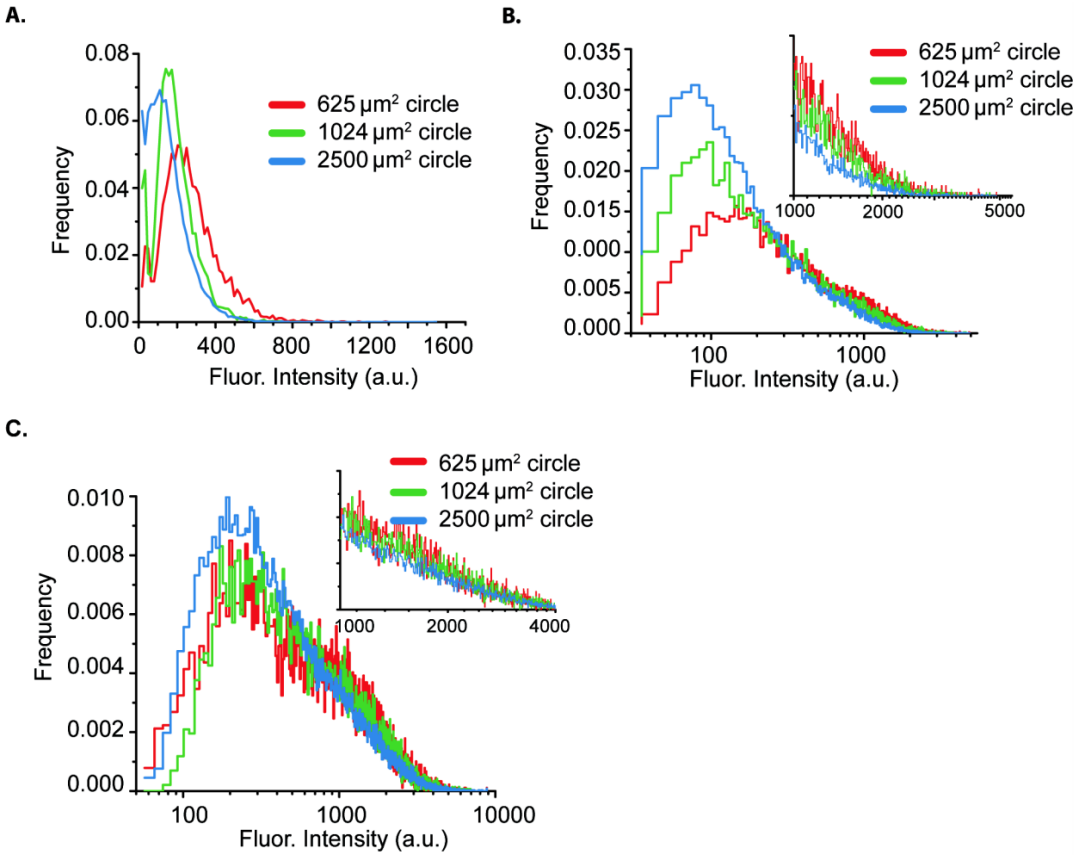

Figure 2.8: Intensity distribution of eGFP-CLCa and immunostained AP2. A. eGFP-CLCa structures were imaged by spinning disk confocal microscopy and detected in fixed cells using Gaussian mixture model fitting algorithm and plotted for their intensity distribution. B. Immunostaining of AP2 structures marked by AP6 antibodies were imaged by TIRF microscopy and detected using Gaussian mixture model fitting algorithm. C. mCherry-CLC structures were imaged by TIRF microscopy and detected in fixed cells using Gaussian mixture model fitting algorithm and plotted for their intensity distribution.

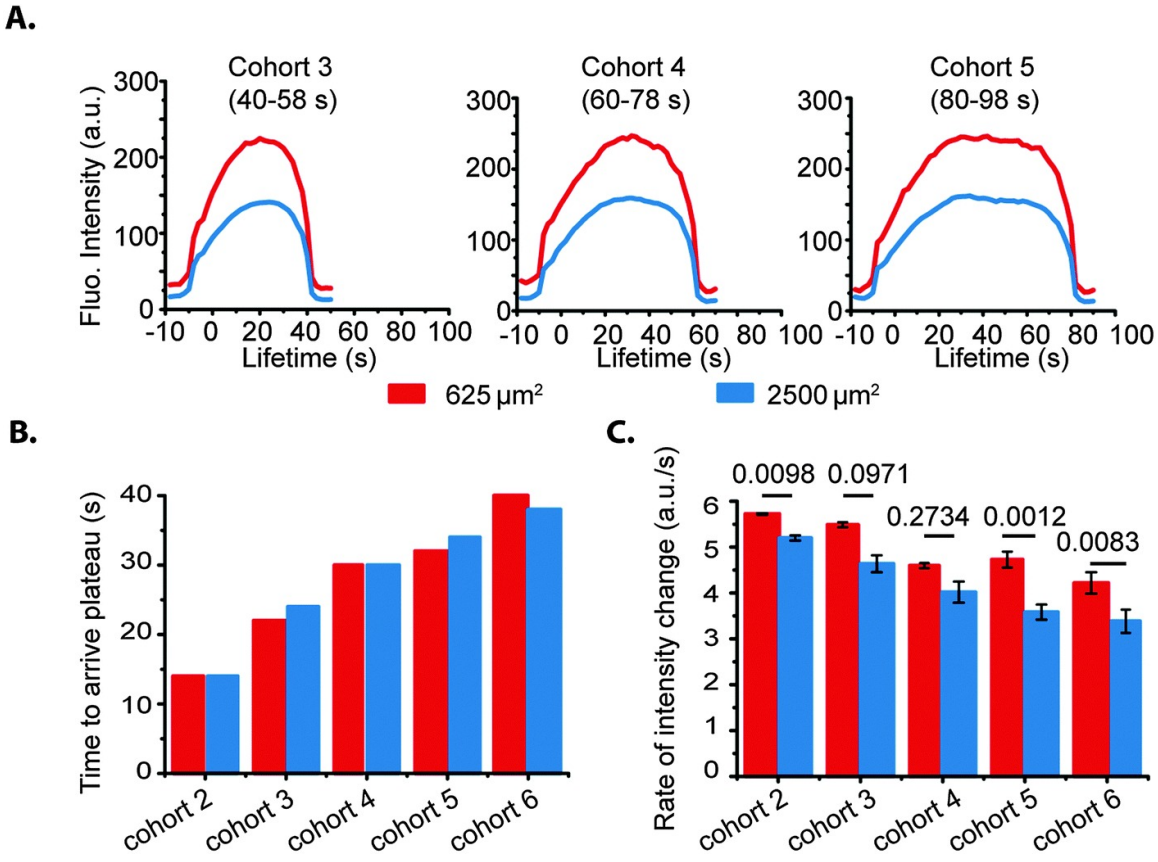

Figure 2.9: Decrease in plateau intensity is due to a decrease rate of intensity change. A. Comparison of average intensity traces between 625 µm^2 and 2500 µm^2 circular cells for cohort 3 (left), 4 (middle), and 5 (right). B. Comparison of time to arrive plateau intensity for cohort 2 to 6 between 625 µm^2 and 2500 µm^2 circular cells. The time point was determined by the first time point that fluorescence intensity reaches 95% of the maximum fluorescence intensity in a cohort from Figure 2.7 (A). C. Rate of intensity change of CLCa in CCPs for lifetime cohorts 26 for 625 µm^2 and 2500 µm^2 circular cells. Student's t test is performed between groups and p values are indicated in the figures.

2.3.3 Actin depolymerization and myosin contractility inhibition increase CCP fluorescence intensity

As the actin cytoskeleton and focal adhesions become more organized with increasing cell spreading areas on micropatterned substrates, we asked whether the whether the mechanical property of cells changes in cells plated on patterned surfaces. To establish that cell spreading on patterned substrates modified cell tension, we examined the subcellular localization of recently identified transcription factors YAP (Yes-associated protein) and TAZ (transcriptional co-activator with PDZ-binding motif) that exhibit nuclear localization when cell tension is increased (*Dupont et al.*, 2011). Consistent with previous findings, immunostaining of YAP showed nuclear localization in larger cells; whereas YAP in small cells was found diffused in the cytosol (Figure 2.10 (A)). Further quantification revealed that only 20% of 625 μm^2 square cells had nuclear localization of YAP compared to 90% for 2500 μm^2 cells (Figure 2.10 (B)). This indicated that larger cells developed more tension than smaller cells. As additional verification that cell tension increased with increasing cell spreading area, we employed micropipette aspiration to qualitatively measure the tension of the patterned cells as it reveals the force needed to deform the cell against a surface tension (*Hochmuth*, 2000). Applying a negative pressure of 1.2 kPa and measuring the projection length of the plasma membrane within the pipette (L_p) and pipette diameter (D_p), we calculated the normalized projection length (L_p/D_p) to qualitatively compare cortical tension (Figure 2.10 (C)). A longer normalized projection length indicated lower cortical tension. The normalized projection length for 625 μm^2 cells was more than three times longer than for 2500 μm^2 cells (13.8 compared to 3.3) (Figure 2.10 (D)). Altogether, our results indicated that resting cell tension increased with cell spreading.

Since larger cells also had a more developed actin cytoskeleton as evidenced by more stress fibers (Figure 2.3 and 2.6) and developed more tension (Figure 2.10 (A)),

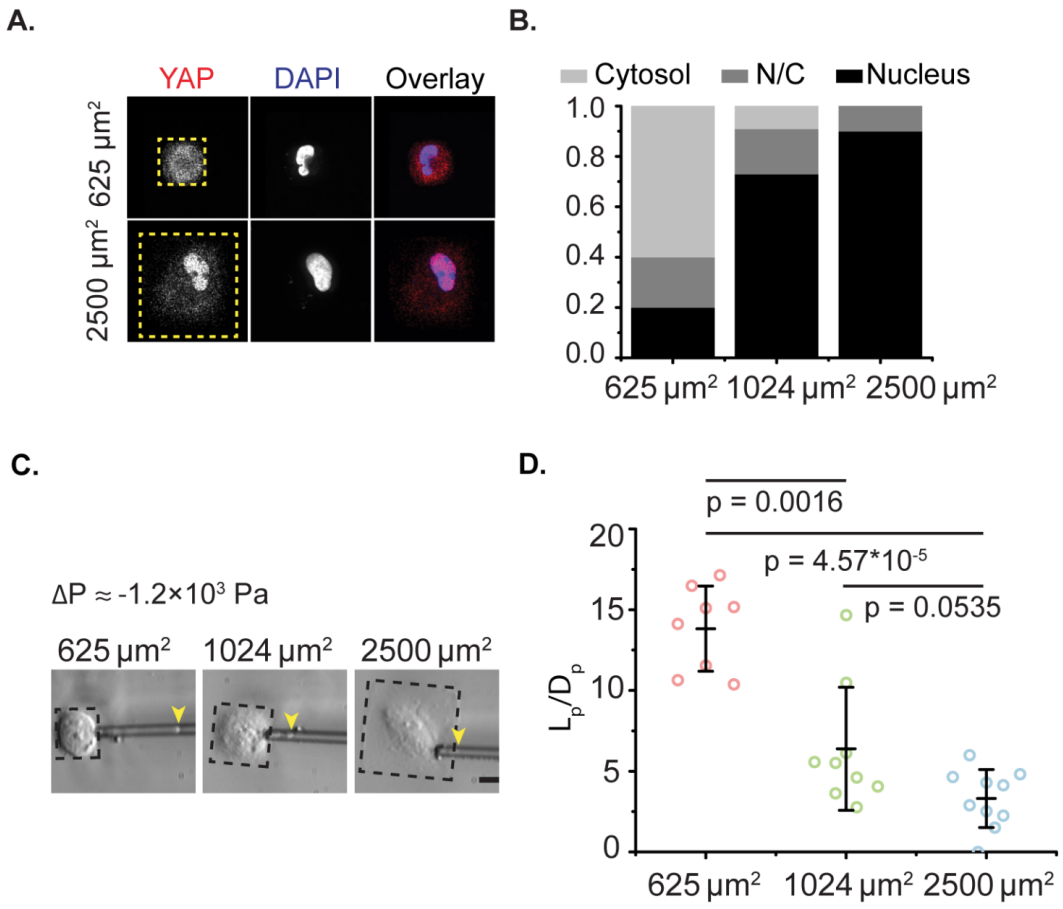

Figure 2.10: Tension increase with increasing cell spreading area. A. Fluorescent images of immunostained YAP, nucleus (DAPI) for 625 µm^2 and 2500 µm^2 square cells (top). Yellow dotted lines show the outline of the cell. B. Proportion of the cells displaying nuclear YAP localization (nucleus, black), even distribution of YAP/TAZ in nucleus and cytosol (N/C, dark grey), or cytoplasmic YAP (cytosol, light grey) for 625 µm^2 (left), 1024 µm^2 (middle), and 2500 µm^2 square cells. Number of cells for each pattern = 10 - 13. C. Brightfield images of micropipette aspirated cells on different cell spreading area with 1.2 kPa suction pressure (left). Yellow arrows point to plasma membrane projection in the micropipette. D. Graph of L_p/D_p for aspirated cells with an aspiration pressure of 1.2 kPa (right). Each data set was represented as average +/- S.D.. *p ¡ 0.05 by Wilcoxon rank sum test due to the non-normality of data of 1024 µm^2 cells.

we next sought to examine how the actin network was related to CCP dynamics on micropatterned substrates. Treatment with a low dose of latrunculin A (LatA), which sequesters actin monomers, caused some reduction in actin stress fiber evident by fluorescence staining of actin filaments (Figure 2.11 (A)). Under this condition, the proportion of short-lived CCPs increased significantly, especially for cells with the largest cell spreading area (Figure 2.11 (B)). Initiation density was similar before and after LatA treatment (Figure 2.11 (C)), suggesting that mild disruption of actin network does not affect CCP initiation and that factors other than only tension affect CCP lifetimes and initiation density. Interestingly, the plateau fluorescence intensity of CCPs significantly increased with LatA treatment though it was not immediately clear why this occurred.

Finally, since the cortical actin network that is juxtaposed to the plasma membrane exerts cortical tension on the membrane via activity of motor proteins such as myosin, we wanted to test the hypothesis that cortical tension regulates the fluorescence intensity of CLCa in CCPs. Using another pharmacological inhibitor, Y-27632, that blocks the Rho-associated kinase ROCK and reduces myosin contractility, we observed that CCP intensity substantially increased (Figure 2.11 (E)). These experiments show that disrupting the actin cytoskeleton in larger cells results in more abortive CCPs with more clarthrin fluorescence and that disrupting contractility also increased clathrin fluorescence in CCPs.

2.4 Discussion and Conclusion

The structural context of a cell is important for understanding how cells sense and respond to physical and mechanical cues (*Ingber*, 2006), and microcontact printing has been widely used to precisely control the degree of cell spreading (*Chen et al.*, 1997; *McBeath et al.*, 2004; *Kita et al.*, 2011; *Shao et al.*, 2014). Based on soft-lithography, the technique enables engineering of cellular microenvironment and can

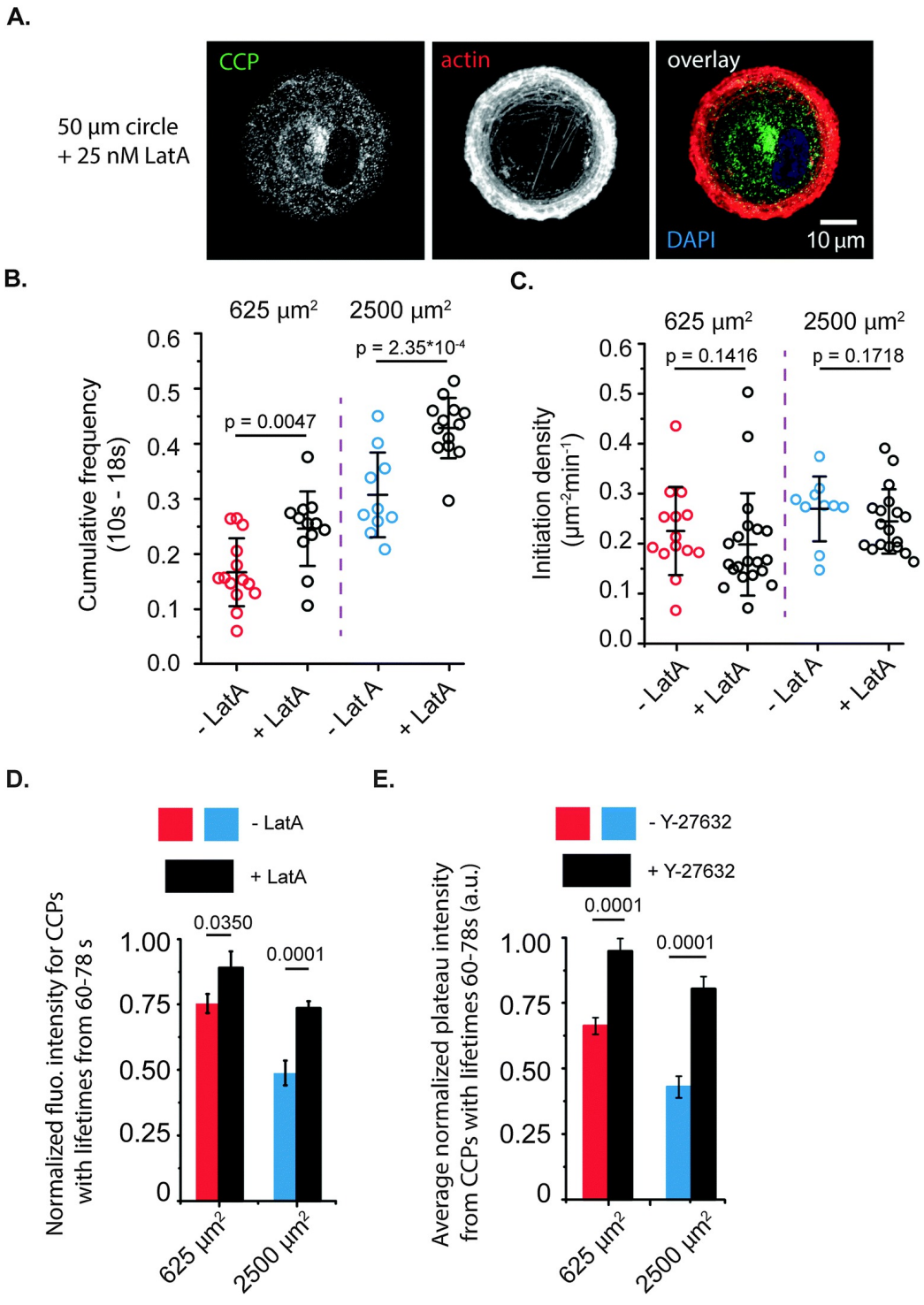

Figure 2.11: Caption on the next page

Figure 2.11: Latrunculin A and Y-27632 decrease CCP plateau intensity. (A). Fluorescence images of cells after 20 minutes of 25 nM LatA treatment show that cells maintained their shapes, but with some visible changes to the actin cytoskeleton. (B). Proportion of short-lived (10 s to 18 s) CCPs for 625 μm^2 and 2500 μm^2 circular cells without and with 25 nM latrunculin A. N = 14, 10 and N_{CCP} = 4372, 29351 for 625 μm^2 and 2500 μm^2 circular cells without treatment. N = 12, 13 and N_{CCP} = 4196, 48287 for 625 μm^2 and 2500 μm^2 circular cells with 25 nM latrunculin A. Student's t test is performed between groups with the same size. (C). Initiation density for the same groups of cells in the Figure 2.3. Wilcoxon rank sum test is performed between 625 μm^2 groups because of the non-normality of the data. Student's t test is performed between 2500 μm^2 groups. (D). Average plateau intensity of cohort 4 for 625 μm^2 and 2500 μm^2 circular cells with and without applying 25 nM latrunculin A. N = 14, 10 for 625 μm^2 and 2500 μm^2 circular cells without treatment. N = 12, 13 for 625 μm^2 and 2500 μm^2 circular cells with 25 nM latrunculin A. Student's t test is performed between groups and p values are indicated in the figures. (E) Average plateau intensity of cohort 4 for 625 μm^2 and 2500 μm^2 circular cells with and without applying 3 mM Y-27632. N = 14, 10, N_{CCP} = 4372, 29351 for 625 μm^2 and 2500 μm^2 circular cells without treatment. N = 10, 8 and N_{CCP} = 3240, 43600 for 625 μm^2 and 2500 μm^2 circular cells with 3 µM Y-27632. Other cohorts had similar results.

be used to generate carbohydrate, peptide and protein arrays (*Voskuhl et al.*, 2014). These microfabricated environments can be used to study structure and function of single cells, as in this study, or collective cell behaviors (*Vedula et al.*, 2014). Moreover, a variety of shapes can be made to control cell shape that guide distinct anisotropic internal cellular organization (*Théry et al.*, 2006). The ability to control cell size or subcellular adhesion using microcontact printing is broadly applicable to other areas of cell and developmental biology, including cell organization, cellcell interaction, cytoskeleton dynamics, cell adhesion, membrane trafficking, cellular differentiation and so on.

Here, we combined microcontact printing with quantitative live cell imaging of CCP dynamics and found that the proportion of short-lived CCPs and CCP intensity increased with large cell spreading area. CCP lifetimes range widely from under ten seconds to a couple of minutes (*Taylor et al.*, 2011; *Loerke et al.*, 2009). Recently, several groups have shown that short-lived events under 20 s may represent failed dynamin 2 recruitment to CCPs (*Aguet et al.*, 2013; *Taylor et al.*, 2012; *Grassart et al.*,

2014; *Cocucci et al.*, 2014), which is required for vesicle scission, further demonstrating the abortive nature of short-lived CCPs. One evidence from our data supporting this classification of abortive CCPs is that CCPs with lifetimes less than 20 s did not reach the maximum intensity attained by CCPs with 440 s lifetimes, suggesting incomplete assembly. Thus, one interpretation of our result is that increasing cell spreading area on micropatterned substrates increases the frequency of abortive CCPs as well as initiation density. These two opposing effects would seem counterintuitive, and we speculate that in this case, a higher frequency of initiation could be coupled to the increase in abortive CCPs due to the larger a cytosolic pool of endocytic proteins arising from more frequent CCP disassembly. This could be understood as a mechanism to compensate for the increase in abortive CCPs to ensure the robustness of CME.

From our intensity analysis of CCP trajectories, we quanti- fied maximum fluorescence intensity in cohorts of CCPs that had different lifetimes. Although CCPs are diffraction-limited, fluorescence intensity is proportional to the number of photons captured. In TIRF microscopy, the excitation intensity decays exponentially with the distance from the coverslip, so a dimmer signal could be due to the intrinsic property of TIRF imaging. However, our confocal imaging that had a 500 nm depth of focus verified a similar result that CCP intensity was lower in cells with large cell spreading areas. Furthermore, the higher cortical tension as well as stronger adhesion in large cells would reduce the spacing between the coverslip and the membrane, and thus increase the fluorescence intensity instead of the observed decrease in fluorescence intensity. Finally, our analysis that included thousands of CCPs per cohort group would average out a distribution of different CCP shapes (if they exist). The correlation between plateau intensity and CCP size has been shown previously and used as an indicator for CCP size *Ehrlich et al.* (2004); *Antonescu et al.* (2011); *Saffarian et al.* (2009). Thus, one interpretation of fluorescence intensity is CCP size. It is

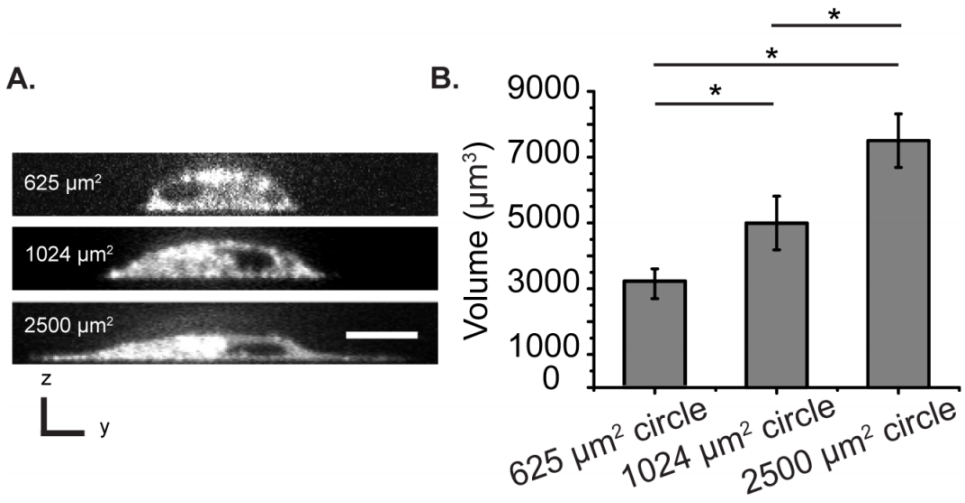

Figure 2.12: (A). Side view of representative micropatterned cells. Scale bar, 10 µm (B). Cell volume for 625 µm^2, 1024 µm^2, 2500 µm^2 circular cells. Error bars, standard deviation. N = 11, 8, 7 for 625 µm^2, 1024 µm^2, 2500 µm^2 circular cells respectively. *p ¡ 0.0002 by Student's t test.

possible that clathrin triskelia density in a CCP could change due to tension, though we think this possibility is low given the significant fluorescence intensity drop we observed. Although it remains a possibility that there could be very different CCP shapes that resulted in the changes in fluorescence intensity, we believe based on these considerations that a decrease in CCP intensity most likely results from a decrease in the number of clathrin triskelia, hence a decrease in CCP size. The slower clathrin accumulation rate could be due to the larger cell volume though cell heights also decreased with increasing cell area thereby increasing the effective concentrations that could not explain the slower polymerization rate (Figure 2.12).

Using a dynamic growth model similar to what has been used previously to study focal adhesion assembly (*Gov and Gopinathan*, 2006), we could gain additional insight on how clathrin polymerization rate changed with cell spreading area. Assuming the initial growth of a CCP is a flat domain where growth of the domain occurs only at the edge, but clathrin detachment can occur everywhere inside the domain with on- and off-rates as k_{on} and k_{off}, we have the dynamic equation for domain

area as $\frac{\mathrm{d}r^2}{\mathrm{d}t} = k_{on}r - k_{off}r^2$. The rate of growth during early lifetime (i.e. r is small) yields $\frac{\mathrm{d}r}{\mathrm{d}t} \approx k_{on}$, with a steady state size $r_{ss} \approx \frac{k_{on}}{koff}$. Since we found that increasing cell spreading area decreased the steady state sizes of CCPs by decreasing the rate of CCP growth, our dynamic growth model suggests a smaller k_{on} to satisfy these conditions. Although we have found that cell tension increases with increasing cell spreading on our micropatterned substrates, there are likely biochemical and other biophysical changes between small and large spreading cells. For instance, focal adhesion signaling, cytoskeleton organization, and differences in protein expression could affect CCP dynamics. In our study, we used acute drug perturbations by LatA or Y-27632 just prior to imaging CCP dynamics. During this time period, gene expression profiles would unlikely change significantly, sup- porting the idea that a physical effect could be relevant here. However, we cannot exclude the possibility that changes in signaling or other non-specific effects of LatA or Y-27632 have on membrane trafficking could account for our findings. Since actin polymerization is essential for CCP invagination under high tension conditions (*Boulant et al.*, 2011), our finding that the fraction of short-lived CCPs increased in cells treated with LatA on large patterns is consistent with the previous result.

Previous works have identified the importance of membrane tension in regulating certain aspects of CCP dynamics and the requirement of dynamic actin assembly in yeast and mammalian cells (*Aghamohammadazadeh and Ayscough*, 2009; *Boulant et al.*, 2011). The formation of coated vesicle is a balance of the energetic cost and energetic drivers, each of which are influenced by several parameters (*Stachowiak et al.*, 2013). In a theoretical study, the size of the vesicles can be influenced by tension through engaging actin polymerization and where the actin forces act would determine the size of the vesicles (*Walani et al.*, 2015). Using giant unilamellar vesicle as a model system and a theoretical framework to estimate polymer- ization energy from experimental data, it was found that there is a balance between mem-

brane tension and polymerization energy that sets the shape of clathrin coats (*Saleem et al.*). Our work is consistent with the findings of both of these works. In eukaryotic cells, CCPs invaginate in the presence of a cortical actin network. Thus, endocytosis of CCPs requires deformation of the membrane that couples tightly to the cortical actin network where membrane mechanics should be considered as a membranecortex composite (*Luo et al.*, 2013). In this context, it remains unclear what roles cortical actin network play in regulating distinct aspects of CCP dynamics since there is no clear relationship between cortical tension and membrane tension though It has been suggested that cortical tension has a huge influence on membrane tension (*Gauthier et al.*, 2012). In our study, reduction in cortical tension by inhibiting myosin contractility resulted in lower CCP intensity (i.e. smaller CCPs). One way to conceptualize this is that the tension from stress-stiffening of the cortical actin network provides physical constraints (*Stricker et al.*, 2010), or effectively compressive forces, that limit the assembly of CCPs.

Membrane and cortex mechanics change actively as cells change shape during different cellular activities (*Gauthier et al.*, 2012; *Salbreux et al.*, 2012). The shutdown of CME during early mitosis, presumably due to higher membrane tension, could be restarted by allowing actin to engage in endocytosis (*Kaur et al.*, 2014). Additionally, several recent studies have highlighted the role of tension in cell migration (*Houk et al.*, 2012; *Lieber et al.*, 2013, 2015) and how the tension gradient in motile cell could be coupled to polarized exo- and endocytosis (*Fogelson and Mogilner*, 2014). Although the functional sig- nificance of distinct CCP dynamics is not completely understood, it is becoming appreciated that endocytosis regulate signaling circuits by resolving signals in space and time (*Scita and Di Fiore*, 2010). The ability of clathrin-coated structures to respond to physical cues agrees with the view that CME is not only a process of eating and drinking, but a process that is modulated according to a cells physiological states. It requires further efforts to unravel the physiological meaning

behind these modulation and adaptations to ensure the robustness of CME.

CHAPTER III

Clathrin-coated Pits Dynamics on Polarized Patterns

3.1 Introduction

Cells' ability to establish polarization has fascinated many investigators. Seeding cells in a petri dish, we would observe that cells first spread homogeneously and adopt a circular morphology, but after several hours, they start to polarize, establishing polarized cellular structures. However, due to cell-cell heterogenity and complicated environments cells grow in, it is very hard to quantify the polarized cellular structures for many cells. The great randomness in cell shape and cellular structure has hindered us from understanding the spatial organization between cellular structures and their relationship with morphology. *Roybal et al.* (2016) took a computational approach, using approximated large deformation diffeomorphic metric mapping algorithm to standardize T-cells, and thereby found that actin nucleation Wiskott-Aldrich syndrome protein family verprolin-homologous protein 2 and actin-severing protein cofflin are the main regulator of actin dynamics upon co-stimulation by antigen. This method is convenient and does not require special engineering techniques, but using the algorithm to normalize every cell into the same shape might introduce artifacts. Another approach is to use micro-contact printing to pattern polarized patterns on

the substrate and thereby force a cell to conform to the same polarized morphology.

As we have discussed in Chapter II, micro-contact printing allows researchers to control and manipulate the micro-environment in cellular and subcellular level. Instead of using symmetrical patterns as in Chapter II, by using a polarized pattern or adding an extra structure in the symmetric pattern, investigators are able to induce polarity with both polarized and unpolarized morphology .

We have discussed in Chapter II that micro-contact printing was widely used to study the relationships between cell shape/morphology and physiological functions (*Chen et al.*, 1997; *McBeath et al.*, 2004), where cells on different sized patterns were able to initiate different signaling pathway to lead to different fate. By using different shaped micro-patterns, we are able to understand a different facet of cell biology - cellular structure spatial organization. This is important because we know that cell is far more than an ensemble of macro-molecules, but assembles different structure in a organized manner, which leads to function.

Using four different-shaped micro-patterns that have different adhesive areas but on which cells spread to the same shape, *Théry et al.* (2006) showed that it was cells' adhesive micro-environment that determines the polarity axis instead of anistropy of cell cortex. In the same study, the relative organization of nucleus-centrosome-Golgi axis in anistropic cells by averaging three structures from tens of the same shaped cells (*Théry et al.*, 2006).

micro-contact printing can not only control single cells' morphology but also create special micro-environment for subcellular structure. For highly polarized cells, such as neuronal cells, micro-contract printing provide tools to decouple factors to study axon growth. For example, neuron cells developed long axons on the micropatterned lines with polylysine-conjugated laminin or extracellular domain of the cell adhesion molecule, L1, but only dendrites on polylysine alone (*Kam et al.*, 2001; *Oliva et al.*, 2003).

Without any constraints, CCPs seem to distribute randomly on the membrane with different lifetimes. Does a cell regulate on how long and where CCP appear?

Using subcellular sized (5 µm circle arrays) pattern, *Liu et al.* (2009) observed that CCPs inside the fibronectin pattern have longer lifetime than ones outside and this elongation is due to the global cytoskeleton structure. However, there was not much difference regarding to CCP density within and outside the fibronectin pattern. Many studies have reported that there exists "hotspots" for CCP initiation where CCPs are more likely to appear, which depends on the integrity of cortial actin and other accessary proteins (*Gaidarov et al.*, 1999; *Nunez et al.*, 2011). However, it has not yet been explored where are these "hotspots". Without standardization, cells comes in all kinds of shapes and sizes, it would be hard to get any results with statistical significance. Here, we used micro-contact printing technique to printed anisotropic shapes and then measured CCP dynamics. With image registration, we were able to align tens of cells with the same orientation and thereby calculate the average CCP initiation density, lifetime, and motility at the "same" location across many cells.

3.2 Method and Material

3.2.1 micro-contact printing

The procedure was the same as in Chapter II section 2.2.2. To study the spatial organization of CCPs, we designed anisotropic pattern shown in Figure 3.1.

3.2.2 Cell lines and antibodies

For this study, the cell line and antibodies were the same as in Chapter II section 2.2.1 and 2.2.3.

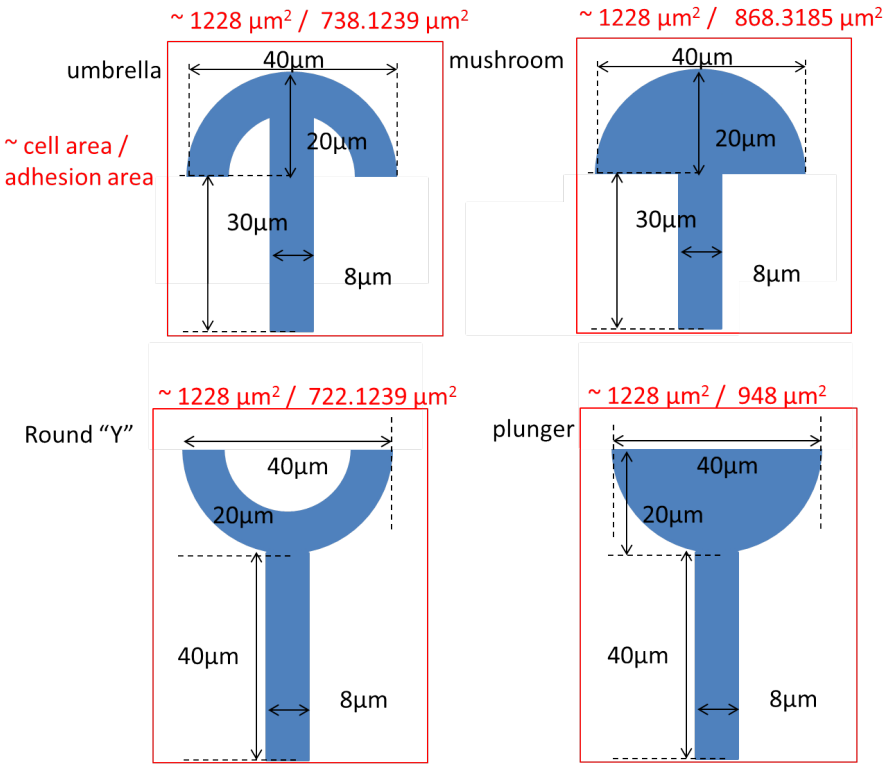

Figure 3.1: Designed shape for micropatterns.

3.2.3 Image registration

Due to the random orientation of patterns, it is essential to align all the same patterns and thus the cells. Once we have all the cells aligned, we can overlap them and calculate the averaged spatial features. The image registration involved in three steps:

1. Create a mask (M_{im}) from the micro-contact printed protein image (I).
2. Create a mask (M_{s}) based on the designed shape.
3. Align M_{s} and M_{im}.

To visulize micro-contact printed patterns, we added 20 µg/mL of Alexa fluor 568 fibrinogen to 40 µg/mL fibronectin. We used k-means algorithm (more details in Appendix A) to group the image into two categories: micro-contact printed pattern and background, and obtained a mask M_{im}.

Since the designed shapes only consist half-circle arcs and straight stems, it can be characterize presicsely using Matlab command given the shape and position parameters. Therefore, we programmed in Matlab to create a black-white image for the shape and used it as the mask $M_{\mathrm{s}}(\mathrm{shape}, \mathrm{position})$, where shape parameter includes radius of circle (in nm), stem length, line width, and pixel size, and position parameter: x-coordinate of vertex position, y-coordinate of vertex position, and rotation angle in radius. Notice that these paramters are enough to define the mask of the shapes we designed.

Our goal is to find the shape and position parameters that define M_{s} to match the M_{im}. The goodness of fit or objective function is defined as

$$\min \sum \left(M_{\mathrm{s}}(\mathrm{shape}, \mathrm{position}) - M_{\mathrm{im}}\right)^2$$

Our goal is find

$$\mathrm{shape}^*, \mathrm{position}^* = \underset{\mathrm{shape,position}}{\arg\min} \sum \left(M_{\mathrm{s}}(\mathrm{shape}, \mathrm{position}) - M_{\mathrm{im}}\right)^2$$

The minimization problem was solved using Matlab built-in nonlinear programming solver *fminsearch*. To efficiently solve this problem, we first kept the shape parameters fixed and only fitted the position parameters, and in the second round, we allowed all the parameters to converge.

3.2.4 Density calculation

Image registration allowed us to overlap different cells with the same shape and thereby calculate the phenotype distribution across many cells. Using CMEanalysis software package (*Aguet et al.*, 2013), we obtained the lifetime, position and intensity profile for every CCP. Then for a target feature, for example, lifetime t, we were able to calculate the density as the following:

$$d(x_S, y_S) = \frac{1}{N} \sum_{i=1}^{N} \frac{\sum_{(x_j,y_j)\in S_i} t_j}{|S_i|}$$

where (x_S, y_S) indicates the position on the pattern, S_i all the valid CCPs of cell$_i$ that lie in $\{(x, y) : (x - x_S)^2 + (y - y_S)^2 \leq r^2\}$, $|S_i|$ the number of CCPs in S_i.

3.3 Result and Discussion

3.3.1 Actin and CCP on polarized patterns

As we see from Figure 3.1, we designed four different patterns to study how CCPs and their phenotypes distribute in anisotropic cells. Specifically, we expected cells on "umbrella" and "mushroom" shapes spread to the same shape, as well as ones on "Round 'Y'" and "plunger" shapes to be similar. More over, we designed that "umbrella" and "round 'Y'" or "mushroom" and "plunger" have the same adhesive area. In this way, we are able to decouple cell shape and adhesive area from other factors.

The first column in Figure 3.2 shows the micro-printed pattern. Despite the cell shape similarity between "umbrella" and "mushroom" or "round 'Y'" and "plunger", we observed a visible difference in actin cytoskeleton. For "umbrella" pattern, there was a thick actin band at the arc, but it was barely visible for the "mushroom" shape. However, for the "mushroom" shape, strong actin showed up at the sides which connected the half-circle to the bottom vertex. Notably, there was not so much difference between "round 'Y'" and "plunger" shaped cells. For CCPs, there was no obvious patterns.

3.3.2 Focal adhesion and CCP on polarized patterns

Focal adhesion is a macromolecule complex that connects extracellular matrix to actin cytoskeleton. Because of this special structure, it plays a crucial role in

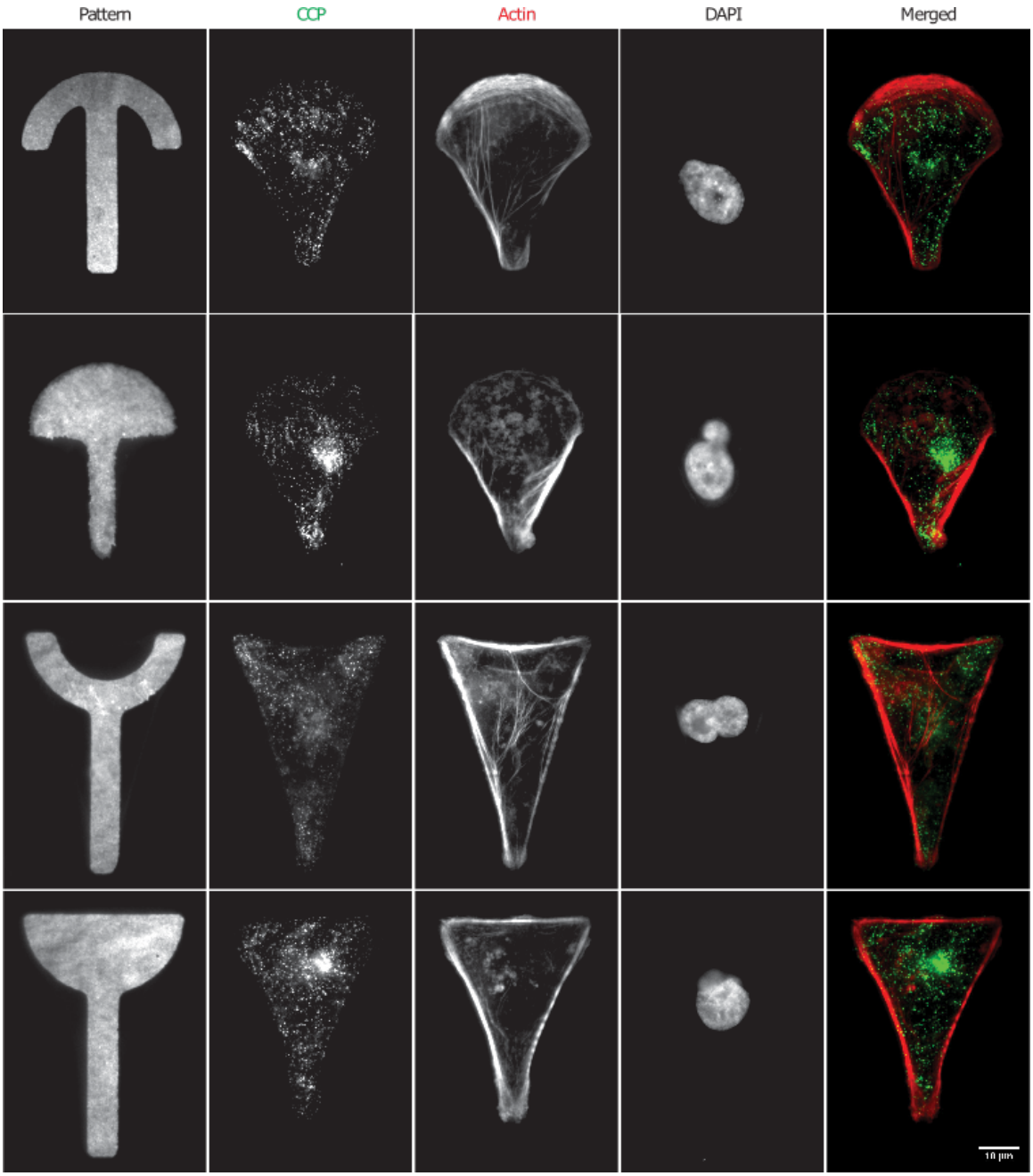

Figure 3.2: Immunofluoresecne of actin and CCPs on the patterned cells.

mechanotransduction. By placing cells on different sized but same shaped patterns, *Chen et al.* (2003) argued that cell shape exerts global control on focal adhesion assembly.

We also stained paxillin, a marker for focal adhesion, to see whether focal adhesion reflected the difference in actin cytoskeleton. Indeed, between "umbrella" and "mushroom" shapes or "mushroom" and "plunger" shape, the difference in focal adhesion is less visible (Figure 3.3). However, we still observed more distinct focal adhesions on the arc of the "umbrella" shape than the "mushroom" one, which might explain the more pronounced actin cytoskeleton observed in the former one. One might argue that it was biased to just look at one cell. Aligning the cells using image registration framework, we calculated the average "clathrin", "paxillin", and "actin" image for four different shaped cells (Figure 3.4). The paxillin intensity seemed to correlate with fibronectin area, and in all four shapes the focal adhesions were distinct at the vertices of shapes. Similar to the example in Figure 3.2, there was a thicker actin band for "umbrella" and "Round 'Y'" shaped cells.

Actin and focal adhesions are skeleton of the cells, reflecting how cells achieve balance on the extracellular matrix with specific morphology. Even though it seems like a purely mechanical problem, the balance process involves sophisticated biochemical regulation. It has been recognized that cells sense mechanical environment via generating the force from pulling the extracellular matrix. The coordination between cytoskeleton and focal adhesion is regulated via Rho GTPases (*Ridley and Hall*, 1992). Focal adhesion kinase, the master regulator of focal adhesion, connects to Ras pathway by creating a high affinity site at tyrosin 925 to Src homology 2 domain (*Provenzano and Keely*, 2011). Also, in an early study, it was found that phosphorylations at tyrosine 397 and 925 of focal adhesion kinase led to mitogen-activated protein kinase activation during cyclic stretch of fibroblast (*Wang et al.*, 2001). Because of the central roles of these pathways in cell biology (*Etienne-Manneville and*

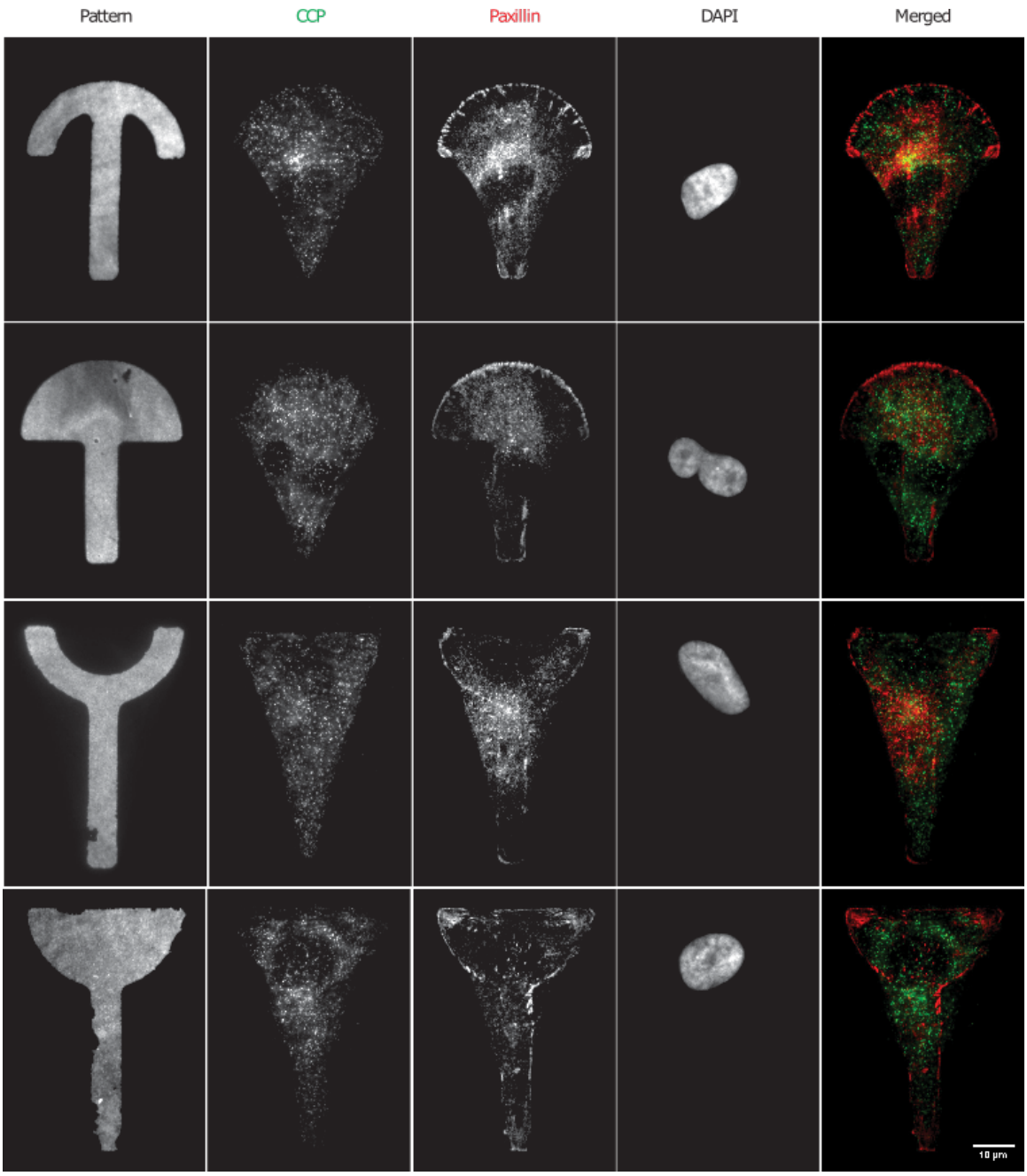

Figure 3.3: Immunofluoresecne of paxillin and CCPs on the patterned cells.

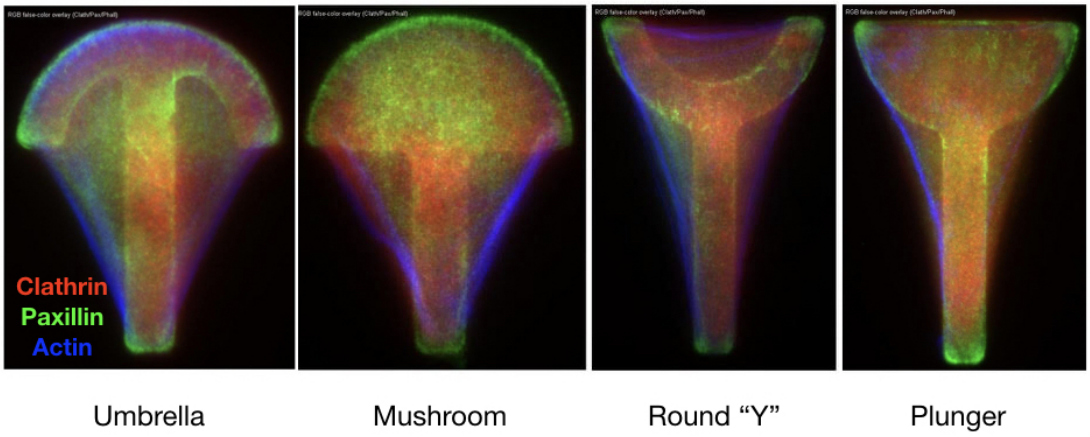

Figure 3.4: Average "clathrin", "paxillin", "actin" for four different shaped cells. Number of cells: $N_{umbrella}$=12, $N_{mushroom}$=12, $N_{round\ "Y"}$=16, $N_{plunger}$=10

Hall, 2002; *Martin*, 2001; *Johnson and Lapadat*, 2002), the seemingly pure mechanical properties have thus far-reaching effects on cell physiology.

3.3.3 CCP initiation density, lifetime and motility on polarized patterns

We would therefore like to ask, how do CCPs respond to anisotropic micro-contact printed patterned cells? To answer this question, we look at the following aspects of CCPs: where do they initiate? How long do they last on the membrane? How much do they move on the membrane?

In Chapter II, we have observed that larger cells had a slightly higher initiation density. We can see that when we mapped out the initiation density on the anisotropic cells there were indeed "hot" areas where CCPs tended to initiate more (Figure 3.5). At the area where there was no adhesion, we observed an increase in initiation density. However, when we looked at the overall trajectory density, there was a rather negative correlation between initiation density and trajectory density (Figure 3.6). This could only make sense that there were more CCPs to start in those areas with dense trajectory and they stayed longer on the membrane. Indeed, when we compared Figure 3.5, 3.6, and 3.7, lifetime positively correlated with trajectory density where

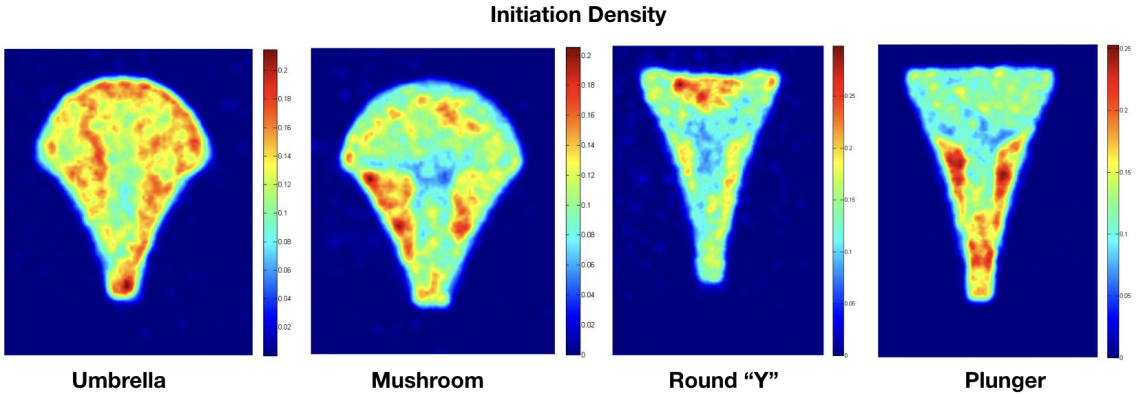

Figure 3.5: Initiation density of CCPs on the patterned cells.

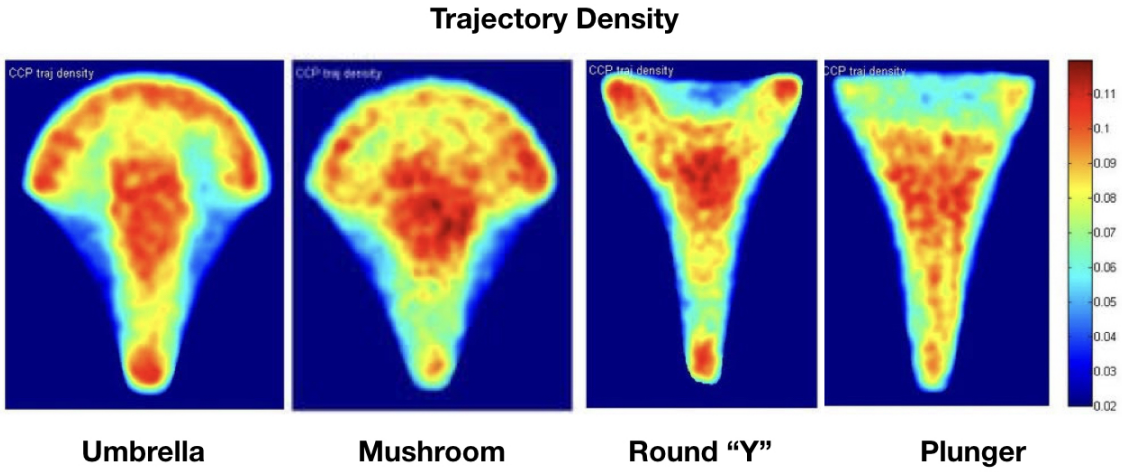

Figure 3.6: Trajectory density of CCPs on the patterned cells.

the initiation density was lower. Specially, we can give an inverse example that in the shape "Plunger", at the wing sides, we saw a very high initiation density and also a high trajectory density, but then the lifetime was very low. Notably, the motility of CCPs was negatively correlated with lifetime (Figure 3.8).

From Figure 3.2 and 3.3, "umbrella" and "mushroom" shaped or "round 'Y'" and "plunger" shaped cells had roughly the same morphology, and yet their CCP phenotypes were largely different. This further supports *Liu et al.* (2009) that CCP dynamics is controlled locally by perhaps underlying cytoskeleton structure or other cellular structures. In cell biology, it is well believed that "structure determines the

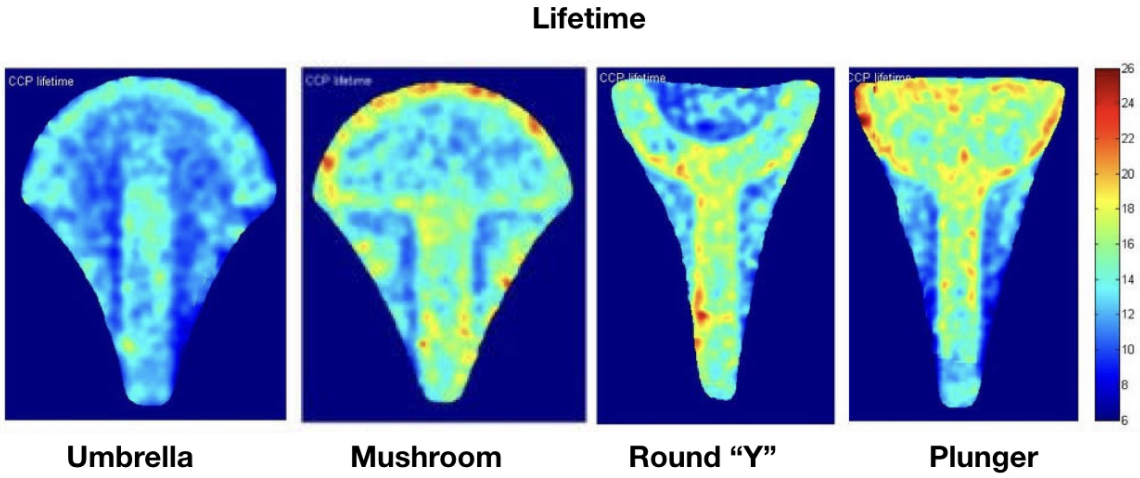

Figure 3.7: Lifetime of CCPs on the patterned cells.

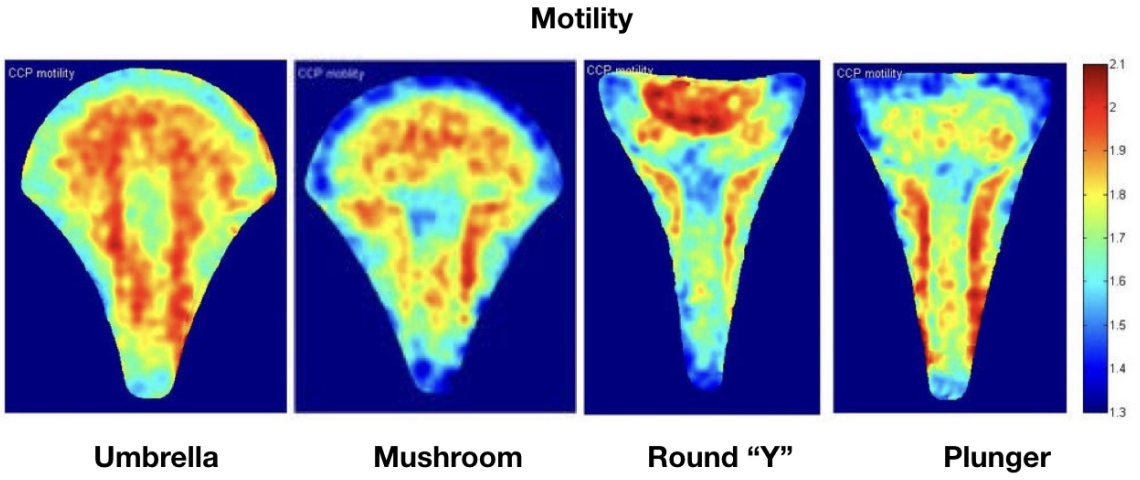

Figure 3.8: Motility of CCPs on the patterned cells.

function". However, as much as we have tried to measure and observe CCP to a great detail, we do not fully understand why they distribute on the membrane in the way they do, and definitely fail to predict where and when they will appear. Even with micro-contact printing, we seem to be able to control the lifetime and initiation spot, we do not know the significance of such pattern.

To this end, it brings us a major drawback of micro-contact printing system: we can only study the structural aspect of cellular processes but cannot glean much insights into the function of spatial organization. As we discuss in Chapter I, early on studies on CME and CCPs were sepearated in their phenotype and function. The functional studies were often isolated from other cellular processes. However, sometimes, ligand stimulation not only induces receptor-mediated endocytosis, but also ignites a series cellular processes that change cell behavior. One such example is chemotaxis. Chemotaxis is a process where cells migrate towards the chemoattractant (ligand), during which cells rapidly establish polarity. On the countary, most studies in this area focus on the downstream signaling pathway and cell behavior, but few on CME's role in the process. We think it is a great niche for us to further understand CME and CCPs. Therefore, we devote our last project to study CME during neutrophil polarization, one of the events upon chemoattractant stimulation.

CHAPTER IV

Clathrin-mediated Endocytosis during Neutrophil Polarization

4.1 Introduction

Chemotaxis describes the amazing ability for a cell to sense and move toward or away from a higher concentration of chemicals in the environment. It is a crucial process in normal physiology, and is involved in embryonic development, immune cell trafficking, and wound healing. Moreover, in pathogenesis of many diseases such as cancer, chemotaxis is essential in the disease progression and metastasis. Conceptually, chemotaxis can be divided into three processes: motility, gradient sensing, and polarity (*Swaney et al.*, 2010). In the abscence of stimulus, actin-binding proteins are recruited to the basal surface, forming a wave-like structure, which facilitates the generation of pseudopodia. Given an environmental cue, neutrophils then would develop a significant front - lamellipodia (*Yang et al.*, 2016) and uropod at the back which together drive the cell to move forward (*Hind et al.*, 2016).

Gradient sensing also plays a key role in chemotaxis, conferring directional migration for the cell with great sensitivity (*Iijima et al.*, 2002).For example, Dictyostelium discoideum cells are able to sense a concentration gradient of only 1-5% across the cell (*Mato et al.*, 1975). Despite many years of research, the detailed mechanism of

this process is not completely known. Receptors that directly sense the chemicals are found to distribute evenly over the cell. It is believed that slight differences in receptor occupancy leads to the polarized distribution of intracellular proteins and lipids, which then reorganize actin and drive directionaly cell motility. Currently, several models based on local excitation and global inhibition (LEGI) are widely used to explain the ability for cell, whether polarized or not, to sense the chemical gradient (*Swaney et al.*, 2010). In brief, upon stimulation, a fast excitation followed by a delayed inhibition accounts for the temporal and spatial responses of a cell to chemoattractant stimulation. However, a detailed molecular mechanism is still needed. Experimentally, many studies have focused on the possible role of signaling molecules in gradient sensing. For example, disruption of PI 3-phosphotase, PTEN, in Dictyostelium discoideum cells perturbed chemotaxis, which caused cells without PTEN to follow a circuitous route toward the chemoattractant (*Iijima and Devreotes*, 2002). Since cells lacking PTEN can still undergo chemotaxis, this suggests that other molecules or processes may also be involved in chemotaxis and that we may not be able to attribute a single protein to gradient sensing. Rather, from a systems biology perspective, it is important to consider how other cellular processes might interface with gradient sensing.

The ability to establish polarity is essential for effective chemotaxis, revealing the amazing temporal and spatial control over macro-molecules and their interactions in a cell. Within tens of seconds to several minutes upon stimulation by fMLP, neutrophils rapidly establish polarity, with lamellipodia protruding in the front and a long tail at the back. Many molecular effectors activated by fMLP upon FPR binding are known, including the ones that mediate G protein and arrestin signaling (*Wagener et al.*, 2016). Like most GPCRs, agonist binding to FPR triggers internalization from the plasma membrane to intracellular compartments (*Ernst et al.*, 2004). Although bidirectional interplay between signal transduction and endocytosis of cell surface

receptor is an emerging theme (*Jean-Alphonse and Hanyaloglu*, 2011; *Sorkin and von Zastrow*, 2002), the interplay between endocytosis and fMLP-FPR signaling in the context of neutrophil polarization has not been investigated in detail.

CME is one of the major endocytic pathways that GPCRs are internalized following ligand binding (*Wolfe and Trejo*, 2007). CME has been shown to play an important role in signal transduction. It actively regulates the turnover of the receptors on the membrane, thereby governs the amount of signal a cell can receive. CME occurs through the assembly of discrete CCPs, each is a macromolecular assembly that consists of major scaffold/signaling molecules such as β-arrestin 2 and assembles and dissembles in a timely manner. Many studies have shown the importance of CME in polarized cell function and physiology. In polarized budding yeast, endocytoticvesicles corral central exocytic zone to establish robust polarity (*Jose et al.*, 2013). In migrating cells, the spatial distribution of CCPs has been a subject of debate. Early electron microscopy studies showed that CCPs appeared to be at the back and almost none at the front lamilipodia (*Davis et al.*, 1982). However, another study observed that CCPs were polarized at the leading edge in migrating Madine Darby canine kidney (MDCK) cells (*Rappoport and Simon*, 2003). Combining spinning disk confocal light sheet microscopy, *Kural et al.* (2015) characterized CCP distribution in migrating glioblastoma cells and found spatial differences in CCP dynamics between dorsal and ventral membrane.

In this project, we aim to investigate the role of CME during HL60-derived neutrophil polarization. We first quantify the spatial co-distribution of FPR and CCP in fMLP-stimulated and non-stimulated cells. The phenotype differences for fMLP-stimulated and non-stimulated cells suggested that CME might be important in neutrophil polarization, and we demonstrate the importance of CME for effective polarization using high content imaging and pharmacological perturbation of clathrin and dynamin. Both treatments potently blocked neutrophil polarization and fMLP-

induced ERK and Akt signaling. Analysis of actin-clathrin and actin-β-arrestin spatial correlation revealed differential interaction between actin cytoskeleton and endocytic proteins with and without fMLP, suggesting a close-knit relationship between CME of FPR and FPR signaling during neutrophil polarization.

4.2 Material and Methods

4.2.1 Cell culture and differentiation

We received HL-60 cell as a gift from Dr. Orion Weiner (UCSF). HL-60 cells were maintained in RPMI medium supplemented with 10% heat-inactivated FBS and 1% penicillin streptomycin at 37 °C/5% CO2. Neutrophil-like cells used in experiments were differentiated from HL-60 by introducing 1.5% DMSO into growth medium for 3-6 days.

4.2.2 Flow cytometric analysis of fMLP internalization

The flow cytometry assay was performed to measure the internalization of fMLP. Differentiated cells were first serum-starved for 30 min at 37C and then incubated with 100 nM fluorescein conjugate of formyl-Nle-Leu-Phe-Nle-Tyr-Lys (F1314, Thermo Fisher Scientific, MA) on ice for 30 min to equilibrate the binding between ligands and receptors. The cells were transferred to 37 celsius water bath and incubated for the indicated amount of time, while keeping one sample on ice as a control. The endocytosis was halted by adding a volume of ice-cold mHBSS and returning the sample to ice. Samples were then spun at 400 g to pellet and washed with acid buffer (500 mM Glycine in mHBSS, pH =2.7) to remove the surface binding, followed by two more ice-cold mHBSS wash. The samples were measured within an hour using Guava easyCyte flow cytometer (Millipore, MA).

4.2.3 Fibronectin coverslip coating

In order for cells to adhere to the surface, all coverslips were coated with 100 g/mL fibronectin (F4759, Sigma, MO) in Ca^{2+}/Mg^{2+}-free PBS for 1 hr. The coated coverslips were then washed twice with Ca^{2+}/Mg^{2+}-free PBS and incubated in mHBSS with 1% endotoxin-free human serum albumin (Gemini Bio-Products, CA) for more than 15 min. They were used within the day of preparation.

4.2.4 Immunostaining

For immunostaining, cells were fixed in ice-cold 3.7% paraformaldehyde in intracellular buffer (140 mM KCl, 1 mM $MgCl_2$, 2 mM EGTA, 320 mM sucrose, and 20 mM HEPES with pH=7.5) for 45 min on ice. Washed and permeabilized with 1% Triton X-100, cells were then blocked in intracellular buffer containing 1% bovine serum albumin for 1 hr, before incubating with primary antibody overnight at 4 °C. On the second day, after washed six times with PBS, samples were incubated with secondary antibody along with rhodamine-phalloidin (PHDR1, Cytoskeleton, CO) and DAPI (D9542, Sigma-Aldrich, MO) for 3 hours at room temperature at manufacturers recommended concentrations. Cells were imaged after washing with PBS.

In immunostaining experiments, we have used the following antibodies: phosphomyosin light chain2 (Ser19) antibody (#3675, Cell Signaling Technology, MA), α-tubulin antibody (#2144, Cell Signaling Technology, MA), clathrin antibody [X22] (ab2731, Abcam, MA), β-arrestin-1/2 antibody (sc-74591, Santa Cruz Biotechnology, TX).

4.2.5 Microscopy for fixed samples

We employed different imaging systems for different experiments. To observe clathrin and β-arrestin, we used TIR-FM; for each cell, we also recorded the actin and nucleus using epi-fluorescence microscopy which is available on the same microscope.

TIR-FM was performed on a Nikon TiE-Perfect Focus System (PFS) microscope equipped with an apochromat 100X objective (NA 1.49), a sCMOS camera (Flash 4.0, Hamamatsu Photonics, Japan), and a laser launch controlled by an acoustooptic tunable filter (AOTF).

To measure the effect of drug treatments on neutrophil polarization, cells were stained with α-tubulin, phospho-myosin light chain 2, actin and nucleus and imaged using Cytation 5 Cell Imaging Multi-Mode Reader (BioTek, VT) equipped with 20X objective and DAPI, GFP, RFP, and Cy7 imaging filter cubes. For each condition (specified in Figure 3), we took around 400 images from 2 different coverslips.

4.2.6 Spatial correlation between clathrin-coated pit/β-arrestin and actin

Clathrin-coated pit and β-arrestin structures were imaged using TIR-FM to get high-resolution and low noise-signal ratio pictures. CMEanalysis package were used to faithfully detect the dot-like structure, as clathrin-coated pits and β-arrestin are. For each dot-like structure, its location (x_i, y_i) and intensity A_i in the cell was determined. To obtain the correlation between CCP/β-arrestin and actin intensity, we calculated the local density for each detected CCP/β-arrestin as well as the corresponding intensity at the same location for actin. The density can be formulated mathematically:

$$\text{local density}|_{(x_i,y_i)} = \frac{\sum_{(x_i,y_i)\in\text{detected puncta}} \mathbb{I}\left(R_d^2 - (|x_i - x_j|^2 + |y_i - y_j|^2)\right)}{\pi R_d^2}$$

where $\mathbb{I}(x) = \begin{cases} 1 & x \geq 0 \\ 0 & x < 0 \end{cases}$, R_d is the radius we used to calculated the local density for dot-like structures, and (x_i, y_i) is the coordinates we obtained from the detection

results. Similarly, local actin intensity can be formulated:

$$\text{local actin intensity}|_{(x_i,y_i)} = \frac{\sum_{(a-x_i)^2+(b-y_i)^2 \leq r^2} \text{ActinImage}(a,b)}{\pi r^2}$$

where ActinImage(a, b) is the intensity at (a, b) for actin image, r is the radius within which we counted the pixel as local.

4.2.7 Polarization quantification

In order to unbiasedly quantify drug effect on neutrophil polarization, we used Cytation 5 imager to take around 1000 cells per condition. A customized CellProfiler pipeline, which implemented watershed algorithm, was applied to the images to effectively generate the masks for individual cells. To overcome over-segmentation of the watershed algorithm, we used DAPI as the marker image, added up three other channel images (MT, actin and pMyosinII) as the secondary image, and then applied the watershed algorithm. We then manually inspected every cell/mask pair and discarded the cells which were mistakenly segmented. Using the generated masks, we calculated the following morphological features: area, circularity. Employing both the staining image and mask, we quantified the intensity features and center features, which are listed in Table 4.1. The feature extraction was implemented in MatLab.

4.2.8 Western blot analysis

For Western blots, an equal volume of ice-cold 20% trichloroacetic acid (TCA) was added to the sample to lyse the cells. 40 mM NaF and 20 mM β-glycerophosphate were included if blotting against the phospho-proteins. The mixtures were then kept at 4 °C overnight for maximum yield of proteins. Lysates were then centrifuged at 13,000×g at 4 °C for 5 min to pellet. The pellets were then washed in 0.5% TCA once and then resuspended in 50 µL 2× Laemmli sample buffer (1610737, Bio-Rad, CA)

Category	Feature name	Notes
Morphology feauture	area	
	circularity	$4\pi \cdot \text{area}/\text{perimeter}^2$
Center feature	MT bright spot to center	Bright spot is defined as the pixels within cell segment with intensity more than 90% percentile intensity.
	Actin bright spot to center	Center for a specific fluorescent channel is given by mean x and y coordinates of pixels weighted by their intensity in the segment mass.
	pMyosinII bright spot to center	
Intensity feature	MT intensity standard deviation	Intensity standard deviation was calculated as the standard deviation of the intensity in the segmented mass.
	Actin intensity standard deviation	
	pMyosinII intensity standard deviation	

Table 4.1: Description of the calculated features.

containing 30 mM NaOH and 5% β-mercaptoethanol. Protein bands were separated by SDS-PAGE gel electrophoresis and transferred to nitrocellulose membrane. The membrane was blocked with 5% milk and incubated overnight with following antibodies: CHC [TD.1] (24578, Abcam, MA); $pAkt_{308}$ (2965 or 4056, Cell Signaling Technology, MA); $pAkt_{473}$ (4060, Cell Signaling Technology, MA); total Akt (4691, Cell Signaling Technology, MA); pERK (9106 or 4376, Cell Signaling Technology, MA); GAPDH (24778, Santa Cruz Biotechnology, TX); actin (8432, Santa Cruz Biotechnology, TX). The blots were developed with fluorescent secondary antibodies: goat anti-mouse DyLight 680 (35518, Thermo Fisher Scientific, MA) and goat anti-rabbit DyLight 800 (SA5-10036, Thermo Fisher Scientific, MA), and the blots were imaged using Odyssey Infrared Imaging System (Li-COR, Biosciences, NE). The Western

blot results were quantified using ImageJ. At least three independent experiments were conducted for each condition.

4.3 Results and Discussion

4.3.1 CCPs and FPR spots organize differently in the presence of fMLP

In the presence of fMLP, even with uniform concentration, neutrophils start to polarize with distinctive phenotypes, such as a dramatic increase in cell area, adopting an elongated shape, and formation of polarized signaling molecules and sub-cellular structures within the cell. To investigate the spatial organization between FPRs and CCPs, we imaged FPRs and CCPs in fixed HL-60 derived neutrophils (hereafter referred to as neutrophil) using TIR-FM without and with uniform 100 nM fMLP after 5 minutes. TIR-FM microscopy uses a thin evanescent excitation field to observe the ventral cell surface, and largely avoids fluorescence signals from intracellular structures. Besides a significant increase in cell size, we observed more FPR puncta and CCPs and a noticeable greater degree of colocalization in fMLP-treated cells (Figure 4.1A). Using Pearson coefficient, a standard colocalization analysis, between the two fluorescence channels, there was a large variation and an overall smaller mean coefficient for fMLP-treated cells (Figure 4.1B). However, this metric only measures the linear relationship between two variables and ignores local structures of the data; therefore, a more detailed analysis is needed.

CCPs and FPRs were detected using point-source detection software package based on an improved Gaussian mixture model(*Aguet et al.*, 2013). We noticed that there was a dramatic increase in the number of CCPs and FPR puncta upon fMLP stimulation and there were more FPR puncta than CCPs under both stimulating and non-stimulating conditions. However, not all of the CCPs were associated with FPRs, where we define the association by the number of FPRs within a 5-pixel (290

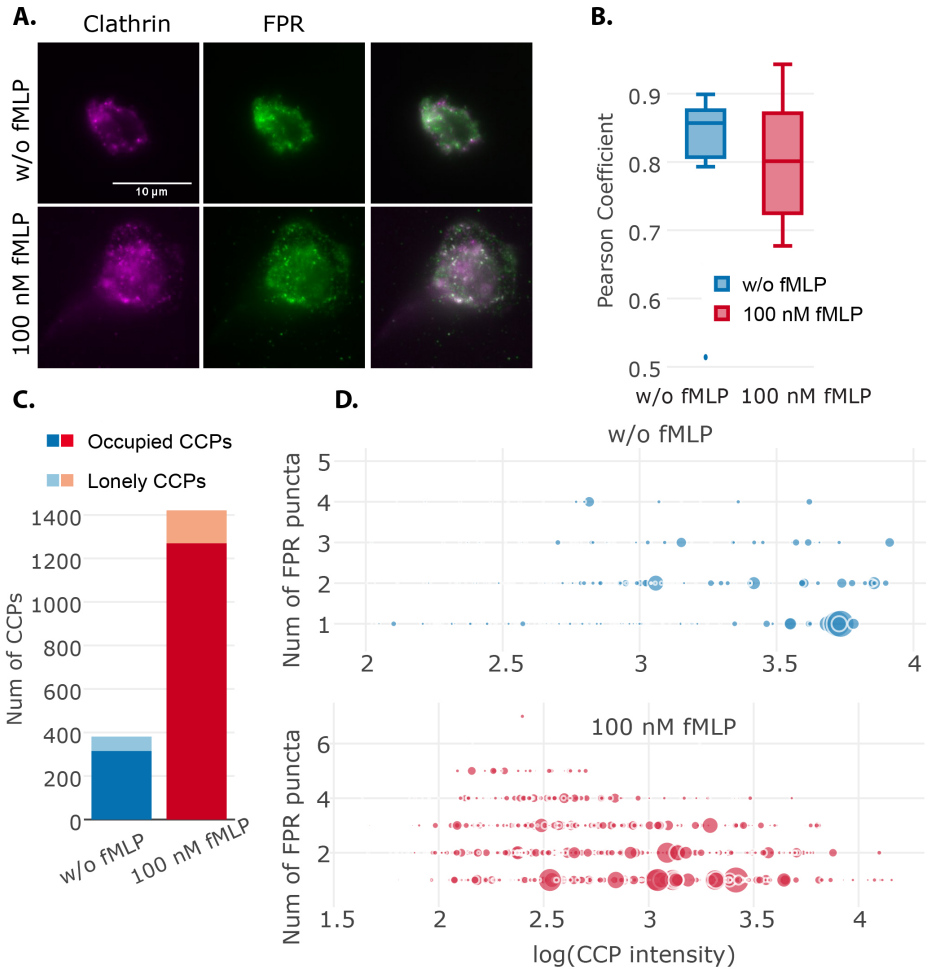

Figure 4.1: Spatial organizations between CCPs and FPRs are different with and without fMLP. (A) Example TIRF images of FPR (green) and CCP (magenta) without (upper) and with (bottom) 100 nM fMLP. Arrowheads point to colocalized spots. (B) Pixel-wise Pearson coefficient was quantified. Wilcoxon rank-sum test $p = 0.46$ does not reject the null hypothesis. ($n_{w/o\ fMLP} = 8$, $n_{fMLP} = 8$) (C) The bar graph of the number of occupied CCPs and vacant CCPs, where we define "vacant CCPs" as CCPs without FPR spots within its 10-pixel radius. (Occupied CCP number: $n_{w/o\ fMLP} = 315$, $n_{fMLP} = 1270$; vacant CCP number: $n_{w/o\ fMLP} = 66$, $n_{fMLP} = 151$; a total of 8 cells were analyzed in each condition) (D) Scatter plot of CCP intensity (in log scale) vs. number of FPR spots. Each dot in the plot represents a CCP with its x-axis representing its intensity and y-axis the number of FPR spots nearby (where we define nearby as the distance within a 10-pixel radius); the size of the dot represents the average intensity of all the FPR spots nearby. Only occupied CCPs were included in these two plots. (Occupied CCP number: $n_{w/o\ fMLP} = 315$, $n_{fMLP} = 1270$)

nm) radius of a CCP. There were 17.32% of CCPs without FPRs nearby (vacant CCPs) for the control condition compared to 10.62% for the fMLP-treated condition (Figure 4.1C). In addition, there were significantly more CCPs with FPRs (occupied CCPs) in the FMLP-treated condition. We next ask whether the increased number of CCPs and FPRs are scattered randomly on the membrane with uniformly distributed intensity and how many FPR puncta are around a CCP. To provide a more comprehensive view of the data, we mapped each individual CCP to a plane where x-axis is the CCP intensity and y-axis the number of FPR puncta surrounding it with the marker size indicating the FPR intensity (Figure 4.1D and E). From the two scatter plots, it is apparent that the plot for non-stimulation is not a down-sample version of the plot for fMLP-stimulated condition. Rather, the two conditions had different distributions in three variables presented. In the presence of fMLP, the increase in CCP numbers was not uniform against CCP intensity - there were much more dimmer structures than the brighter ones. Interestingly, it is the dimmer CCP structures where we found more surrounding FPR puncta as well as more FPRs (i.e. larger circles). While the increase in dimmer structures could due to a greater z distance from the imaging plane, fMLP treatment increases neutrophil spreading and should provide an overall greater attachment to the substrate. The increase in FPR in dimmer CCPs is similar to a finding reported recently that short-lived (i.e. dim CCPs) have more epidermal growth factor receptors (EGFR) (*Rosselli-Murai et al.*, 2017). This is also consistent with cargo clustering that nucleate de novo CCPs. Altogether, the above results demonstrated that fMLP stimulation led to interaction between FPR and CCPs and thus CME is responsive to fMLP stimulation in neutrophils.

4.3.2 fMLP internalization occurs rapidly in neutrophil

To further study endocytosis during neutrophil polarization, we next sought to characterize the kinetics of fMLP internalization. An early study quantified the endo-

cytosis rate in polymorphonuclear leukocytes using fluorescein-dextran and observed a steady increase in intensity over time (*Davis et al.*, 1986). We used FITC labeled fMLP to track internalization of fMLP over time using flow cytometry analysis (see Methods and figure captions for more details). Similar to canonical transferrin uptake assay to quantify the endocytic rate (*Liu et al.*, 2010), we measured the intensity of FITC-fMLP following surface bound ligand removal. Due to the incomplete differentiation of some cells, we observed two populations in FITC channel (Figure 4.2). The peak intensities for two contiguous time points only had small differences. In this case, using a simple mean or median or any manually picked metrics would fail to quantify the data objectively. Hence, we resorted to a Gaussian mixture model to model the two populations by assuming that the data came from two Gaussian distributions and extracted the larger mean as the "average intensity" for that sample. The method has several advantages in this application:

1. It utilized all the acquired data without manually excluding any data;

2. It was able to differentiate the difference between conditions;

3. It was robust across all independent experiments.

We observed a canonical endocytic uptake trend for the uptake of fMLP within the first 20 minutes (Figure 4.3). It is worth noting that the rate of increase is not uniform in the first 20 min. The rate of increase between 0 min to 2 min was much more distinct than any other time range (1.43 ± 0.069 a.u./min), and followed by 5 min to 10 min (0.0237 ± 0.0118 a.u./min). In contrast to previous reported results, we observed a drop in intensity at 30 min, following robust internalization at earlier time points. One possible reason is that ligands undergo complex endocytic pathways, along which the ligand-receptors get recycled back to the membrane or degraded within the cells.

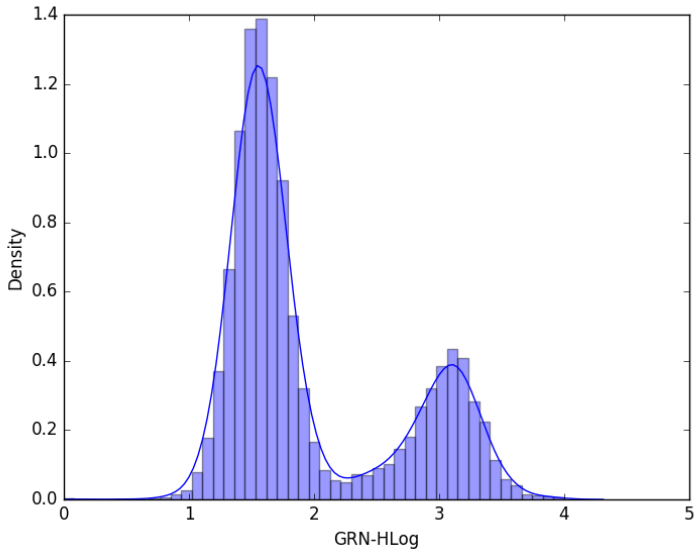

Figure 4.2: Density plot for FITC channel. The larger the GRN-HLog value, the more fMLP-FITC was taken in. Due to the incomplete differentiation of HL-60 cells, we observed two intensity peaks. The peak values were extracted using Gaussian mixture models.

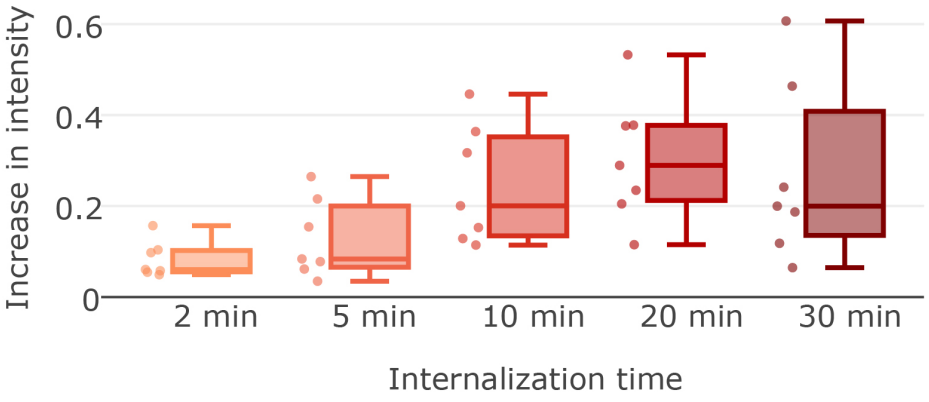

Figure 4.3: fMLP internalization first increases over time but then decreases. fMLP internalization at 2 min, 5 min, 10 min, 20 min, and 30 min time points were measured by flow cytometry (See Materials and Methods for detailed calculation of average intensity). Each data point for a specific condition in the box plot represents the difference in average intensity between that condition and the control condition (without internalization) from a single experiment. A total of 7 independent experiments were performed.

4.3.3 CME is important for neutrophil polarization

The association of FPR with CCPs and internalization of fMLP bound FPR following fMLP stimulation suggest that CME might play a role in neutrophil polarization. Many studies have pointed to the crucial and multi-faceted roles of CME on signaling (*Rosselli-Murai et al.*, 2017; *Liu et al.*, 2017; *Reis et al.*, 2015; *Garay et al.*, 2015; *Weinberg et al.*, 2017). Clathrins role as a scaffold but not in receptor endocytosis is required for Akt308 phosphorylation upon epidermal growth factor stimulation(*Rosselli-Murai et al.*, 2017; *Garay et al.*, 2015). In an analogous way, *Eichel et al.* (2016) revealed that clathrin-coated structures on the plasma membrane are central for β-arrestin signaling of GPCRs. Conversely, proper CME is important for other signaling pathways, including ERK and mTORC1 signaling (*Rosselli-Murai et al.*, 2017). The importance of endocytosis for downstream signaling has also been found in growth factor signaling to mTORC1 in macrophages (*Garay et al.*, 2015).

To investigate whether CME is essential in neutrophil polarization, we resorted to pharmaceutical perturbations, which acutely and effectively target cell population and do not suffer from compensation in genetic knockdown experiments. We performed experiments with two of the mostly used inhibitors for CME, Pitstop2 (that interferes with CCP assembly (*von Kleist et al.*, 2011)) and Dynasore (that inhibits vesicle scission (*Macia et al.*, 2006)). Although there are reports that show Pitstop2 blocks clathrin-independent endocytosis and the drug has non-specific effects (*Dutta et al.*, 2012; *Willox et al.*, 2014), we are not concluding anything about the function of clathrins N-terminal domain. In order to evaluate the effects of endocytosis inhibitors on neutrophil polarization in an objective manner, we used automated imaging and analysis of fixed cells labeling microtubule, actin, phospho-myosin II (pMyosinII) and DAPI (Figure 4.4A). In fMLP-treated cells, actin and microtubule/pMyosinII distinctively localized to the front and rear of a cell, respectively. As it is readily apparent, addition of Pitstop2 and Dynasore abrogated fMLP-induced polarization.

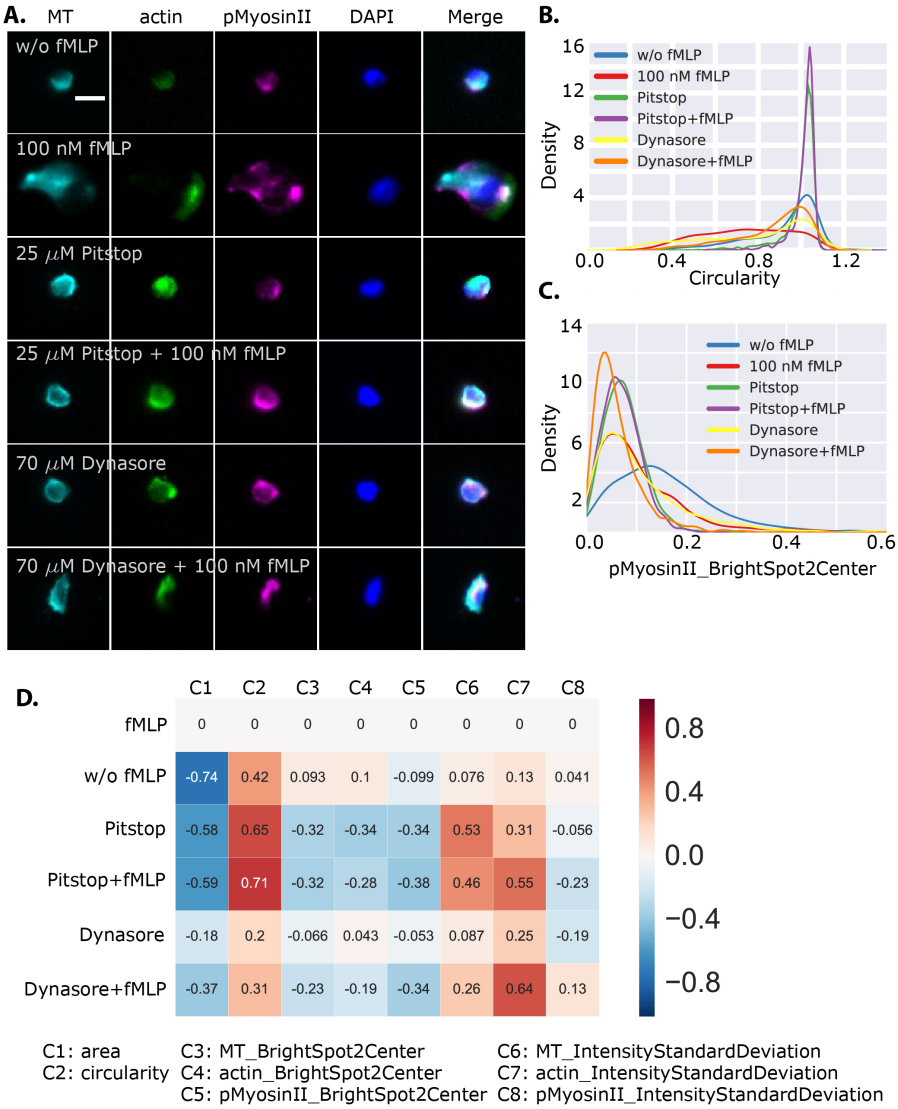

Figure 4.4: Pitstop and dynasore, two drugs that perturb clathrin-mediated endocytosis, inhibit neutrophil polarization. (A) Representative fluorescent images (cyan: microtubule, green: actin, magenta: pMyosinII, blue: DAPI) of neutrophils under different treatment. (B)-(C) Kernel density estimation for circularity and relative distance between bright spot of pMyosinII to cell center distributions across different conditions. These are two example distributions from 8 extracted features. (D) Kolmogorov-Smirnov test statistics between 100 nM fMLP condition and the rest of the conditions. Intuitively, positive value indicates that the distribution for the feature shit to right compared to fMLP condition (e.g., circularity distribution in Figure 4.4B); negative value indicates a shift to left (e.g., pMyosinII_BrightSpot2Center in Figure 4.4C). (Cell number: $n_{\text{w/o fMLP}} = 1358$, $n_{\text{fMLP}} = 764$, $n_{\text{Pitstop}} = 1423$, $n_{\text{Pitstop+fMLP}} = 894$, $n_{\text{Dynasore}} = 1572$, $n_{\text{Dynasore+fMLP}} = 1421$)

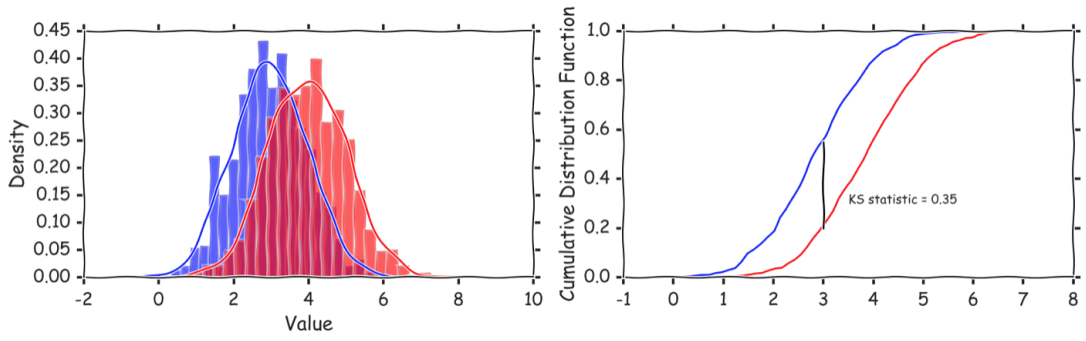

Figure 4.5: Explanation of Kolmogorov-Smirnov (KS) test statistics. The data in blue has a smaller mean than data in red. This can be reflected in the accumulative distribution function shown on right, where blue curve is above the red one. If we define blue data as the reference, then we will get a positive KS statistics.

To avoid possible selection bias and to further understand the phenotype change, we analyzed about 1000 cells for each condition and extracted three groups of features from the images: morphology (C1 and C2), center (C3-C5), and intensity (C6-C8). Due to the large number of cells imaged, we need a more compressed way to represent the feature for each condition. In high-throughput screening studies for selecting hits, z-score method, B-score method, strictly standardized mean difference, and quantile-based methods are used as a way to summarize thousands of measurements into a single number17. As illustrated in Figure 4.4B and C, the measurements are not all drawn from a normal distribution; therefore, we adopted Kolmogorov-Smirnov (KS) test statistics to summarize distributions (more details can be found in Figure 4.5). Using the fMLP stimulation condition as the base, a negative KS statistics (in blue) would mean that the distribution of the measurement shifts to the left compared to fMLP-stimulated cells, and therefore is on average smaller. On the other hand, a positive KS statistics (in red) would mean that the distribution shifts to the right, and therefore is on average larger (Figure 4.4D).

It is well known HL60-differentiated neutrophils are smaller and rounder com-

pared to when stimulated with fMLP. Thus, KS statistics was negative for cell area but positive for circularity (circularity = 1 when it is a perfect circle). This is an assuring proof of principle for our analysis. Using this analysis, we observed the same pattern for both Pitstop2 and Dynasore-treated cells with and without fMLP. However, Dynasore-treated cells had less negative KS statistics for cell area, indicating that Pitstop2 had a larger effect on morphological phenotype.

Besides morphological features, we further measured center and intensity features, denoted as bright to center and intensity deviation, that characterized the spatial organization for microtubules, actin and pMyosinII (Figure 4.4D). Center feature for a structure calculates the normalized distance (by the cell diameter) between the center of an area with 95% of total intensity pixels within a cell and the centroid of all the pixels within a cell. This feature characterizes how polarized a structure is. If the 95% brightest pixels all concentrate in a small region along the cell edge, then center feature is large. On the contrary, if the brightest pixels are close to the center or around the cell periphery, then the value would be small. For cells without fMLP, we only observed a marginal difference in center features compared to cells stimulated with fMLP. For Pitstop2 and Dynasore-treated fMLP stimulated cells, center features were on average smaller, suggesting that Pitstop2 and Dynasore impaired distribution of actin, microtubule, and pMyosinII. Intensity deviation calculates the standard deviation in fluorescence intensity within a cell. A small value means a narrower distribution of the intensity, whereas a large value means intensities within a cell are more spread out. Interestingly, for microtubule and actin, our analysis indicated a larger standard deviation but a smaller bright to center distance for cells without fMLP and for cells treated with Pitstop2 or Dynasore with or without fMLP. From the fluorescence images, we could see bright band of actin and microtubule at the end of a cell in Pitstop2 and Dynasore-treated cells, which explains the large variance, but the distance to the center is not as large compared to the cells treated with fMLP.

Taken above, perturbation of CME by Pitstop2 and Dynasore caused disruption of neutrophil polarization. Even though we cannot rule out off target effects of these small molecules on the cells (*Willox et al.*, 2014; *Girard et al.*, 2011), the finding that both small molecule inhibitors targeting endocytosis abrogated HL60 polarization strongly suggest that CME plays a crucial role in neutrophil polarization.

4.3.4 Inhibition of CME blocks several signaling pathways

Since Pitstop2 and Dynasore both potently blocked fMLP-induced neutrophil polarization, we hypothesize that these inhibitors also block cell signaling. To investigate the downstream signaling effectors of CME, we compared $pAKT_{308}$, $pAKT_{473}$ and pERK levels without and with Pitstop/Dynasore in fMLP stimulated cells. $pAKT_{308}$, $pAKT_{473}$ and pERK covered three major signaling pathway. Specifically, $pAKT_{308}$ indicates the activities of protein kinase Akt, which mediates the positive feedback loop between PIP3 and actin (*Weiner et al.*, 2002), $pAKT_{473}$ were used as a readout of PIP3 and mTORC2 activity, and pERK is activated in MAPK/ERK pathway that is frequently associated with the -arrestin signaling pathway. Using Western blot analysis, we measured the phosphorylation of pERK (Figure 4.6A and B), $pAKT_{473}$ (Figure 4.6C and D), and $pAKT_{308}$ (Figure 4.6E and F) at various time points between 0 min to 10 min and observed a rapid stimulation which reaches its peak within 1-2 minutes and gradually decreases. However, all these dynamical changes disappeared when cells were treated with Pitstop2. Pitstop2 blocks CME at the early stage but not the binding of fMLP to FPR. Hence, we could speculate that proper assembly of CCPs is a crucial step in effective signal transduction. It is interesting to note that Dynasore's impact on neutrophil polarization was not as dramatic as that of Pitstop2 (Figure 4.4D). Here, our signaling analysis showed that the peak intensities of $pAKT_{308}$, $pAKT_{473}$, and pERK of cells in the presence of Dynasore were about half compared to untreated cells, which might explain the intermediate phe-

notype of Dynasore-treated cells. Even though Dynasore-treated cells also reached maximum signaling between 1 and 2 minutes, the subsequent decline of signaling was less efficient. From these results, we believe that CME inhibition hindered neutrophil polarization by blocking fMLP-induced signaling.

4.3.5 Polarized neutrophils have denser and dimmer CCPs at the front

The differences between fMLP stimulation and the two small molecule inhibition conditions provide some clues on the role of CME during neutrophil polarization. Signal transduction likely occurs concurrently during CCP formation, invagination, and scission to form CCV. More importantly, the events after CCP scission (where max signaling is 1-2 minutes) may also aid in neutrophil polarization (on the order of 5 minutes). To gain deeper insights on the relationship of clathrin machinery and signaling scaffold with neutrophil polarization, we investigated in detail the spatial organization between actin, the prominent structure that marks polarity, and clathrin or β-arrestin, the structural and signaling scaffolds in CME, respectively.

As shown in Figure 4.4, neutrophil polarization is marked by the non-uniform cellular components, such as actin, microtubule, and pMyosinII. There have been a number of inconsistent reports on the spatial distribution of CCPs in polarized cells. In 1982, *Davis et al.* (1982) observed that CCPs were mainly located at the back of polarized neutrophils via transmission electron microscopy. However, *Rappoport and Simon* (2003) reported that majority of CCPs were at the leading edge of a migrating cell. We believe that these incongruent findings may lie in the methods used to observed CCP. From our own experiments, CCPs appear to preferentially localize at the front end of the cells by TIR-FM where the ventral plasma membrane is visualized. On the other hand, CCPs appear to be in the middle or at the back of the cell when using confocal or epi-fluorescence microscopy (*Rappoport and Simon*, 2003; *Samaniego et al.*, 2007). Here we use TIR-FM for better signal-to-background

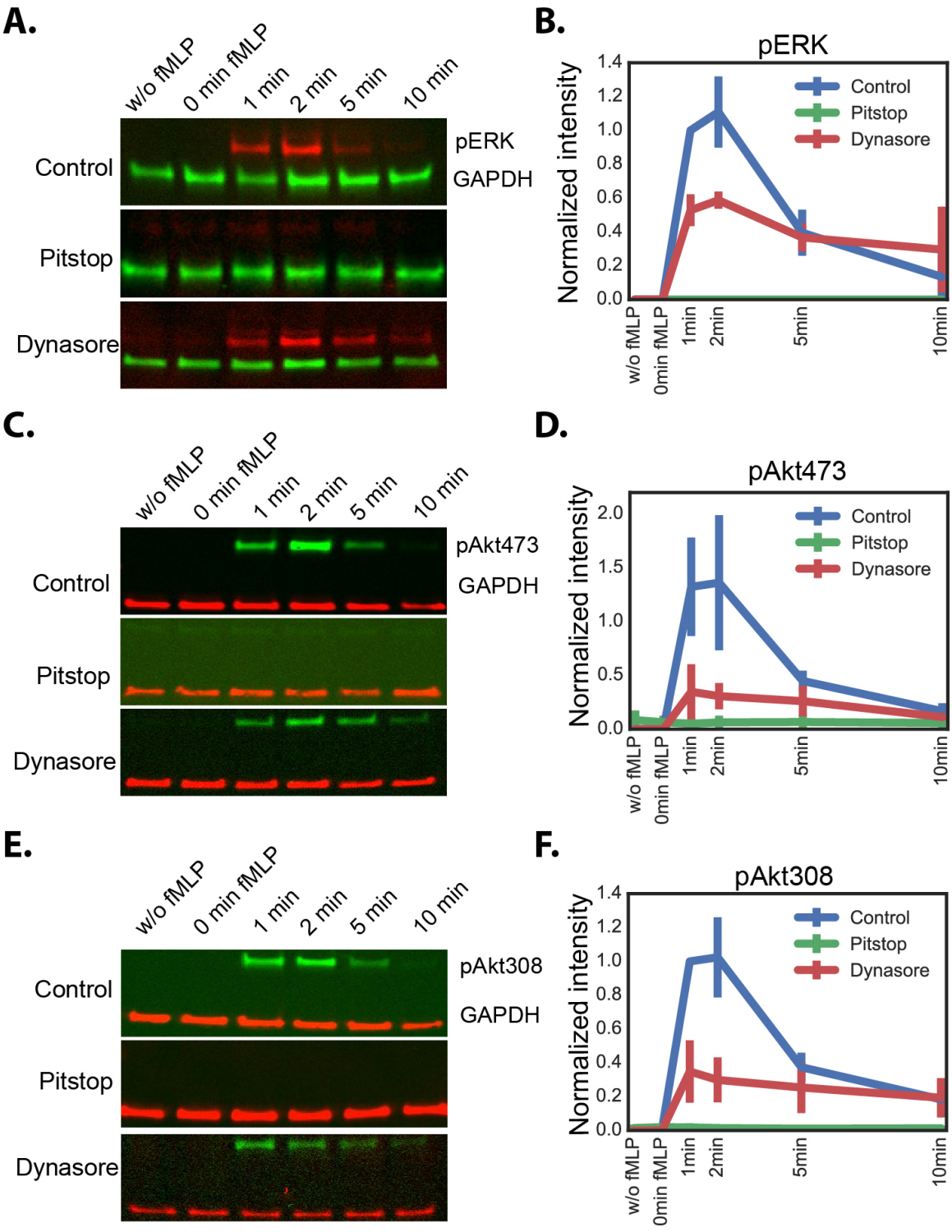

Figure 4.6: Inhibition of CME blocks several signaling pathways. Changes of pERK (A, B) $pAkt_{473}$ (C, D), and $pAkt_{308}$ (E,F) were quantified by Western blot analysis with and without fMLP over time with and without Pitstop and Dynasore. Data in B, D, and F represented mean ± s.d. from three independent experiments.

ratio and more accurate CCP localization.

Consistent with previous studies, we also observed polarization in CCP localization. Without fMLP, CCPs were more evenly distributed on the membrane, whereas there was a distinct CCP band well correlated with the lamellipodia in polarized cells (Figure 4.7). As we and others have shown22, fMLP stimulation leads to rapid polymerization of actin filaments, as evidenced by an increase in phalloidin-stained actin intensity (Figure 4.7B and C). We observed the same trend for CCPs (Figure 4.7D and E). There were about 5 times more CCPs and a right shift of intensity distribution in fMLP-stimulated cells, with a slightly higher density. In Figure 4.1D and E, we noted that there appeared to be more dimmer CCPs in the presence of fMLP. Here, indeed we see the CCP intensity distribution is left skewed with a long tail. However, compared to the cells without fMLP, the CCP median intensity was still higher.

With more and brighter CCPs in the presence of fMLP, how were they distributed on the cell membrane? From the microscopy images, we observed that near the actin bright area, CCPs also seemed to be denser. To quantify this observation, we calculated the local CCP density and actin intensity for each CCP by drawing a circle centered at it. For actin intensity, we chose a small radius of 5 pixels (290 nm) to reflect local density. For CCP density, we selected a larger radius of 40 pixels (2.33 µm) to capture its spatial organization. We also calculated the average intensity for all the CCPs within the circle. Therefore, for each point in Figure 4.7F and G, it represents an individual CCP and shows its local CCP density, actin intensity, and the average CCP intensity (indicated by the size of the point). Comparing the cells without fMLP (Figure 4.7F) and with fMLP (Figure 4.7G), we saw a striking difference in CCP distribution and their correlation to actin intensity. Without fMLP, there were two distinct populations of CCPs, a larger one with low actin intensity and low CCP density and a second population with higher actin intensity and larger CCP

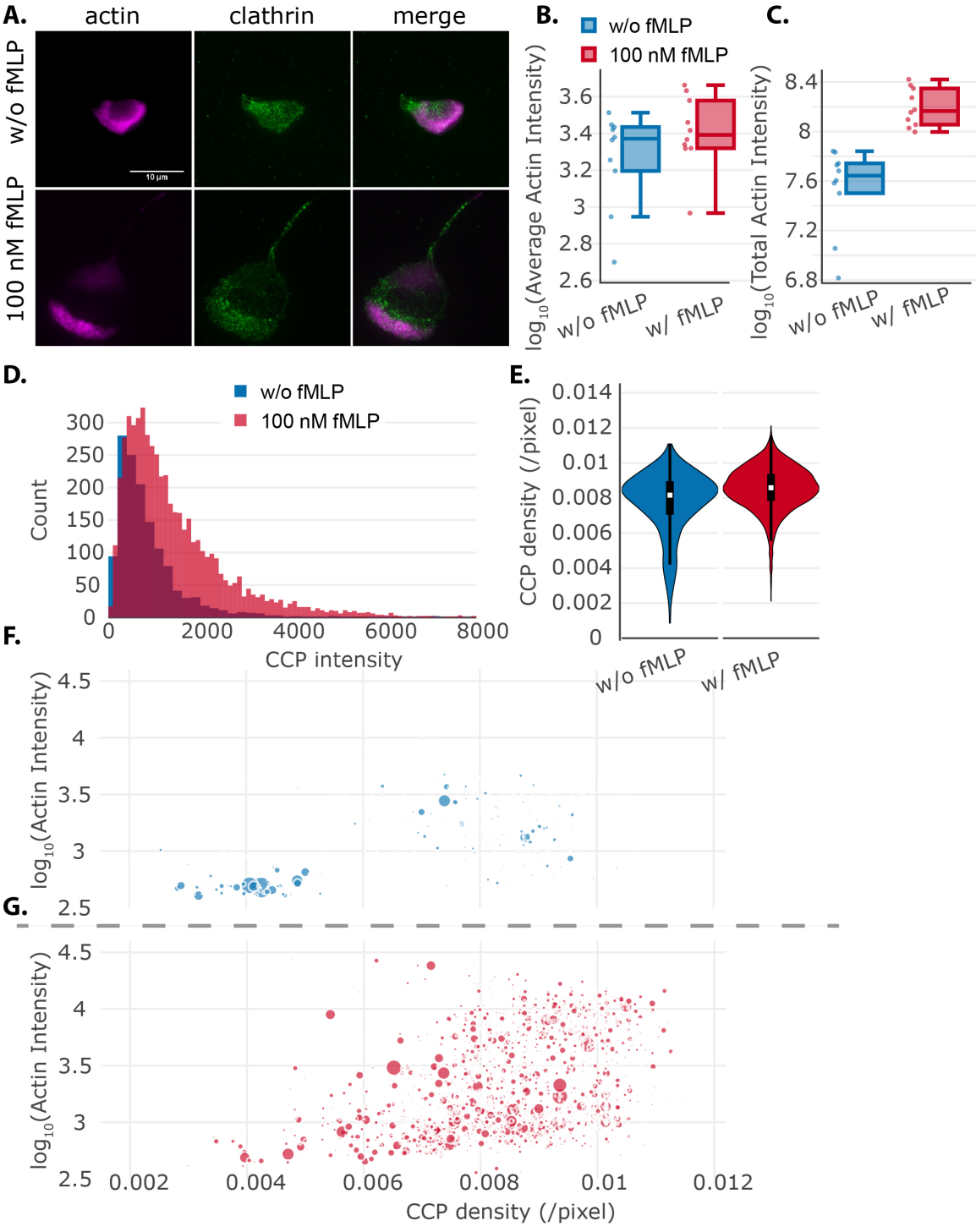

Figure 4.7: Caption on the next page

Figure 4.7: There is a dramatic increase in CCP numbers and intensity in the presence fMLP. (A) Representative TIRF images of actin (magenta) and CCPs (green) without (upper) and with (bottom) 100 nM fMLP. (B)-(C) Boxplot of average actin intensity and total actin intensity across the whole cell. Each dot represents an individual cell. p* = 0.29, Wilcoxon rank-sum test for average actin intensity. p** = 0.00015, Wilcoxon rank-sum test for total actin intensity. ($n_{w/o\ fMLP} = 10$, $n_{100\ nM\ fMLP} = 10$) (D) Histogram of CCP intensities with and without fMLP. The data were from the same cells as the ones in which actin intensities were measured. p 0, Kolmogorov-Smirnov test. ($n_{w/o\ fMLP} = 1361$, $n_{100\ nM\ fMLP} = 5364$) (E) Violin plot of CCP densities with and without fMLP. $p < 10^{-26}$, Kolmogorov-Smirnov test. (F)-(G) Scatter plot of CCP density vs. local actin intensity (in log scale). Each dot in the plot denotes an individual CCP with x-axis representing CCP density and y-axis is the local actin intensity. CCP density in a radius of 40 pixels and local actin intensity radius of 5 pixels were used in this analysis.

density. This separation completely disappeared with fMLP stimulation. However, we observed that most CCPs resided at the lower triangle of the plane, which means that when actin intensity was low, CCP density was not constrained. At high actin intensity areas, CCP density scaled up as well. Interestingly, at the top right part of the plane, where actin and CCP densities were both high, CCP intensities on average were dimmer. This result is consistent with our finding in Figure 1 where dimmer CCPs had more FPRs. The result also agrees with our recent finding that small and short-lived CCPs are capable of signaling (*Rosselli-Murai et al.*, 2017). Together, our analysis provides clear evidence that fMLP stimulation promotes nucleation and suggests the endocytic machineries signal to actin polymerization in neutrophil polarization. The observation of smaller CCPs is consistent with previous finding that cells with high tension have smaller CCPs (*Irajizad et al.*, 2017; *Tan et al.*, 2015) and we expect the leading edge of the cell to have higher membrane tension(*Lieber et al.*, 2015). Previous work has demonstrated that receptor clustering can promote CCP nucleation (*Liu et al.*, 2010). Ligand binding and receptor clustering is a cellular mechanism to control receptor signaling (*Bray et al.*, 1998), so it is plausible that the dim CCPs represent de novo nucleated CCPs upon FPR clustering.

4.3.6 There is a dramatic increase in the number and intensity of β-arrestins in polarized neutrophils

We speculate the endocytic machineries have to signal to actin assembly during neutrophil polarization so there should be a spatial relationship between signaling scaffold proteins and actin structures. Our signaling experiments showed CME played an important role in ERK phosphorylation and it has been shown that pERK reinforces actin polymerization at the leading edge during motility (*Mendoza et al.*, 2015). G protein-independent ERK activation is has been shown to be dependent on β-arrestin (*Shenoy et al.*, 2006) . Recent work has also shown that FPR signaling is mediated by β-arrestin1. Based on these reasons, we investigated the spatial relationship between β-arrestin, acting as a scaffold intermediates for GPCR signaling, and actin structures.

We observed a more distinct difference in β-arrestin immunofluorescence between fMLP stimulation and no stimulation compared to clathrin. Without fMLP, β-arrestin only formed dim punctate structures, but in the presence of fMLP, punctate structures were much more discernible and distributed all over the cell membrane (Figure 4.8A). The β-arrestin structures were not only brighter, but the distribution also appeared denser. Following the same analysis as described earlier, the β-arrestin intensity histogram and density distribution were in agreement with this observation (Figure 4.8B and C).

To better quantify the spatial organization of β-arrestin, we mapped each detected β-arrestin to local actin intensity and β-arrestin density space, with the marker size representing the -arrestin intensity (Figure 4.8D and E). The plot revealed a different pattern for β-arrestin than clathrin. Like clathrin distribution, we find high β-arrestin density at high actin intensity, although there is a range of β-arrestin density. However, at regions with high actin intensity with fMLP stimulation (i.e. top right corner of the plot), we found more and brighter β-arrestin structures (recall clathrin was

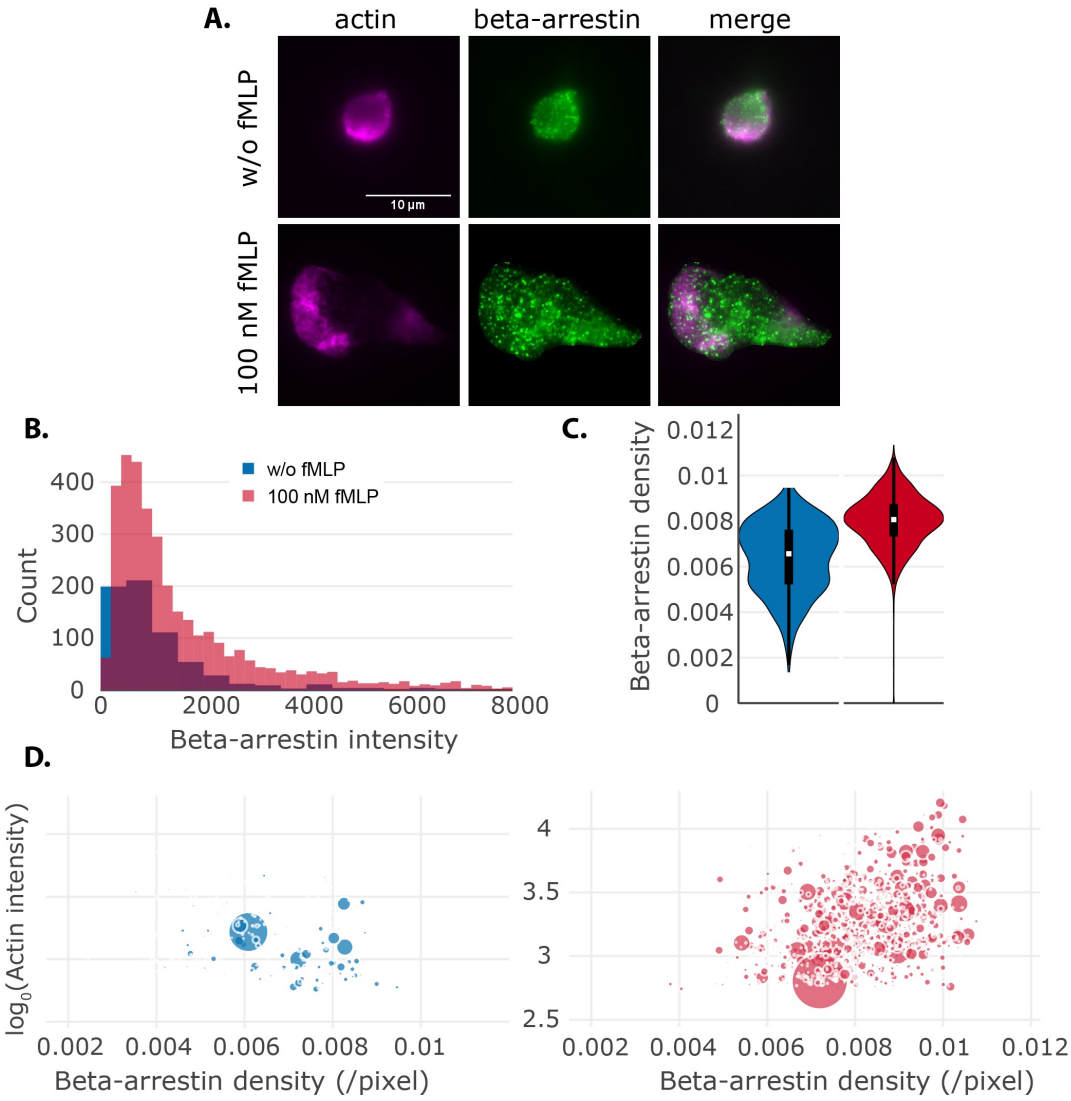

Figure 4.8: Caption on the next page

Figure 4.8: fMLP greatly increases the number of β-arrestin on the membrane. (A) Representative TIRF images of actin (magenta) and -arrestin (green) without (upper) and with (bottom) 100 nM fMLP. (B) Histogram of β-arrestin intensities with and without fMLP. $p < 10^{-11}$, Kolmogorov-Smirnov test. (Cell number: $n_{w/o\ fMLP}$=8, $n_{100\ nM\ fMLP} = 10$; β-arrestin number: $n_{w/o\ fMLP}$=659, $n_{100\ nM\ fMLP} = 3540$) (C) Violin plot of β-arrestin densities with and without fMLP. p 0, Kolmogorov-Smirnov test. (D)-(E) Scatter plot of -arrestin density vs. local actin intensity (in log scale). Each dot in the plot denotes an individual β-arrestin with x-axis representing β-arrestin density and y-axis the local actin intensity. β-arrestin density based on radius of 40 pixels and local actin intensity radius of 5 pixels were used in this analysis.

dimmer in this region). The difference between clathrin and β-arrestin distribution may reflect the functional and temporal disparities of the two molecules. Clathrin recycles between polymerization and uncoating during the formation of CCVs whereas β-arrestin needs to sustain signaling to actin polymerization during polarization and motility.

4.3.7 Regulation of neutrophil polarization by CME

By applying quantitative approaches, our studies have revealed a tight connection between endocytosis of FPR receptor, signaling of fMLP-FPR, and functional polarization of neutrophils (Figure 4.9). Assembly of CCPs and internalization of CCVs are critical for cell signaling and we believe that the ability to organize a variety of molecules into its functional unit is one reason that CME is important in many physiological processes (*Scita and Di Fiore*, 2010). As discrete macromolecular assemblies, CCPs can organize cell signaling with spatiotemporal precision. A theoretical study has predicted that polarity requires optimal endocytosis and can be dynamically stabilized through positive feedback with directed transport (*Marco et al.*, 2007). In this regard, cell polarization has been described as a bistable process with competition for actin between myosin II-dependent contractility and dendritic actin polymerization (*Lomakin et al.*, 2015) that allows for retrograde transport of myosin II. Our work shows the critical role CME plays in signaling to actin polymerization, without which

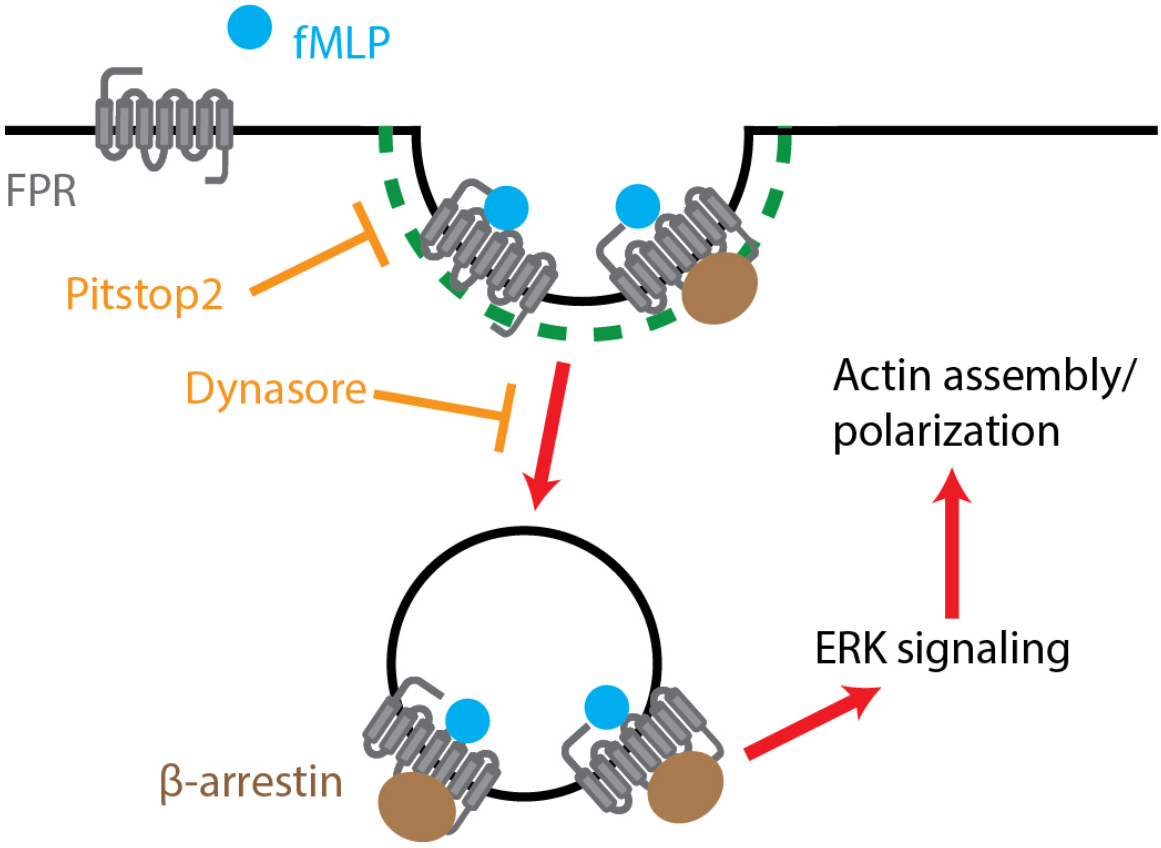

Figure 4.9: Model summarizing the role of CME of fMLP receptor in mediating neutrophil polarization. Spatially localized internalization of fMLP receptor is important for signaling to the actin cytoskeleton during neutrophil polarization.

polarization would be blocked. As receptor clustering and CCP initiation can be tuned depending on chemical and mechanical microenvironment, a cell would be able to rapidly make migration decisions during chemotaxis by integrating information from CCPs.

CHAPTER V

Conclusion and Future Work

5.1 Summary

In summary, we have studied how CCPs respond to spatial confinements via μ-contact printing, and during neutrophil polarization, stimulated by chemoattractant fMLP. In both cases, we have observed a non-homogeneous distribution of CCPs and their properties. These findings show that the seemingly random CCPs are regulated locally by anisotrophic cues. Here is a synposis of our findings.

In Chapter II, we used μ-contact printing to control the spreading of cells and thus the cortical tension, and found that larger cells had higher tension and altered CCP dynamics. We observed a sligntly increased proportion of abortive CCPs and higher initiation density, and a lower CCP intensity which indicated smaller CCP. Using a low dose of latrunculin A and Y-27632 compound, even though we did not see the decrease in abortive CCPs or initiation density, we indeed observed a higher CCP intensity. This means that lifetime and initiation density in these spreading cells are not regulated by actin-related mechanisms, but the difference we observed in CCP intensity or size is strongly related to cortical tension.

In cell biology, to prove a causal-effect relationship, we often start by disrupting the mechanism and then observe the effects. Over the years, we have developed many tools to disrupt a mechanism, over-expression of a mutated protein, genetic knock-

down approaches such as siRNA and shRNA, targeted drugs such as latrunculin A and Y-27632 compound, or even CRISPR/Cas9 system for a 100% knockout. However, all these methods have one type or another side effects. To completely isolate one factor out is almost impossible. We would have to resort to bottom-up approaches for a cleaner system.

Using a minimal system, which reconstitutes CCPs on giant unilamellar vesicles with AP180, clathrin, and epsin, *Saleem et al.* found that high tension by osmotic shock inhibits clathrin polymerization. This study is in agreement with ours. Several other studies (*Irajizad et al.*, 2017; *Hassinger et al.*, 2017), from computational perspectives, also showed that with it is harder to form deep invaginated clathrin coat with high membrane tension.

In Chapter III, using μ-contact printing, we studied how anisotropic cues and adhesion proteins can affect CCP dynamics. The results indicated that CCP distribution is less regulated by the overall morphology of the cells, but rather the local cues, for final spreading area and shape do not determine where and how long does a CCP appear. The engineering system allowed us to know that the lifetime and intiation of CCPs are actively regulated. Due to the lack of chemical stimuli, we conjecture that actin network and the downstream effectors of actin network play a role in regulating CCP dynamics here.

From the above two projects, we see that μ-contact printing is a powerful experimental system that allows us to precisely manipulate cell morphology and thus the underlying cytoskelton. It has been shown previously that cell geometry could not only alter actin structure but also have profound effects on cell fate. However, in CCP dynamics, it is less clear what the physiological relevance of different endocytic dynamics is. It would be more insightful if we identify the direct regulator of CCP lifetime and initiation density. In this way, we could have a more systematic picture of how CME, actin cytoskeleton, and cell geometry connect to each other.

My last project was aimed to uncover some physiological relevance of endocytic regulation on a cellular process, here focusing on neutrophil polarization. Neutrophil is marked by their fast response to chemoattractant. In the presence of chemoattractant, within 5 - 10 min, neutrophils rapidly establish anisotropic morphology, polarized cellular structuress, and move toward to chemoattractant. It seems like a perfect system to connnect biochemical stimuli to mechanical response. Indeed, the system has been well studied, and there exists accumulated experimental evidence and established computational models for neutrophil chemotaxis. However, there were not so much study from a CME perspective.

We quantified the spatial organization of FPR and CCP. Upon the stimulation of fMLP, there were indeed more occupied CCPs and most of the CCPs had less intensities. We further measured the endocytic activity upon adding fMLP and observed a increased uptake of fMLP. Given these, we hypothesized that CME might play a role in neutrophil polarization. Ineed, when we inhibited CME using Pitstop and Dynasore, we observed a disrupted polarization, which might be caused by the inhibition of major signaling pathways. Lastly, we observed the differential spatial correlation of CCP or β-arrestin density and actin without and with fMLP.

As discussed in Chapter I, there are many ways that CME could be a part of signaling pathway. The evidences that CME plays an role in neutrophil polarization is strong, but we do not yet know the dots in between. Possible hypotheses are: 1) some CME-related protein acts as a important scaffold or signal transducer during neutrophil polarization; 2) recycling and sorting through endocytic pathway are important. Our drug inhibition assays seem to support both. Dynasore, which inhibits CCP invagination, did not block the signaling pathway completely and the disruption of neutrophil polarization was less severe. However, Pitstop, which inhibits the formation of CCPs, completely blocked all major signaling pathway and the neutrophil polarization. In spite of the potential off-target effects, two eassays together could at

least lend support to the hypotheses.

5.2 Future Work

The thesis explored regularity in the seemingly random behaviors of CCPs. However, we also recognize the weaknesses of the study. Therefore, we proposed the following future work for deeper understanding of neutrophil polarization.

Given the complexity of CME, we think systems biology approaches would be able to clarify the role of CME in neutrophil polarization. One such approach is to sequentially knockdown the major components of CME and measure the effects on neutrophil polarization. Inefficient as this approach seems, it might also lead to novel findings. However, one technical difficulty for us is to efficiently knockdown a protein in HL-60 cell line. Another limitation is that for an important protein like clathrin, a cell will need to adapt to the knockdown; therefore, the phenotype we observed might not accurately reflect the abscence of that protein. This limitation is the reason for small molecule inhibition advocates. However, drugs always have off-target effects, and we do not have drugs specific for all proteins. Given this dilemma, we think the best way is to perform multiple types of experiments. If the phenotype sustains across all these different methods, then we would have more confidence of the mechanism we hypothesize.

The major step is to build shRNA library for major endocytic proteins and validate the shRNA transfection on neutrophils. Once this important preparation step is finished, we will utilize the computational approaches we developed in IV and compared the features in the perturbed cells with controlled group. Knowing the perturbation and the phenotype change, we can draw a correlation between the corresponding protein and the specific phenotype change. Careful analysis of perturbed phenotype in polarization can help us find new mechanisms that regulate polarization. Also, we will compare neutrophil polarization phenotype from shRNA knockdown to one from Pit-

stop and Dynasore treatments. Furthermore, To better understand the role of CME in the dynamics of neutrophil polarization, we can analyze neutrophil polarization process by live-cell imaging and computational image analysis, and probe temporal responses of Akt and Erk for endocytic-protein-knockdown cells. If we identify any endocytic protein target that greatly regulate neutrophil polarization, we then can utilize bioinformatic search to find molecular links between two processes.

In summary, we have accumulated many facts and knowledge about cell biology, but sometimes it is a challenge for an individual to know all the different domains. For example, CME and neutrophil polarization, experts in each field have studied very deep in that field but they might be ignorant of the other. Bioinformatics search, such as the BioGRID platform (*Stark et al.*, 2006), might help us to find links between two different domains and thus save us from an exhaustive search. We envision that computation-aided experimental research could go a long way and provides a more systems understanding of CME.

APPENDICES

APPENDIX A

K-means Algorithm

In Chapter III, to segment the protein patterns, we used k-means algorithm. K-means algorithm is used in data mining applications to automatically assign data points to k clusters. Here, the algorithm aims to find a intensity threshold that separates the pattern and background.

Given $(x_1, x_2, \cdots, x_n)$ as observed data. Here in our case, x_i is the intensity for a pixel. We want to minimize the in-class distances, i.e.,

$$\arg\min \sum_{k=1}^{K} \sum_{x \in S_i} ||x - \mu_i||^2$$

where μ_i is the mean point for cluster S_i.

However, there is no closed form solution to the problem. We resort to iterative and heuristic method. The procedure is described as following:

1. Randomly initiate K clusters' center $\mu_1, \cdots, \mu_K$

2. For each data point x, assign its cluster:

$$\hat{i} = \arg\min_i ||x - \mu_i||$$

3. Recalculate the new cluster mean: $\mu_i = \frac{\sum_{x_j \in S_i} x_j}{|S_i|}$ for $i = 1, 2, \cdots, K$

4. Repeat Step 2 and 3 until convergence

Image segmentation is a useful tool in cell image analysis. The simplest method is to set any intensity above a threshold as foreground. With k-means algorithm, we can more objectively calculate the threshold. It is extremely helpful in the applications where the intensity level might not be constant across all images.

APPENDIX B

Gaussian Mixture Algorithm

In Chapter IV, we used Gaussian mixture models to find the mean intensity for the second peak of the flow cytometry data. Similar to k-means algorithm, Gaussian mixture is also a clustering algorithm, but instead of hard assignment on clusters, it assigns each data point a probability share of all clusters.

Our data again is one-dimensional data; each data point represents the uptake intensity of a cell. Based on the histogram, we supposed that the measurements come from Gaussian mixture with two Gaussian components, i.e.,

$$p(x) = \sum_{i=1}^{2} w_i \mathcal{N}(x; \mu_i, \sigma_i)$$

where $\sum_{i=1}^{2} w_i = 1$ and $\mathcal{N}(x; \mu_i, \sigma_i) = \frac{1}{\sqrt{2\pi\sigma_i^2}} e^{-\frac{(x-\mu_i)^2}{2\sigma_i^2}}$

Our goal is to find w_i, μ_i, σ_i from the data. We want to maximize the log-likelihood for all observed data, i.e.,

$$\arg\max_{w,\mu,\sigma} \sum_{i=1}^{N} \log \sum_{k=1}^{2} w_k \mathcal{N}(x_i; \mu_k, \sigma_k)$$

We rely on expectation-maximization to solve this problem. Define a state variable

associated with each data point, $\mathbf{s} = (s_1, s_2, \cdots, s_N)$ and indicator variable $\Delta_{i,k} = \begin{cases} 1 & s_i = k \\ 0 & otherwise \end{cases}$. Similar to k-means, it iteratively performs two steps:

1. Given w, μ, σ, update $\bar{\mathbf{s}}$

2. Given $\bar{\mathbf{s}}$, update w, μ, σ

In Step 1, we calculate the repsonsibility of cluster $1, \cdots, K$ on each data point (at j iteration):

$$\gamma_{i,k}^{(j)} = \frac{w_k^{(j)} \mathcal{N}(x_i; \mu_k^{(j)}, \sigma_k^{(j)})}{\sum_{l=1}^{2} w_l^{(j)} \mathcal{N}(x_i; \mu_l^{(j)}, \sigma_l^{(j)})}$$

In Step 2, we use maximum likelihood estimation to calculate w, μ, σ:

$$\mu_l^{(j+1)} = \frac{\sum_{i=1}^{N} \gamma_{i,l}^{(j)} x_i}{\sum_{i=1}^{N} \gamma_{i,l}^{(j)}}$$

$$\sigma_l^{(j+1)} = \frac{\sum_{i=1}^{N} \gamma_{i,l}^{(j)} (x_i - \mu_l^{(j+1)})^2}{\sum_{i=1}^{N} \gamma_{i,l}^{(j)}}$$

Again, this method automatically detects the peak of the intensity data, specially useful for the experimental data where the difference between groups is very subtle.

BIBLIOGRAPHY

BIBLIOGRAPHY

Aghamohammadazadeh, S., and K. R. Ayscough (2009), Under pressure: the differential requirements for actin during yeast and mammalian endocytosis, *Nature cell biology*, *11*(8), 1039.

Aguet, F., C. N. Antonescu, M. Mettlen, S. L. Schmid, and G. Danuser (2013), Advances in analysis of low signal-to-noise images link dynamin and ap2 to the functions of an endocytic checkpoint, *Developmental cell*, *26*(3), 279–291.

Amessou, M., et al. (2016), Spatio-temporal regulation of egfr signaling by the eps15 homology domain-containing protein 3 (ehd3), *Oncotarget*, *7*(48), 79,203.

Antonescu, C. N., F. Aguet, G. Danuser, and S. L. Schmid (2011), Phosphatidylinositol-(4, 5)-bisphosphate regulates clathrin-coated pit initiation, stabilization, and size, *Molecular biology of the cell*, *22*(14), 2588–2600.

Barlic, J., et al. (2000), Regulation of tyrosine kinase activation and granule release through β-arrestin by cxcr1, *Nature immunology*, *1*(3), 227–233.

Borner, G. H., M. Harbour, S. Hester, K. S. Lilley, and M. S. Robinson (2006), Comparative proteomics of clathrin-coated vesicles, *J Cell Biol*, *175*(4), 571–578.

Boulant, S., C. Kural, J.-C. Zeeh, F. Ubelmann, and T. Kirchhausen (2011), Actin dynamics counteract membrane tension during clathrin-mediated endocytosis, *Nature cell biology*, *13*(9), 1124.

Bray, D., M. D. Levin, and C. J. Morton-Firth (1998), Receptor clustering as a cellular mechanism to control sensitivity, *Nature*, *393*(6680), 85.

Carbone, R., S. Fré, G. Iannolo, F. Belleudi, P. Mancini, P. G. Pelicci, M. R. Torrisi, and P. P. Di Fiore (1997), eps15 and eps15r are essential components of the endocytic pathway, *Cancer research*, *57*(24), 5498–5504.

Chen, C. S., M. Mrksich, S. Huang, G. M. Whitesides, and D. E. Ingber (1997), Geometric control of cell life and death, *Science*, *276*(5317), 1425–1428.

Chen, C. S., J. L. Alonso, E. Ostuni, G. M. Whitesides, and D. E. Ingber (2003), Cell shape provides global control of focal adhesion assembly, *Biochemical and biophysical research communications*, *307*(2), 355–361.

Chen, P.-H., et al. (2012a), Identification of a novel function of the clathrin-coated structure at the plasma membrane in facilitating gm-csf receptor-mediated activation of jak2, *Cell Cycle*, *11*(19), 3611–3626.

Chen, W., R. H. Lam, and J. Fu (2012b), Photolithographic surface micromachining of polydimethylsiloxane (pdms), *Lab on a Chip*, *12*(2), 391–395.

Cocucci, E., F. Aguet, S. Boulant, and T. Kirchhausen (2012), The first five seconds in the life of a clathrin-coated pit, *Cell*, *150*(3), 495–507.

Cocucci, E., R. Gaudin, and T. Kirchhausen (2014), Dynamin recruitment and membrane scission at the neck of a clathrin-coated pit, *Molecular biology of the cell*, *25*(22), 3595–3609.

Conner, S. D., and S. L. Schmid (2003), Regulated portals of entry into the cell, *Nature*, *422*(6927), 37.

Corey, D. P., J. García-Añoveros, J. R. Holt, K. Y. Kwan, et al. (2004), Trpa1 is a candidate for the mechanosensitive transduction channel of vertebrate hair cells, *Nature*, *432*(7018), 723.

Davis, B., R. Walter, C. Pearson, E. Becker, and J. Oliver (1982), Membrane activity and topography of f-met-leu-phe-treated polymorphonuclear leukocytes. acute and sustained responses to chemotactic peptide., *The American journal of pathology*, *108*(2), 206.

Davis, B. H., E. McCabe, and M. Langweiler (1986), Characterization of f-met-leu-phe-stimulated fluid pinocytosis in human polymorphonuclear leukocytes by flow cytometry, *Cytometry Part A*, *7*(3), 251–262.

Di Paolo, G., and P. De Camilli (2006), Phosphoinositides in cell regulation and membrane dynamics, *Nature*, *443*(7112), 651–657.

Doherty, G. J., and H. T. McMahon (2009), Mechanisms of endocytosis, *Annual review of biochemistry*, *78*, 857–902.

Dupont, S., et al. (2011), Role of yap/taz in mechanotransduction, *Nature*, *474*(7350), 179.

Dutta, D., C. D. Williamson, N. B. Cole, and J. G. Donaldson (2012), Pitstop 2 is a potent inhibitor of clathrin-independent endocytosis, *PloS one*, *7*(9), e45,799.

Ehrlich, M., W. Boll, A. Van Oijen, R. Hariharan, K. Chandran, M. L. Nibert, and T. Kirchhausen (2004), Endocytosis by random initiation and stabilization of clathrin-coated pits, *Cell*, *118*(5), 591–605.

Eichel, K., D. Jullié, and M. Von Zastrow (2016), [beta]-arrestin drives map kinase signalling from clathrin-coated structures after gpcr dissociation, *Nature cell biology*, *18*(3), 303–310.

Engler, A. J., S. Sen, H. L. Sweeney, and D. E. Discher (2006), Matrix elasticity directs stem cell lineage specification, *Cell*, *126*(4), 677–689.

Ernst, S., N. Zobiack, K. Boecker, V. Gerke, and U. Rescher (2004), Agonist-induced trafficking of the low-affinity formyl peptide receptor fprl1, *Cellular and molecular life sciences*, *61*(13), 1684–1692.

Etienne-Manneville, S., and A. Hall (2002), Rho gtpases in cell biology, *Nature*, *420*(6916), 629–635.

Eyckmans, J., T. Boudou, X. Yu, and C. S. Chen (2011), A hitchhiker's guide to mechanobiology, *Developmental cell*, *21*(1), 35–47.

Ferguson, J. P., N. M. Willy, S. P. Heidotting, S. D. Huber, M. J. Webber, and C. Kural (2016), Deciphering dynamics of clathrin-mediated endocytosis in a living organism, *J Cell Biol*, pp. jcb–201604,128.

Ferguson, S. S., W. E. Downey III, A.-M. Colapietro, L. S. Barak, L. Ménard, and M. G. Caron (1996), Role of,-arrestin in mediating agonist-promoted g protein-coupled receptor, *Science*, *271*, 363.

Fogelson, B., and A. Mogilner (2014), Computational estimates of membrane flow and tension gradient in motile cells, *PLoS One*, *9*(1), e84,524.

Gaidarov, I., F. Santini, R. A. Warren, and J. H. Keen (1999), Spatial control of coated-pit dynamics in living cells, *Nature cell biology*, *1*(1), 1–7.

Garay, C., G. Judge, S. Lucarelli, S. Bautista, R. Pandey, T. Singh, and C. N. Antonescu (2015), Epidermal growth factor–stimulated akt phosphorylation requires clathrin or erbb2 but not receptor endocytosis, *Molecular biology of the cell*, *26*(19), 3504–3519.

Gauthier, N. C., M. A. Fardin, P. Roca-Cusachs, and M. P. Sheetz (2011), Temporary increase in plasma membrane tension coordinates the activation of exocytosis and contraction during cell spreading, *Proceedings of the National Academy of Sciences*, *108*(35), 14,467–14,472.

Gauthier, N. C., T. A. Masters, and M. P. Sheetz (2012), Mechanical feedback between membrane tension and dynamics, *Trends in cell biology*, *22*(10), 527–535.

Girard, E., J. L. Paul, N. Fournier, P. Beaune, L. Johannes, C. Lamaze, and B. Védie (2011), The dynamin chemical inhibitor dynasore impairs cholesterol trafficking and sterol-sensitive genes transcription in human hela cells and macrophages, *PloS one*, *6*(12), e29,042.

Goodman, O. B., J. G. Krupnick, F. Santini, V. V. Gurevich, R. B. Penn, A. W. Gagnon, J. H. Keen, and J. L. Benovic (1996), β-arrestin acts as a clathrin adaptor in endocytosis of the β2-adrenergic receptor, *nature*, *383*(6599), 447–450.

Gov, N. S., and A. Gopinathan (2006), Dynamics of membranes driven by actin polymerization, *Biophysical journal*, *90*(2), 454–469.

Grassart, A., et al. (2014), Actin and dynamin2 dynamics and interplay during clathrin-mediated endocytosis, *J Cell Biol*, pp. jcb–201403,041.

Grove, J., D. J. Metcalf, A. E. Knight, S. T. Wavre-Shapton, T. Sun, E. D. Protonotarios, L. D. Griffin, J. Lippincott-Schwartz, and M. Marsh (2014), Flat clathrin lattices: stable features of the plasma membrane, *Molecular biology of the cell*, *25*(22), 3581–3594.

Hassinger, J. E., G. Oster, D. G. Drubin, and P. Rangamani (2017), Design principles for robust vesiculation in clathrin-mediated endocytosis, *Proceedings of the National Academy of Sciences*, *114*(7), E1118–E1127.

Hayakawa, K., H. Tatsumi, and M. Sokabe (2012), Mechano-sensing by actin filaments and focal adhesion proteins, *Communicative & integrative biology*, *5*(6), 572–577.

Henne, W. M., E. Boucrot, M. Meinecke, E. Evergren, Y. Vallis, R. Mittal, and H. T. McMahon (2010), Fcho proteins are nucleators of clathrin-mediated endocytosis, *Science*, *328*(5983), 1281–1284.

Hind, L. E., W. J. Vincent, and A. Huttenlocher (2016), Leading from the back: the role of the uropod in neutrophil polarization and migration, *Developmental cell*, *38*(2), 161–169.

Hochmuth, R. M. (2000), Micropipette aspiration of living cells, *Journal of biomechanics*, *33*(1), 15–22.

Houk, A. R., A. Jilkine, C. O. Mejean, R. Boltyanskiy, E. R. Dufresne, S. B. Angenent, S. J. Altschuler, L. F. Wu, and O. D. Weiner (2012), Membrane tension maintains cell polarity by confining signals to the leading edge during neutrophil migration, *Cell*, *148*(1), 175–188.

Huang, F., A. Khvorova, W. Marshall, and A. Sorkin (2004), Analysis of clathrin-mediated endocytosis of epidermal growth factor receptor by rna interference, *Journal of Biological Chemistry*, *279*(16), 16,657–16,661.

Iijima, M., and P. Devreotes (2002), Tumor suppressor pten mediates sensing of chemoattractant gradients, *Cell*, *109*(5), 599–610.

Iijima, M., Y. E. Huang, and P. Devreotes (2002), Temporal and spatial regulation of chemotaxis, *Developmental cell*, *3*(4), 469–478.

Ingber, D. E. (2006), Cellular mechanotransduction: putting all the pieces together again, *The FASEB journal*, *20*(7), 811–827.

Irajizad, E., N. Walani, S. L. Veatch, A. P. Liu, and A. Agrawal (2017), Clathrin polymerization exhibits high mechano-geometric sensitivity, *Soft Matter*, *13*(7), 1455–1462.

Iskratsch, T., H. Wolfenson, and M. P. Sheetz (2014), Appreciating force and shape [mdash] the rise of mechanotransduction in cell biology, *Nature Reviews Molecular Cell Biology*, *15*(12), 825–833.

Jaqaman, K., D. Loerke, M. Mettlen, H. Kuwata, S. Grinstein, S. L. Schmid, and G. Danuser (2008), Robust single-particle tracking in live-cell time-lapse sequences, *Nature methods*, *5*(8), 695–702.

Jean-Alphonse, F., and A. Hanyaloglu (2011), Regulation of gpcr signal networks via membrane trafficking, *Molecular and cellular endocrinology*, *331*(2), 205–214.

Johnson, G. L., and R. Lapadat (2002), Mitogen-activated protein kinase pathways mediated by erk, jnk, and p38 protein kinases, *Science*, *298*(5600), 1911–1912.

Jose, M., S. Tollis, D. Nair, J.-B. Sibarita, and D. McCusker (2013), Robust polarity establishment occurs via an endocytosis-based cortical corralling mechanism, *J Cell Biol*, pp. jcb–201206,081.

Kaksonen, M., C. P. Toret, and D. G. Drubin (2005), A modular design for the clathrin-and actin-mediated endocytosis machinery, *Cell*, *123*(2), 305–320.

Kam, L., W. Shain, J. Turner, and R. Bizios (2001), Axonal outgrowth of hippocampal neurons on micro-scale networks of polylysine-conjugated laminin, *Biomaterials*, *22*(10), 1049–1054.

Kaur, S., A. B. Fielding, G. Gassner, N. J. Carter, and S. J. Royle (2014), An unmet actin requirement explains the mitotic inhibition of clathrin-mediated endocytosis, *Elife*, *3*, e00,829.

Kim, D.-H., P. K. Wong, J. Park, A. Levchenko, and Y. Sun (2009), Microengineered platforms for cell mechanobiology, *Annual review of biomedical engineering*, *11*, 203–233.

Kita, A., et al. (2011), Microenvironmental geometry guides platelet adhesion and spreading: a quantitative analysis at the single cell level, *PloS one*, *6*(10), e26,437.

Kural, C., A. A. Akatay, R. Gaudin, B.-C. Chen, W. R. Legant, E. Betzig, and T. Kirchhausen (2015), Asymmetric formation of coated pits on dorsal and ventral surfaces at the leading edges of motile cells and on protrusions of immobile cells, *Molecular biology of the cell*, *26*(11), 2044–2053.

Lakadamyali, M., M. J. Rust, and X. Zhuang (2006), Ligands for clathrin-mediated endocytosis are differentially sorted into distinct populations of early endosomes, *Cell*, *124*(5), 997–1009.

Lefkowitz, R. J. (1993), G proteincoupled receptor kinases, *Cell*, *74*(3), 409–412.

Leyton-Puig, D., T. Isogai, E. Argenzio, B. van den Broek, J. Klarenbeek, H. Janssen, K. Jalink, and M. Innocenti (2017), Flat clathrin lattices are dynamic actin-controlled hubs for clathrin-mediated endocytosis and signalling of specific receptors, *Nature Communications*, *8*, ncomms16,068.

Lieber, A. D., S. Yehudai-Resheff, E. L. Barnhart, J. A. Theriot, and K. Keren (2013), Membrane tension in rapidly moving cells is determined by cytoskeletal forces, *Current Biology*, *23*(15), 1409–1417.

Lieber, A. D., Y. Schweitzer, M. M. Kozlov, and K. Keren (2015), Front-to-rear membrane tension gradient in rapidly moving cells, *Biophysical journal*, *108*(7), 1599–1603.

Liu, A. P., D. Loerke, S. L. Schmid, and G. Danuser (2009), Global and local regulation of clathrin-coated pit dynamics detected on patterned substrates, *Biophysical journal*, *97*(4), 1038–1047.

Liu, A. P., F. Aguet, G. Danuser, and S. L. Schmid (2010), Local clustering of transferrin receptors promotes clathrin-coated pit initiation, *The Journal of cell biology*, *191*(7), 1381–1393.

Liu, A. P., R. J. Botelho, and C. N. Antonescu (2017), The big and intricate dreams of little organselles: Embracing complexity in the study of membrane traffic, *Traffic*.

Loerke, D., M. Mettlen, D. Yarar, K. Jaqaman, H. Jaqaman, G. Danuser, and S. L. Schmid (2009), Cargo and dynamin regulate clathrin-coated pit maturation, *PLoS biology*, *7*(3), e1000,057.

Lohse, M., S. Andexinger, J. Pitcher, S. Trukawinski, J. Codina, J. Faure, M. G. Caron, and R. Lefkowitz (1992), Receptor-specific desensitization with purified proteins. kinase dependence and receptor specificity of beta-arrestin and arrestin in the beta 2-adrenergic receptor and rhodopsin systems., *Journal of Biological Chemistry*, *267*(12), 8558–8564.

Lomakin, A. J., K.-C. Lee, S. J. Han, D. A. Bui, M. Davidson, A. Mogilner, and G. Danuser (2015), Competition of two distinct actin networks for actin defines a bistable switch for cell polarization, *Nature cell biology*, *17*(11), 1435.

Luo, T., K. Mohan, P. A. Iglesias, and D. N. Robinson (2013), Molecular mechanisms of cellular mechanosensing, *Nature materials*, *12*(11), 1064.

Luttrell, L., et al. (1999), β-arrestin-dependent formation of β2 adrenergic receptor-src protein kinase complexes, *Science*, *283*(5402), 655–661.

Luttrell, L. M., and R. J. Lefkowitz (2002), The role of β-arrestins in the termination and transduction of g-protein-coupled receptor signals, *Journal of cell science*, *115*(3), 455–465.

Macia, E., M. Ehrlich, R. Massol, E. Boucrot, C. Brunner, and T. Kirchhausen (2006), Dynasore, a cell-permeable inhibitor of dynamin, *Developmental cell*, *10*(6), 839–850.

Mammoto, T., A. Mammoto, and D. E. Ingber (2013), Mechanobiology and developmental control, *Annual review of cell and developmental biology*, *29*, 27–61.

Marco, E., R. Wedlich-Soldner, R. Li, S. J. Altschuler, and L. F. Wu (2007), Endocytosis optimizes the dynamic localization of membrane proteins that regulate cortical polarity, *Cell*, *129*(2), 411–422.

Martin, G. S. (2001), The hunting of the src, *Nature reviews Molecular cell biology*, *2*(6), 467–475.

Mato, J. M., A. Losada, V. Nanjundiah, and T. M. Konijn (1975), Signal input for a chemotactic response in the cellular slime mold dictyostelium discoideum, *Proceedings of the National Academy of Sciences*, *72*(12), 4991–4993.

McBeath, R., D. M. Pirone, C. M. Nelson, K. Bhadriraju, and C. S. Chen (2004), Cell shape, cytoskeletal tension, and rhoa regulate stem cell lineage commitment, *Developmental cell*, *6*(4), 483–495.

McMahon, H. T., and E. Boucrot (2011), Molecular mechanism and physiological functions of clathrin-mediated endocytosis, *Nature reviews Molecular cell biology*, *12*(8), 517–533.

Mendoza, M. C., M. Vilela, J. E. Juarez, J. Blenis, and G. Danuser (2015), Erk reinforces actin polymerization to power persistent edge protrusion during motility, *Science signaling*, *8*(377), ra47.

Mettlen, M., D. Loerke, D. Yarar, G. Danuser, and S. L. Schmid (2010), Cargo-and adaptor-specific mechanisms regulate clathrin-mediated endocytosis, *The Journal of cell biology*, pp. jcb–200908,078.

Miller, W. E., S. Maudsley, S. Ahn, K. D. Khan, L. M. Luttrell, and R. J. Lefkowitz (2000), β-arrestin1 interacts with the catalytic domain of the tyrosine kinase c-src role of β-arrestin1-dependent targeting of c-src in receptor endocytosis, *Journal of Biological Chemistry*, *275*(15), 11,312–11,319.

Mitsunari, T., F. Nakatsu, N. Shioda, P. E. Love, A. Grinberg, J. S. Bonifacino, and H. Ohno (2005), Clathrin adaptor ap-2 is essential for early embryonal development, *Molecular and cellular biology*, *25*(21), 9318–9323.

Nunez, D., C. Antonescu, M. Mettlen, A. Liu, S. L. Schmid, D. Loerke, and G. Danuser (2011), Hotspots organize clathrin-mediated endocytosis by efficient recruitment and retention of nucleating resources, *Traffic*, *12*(12), 1868–1878.

Oliva, A. A., C. D. James, C. E. Kingman, H. G. Craighead, and G. A. Banker (2003), Patterning axonal guidance molecules using a novel strategy for microcontact printing, *Neurochemical research*, *28*(11), 1639–1648.

Pálfy, M., A. Reményi, and T. Korcsmáros (2012), Endosomal crosstalk: meeting points for signaling pathways, *Trends in cell biology*, *22*(9), 447–456.

Provenzano, P. P., and P. J. Keely (2011), Mechanical signaling through the cytoskeleton regulates cell proliferation by coordinated focal adhesion and rho gtpase signaling, *J Cell Sci*, *124*(8), 1195–1205.

Puthenveedu, M. A., and M. von Zastrow (2006), Cargo regulates clathrin-coated pit dynamics, *Cell*, *127*(1), 113–124.

Rappoport, J. Z., and S. M. Simon (2003), Real-time analysis of clathrin-mediated endocytosis during cell migration, *Journal of cell science*, *116*(5), 847–855.

Reis, C. R., P.-H. Chen, S. Srinivasan, F. Aguet, M. Mettlen, and S. L. Schmid (2015), Crosstalk between akt/gsk3β signaling and dynamin-1 regulates clathrin-mediated endocytosis, *The EMBO journal*, p. e201591518.

Ridley, A. J., and A. Hall (1992), The small gtp-binding protein rho regulates the assembly of focal adhesions and actin stress fibers in response to growth factors, *Cell*, *70*(3), 389–399.

Rosselli-Murai, L. K., et al. (2017), Loss of pten promotes formation of signaling-specific clathrin-coated pits, *bioRxiv*, p. 137760.

Roybal, K. T., et al. (2016), Computational spatiotemporal analysis identifies wave2 and cofilin as joint regulators of costimulation-mediated t cell actin dynamics., *Science signaling*, *9*(424), rs3–rs3.

Saffarian, S., E. Cocucci, and T. Kirchhausen (2009), Distinct dynamics of endocytic clathrin-coated pits and coated plaques, *PLoS biology*, *7*(9), e1000,191.

Salbreux, G., G. Charras, and E. Paluch (2012), Actin cortex mechanics and cellular morphogenesis, *Trends in cell biology*, *22*(10), 536–545.

Saleem, M., S. Morlot, A. Hohendahl, J. Manzi, M. Lenz, and A. Roux (), A balance between membrane elasticity and polymerization energy sets the shape of spherical clathrin coats, *Nature communications*, *6*.

Samaniego, R., L. Sánchez-Martín, A. Estecha, and P. Sánchez-Mateos (2007), Rho/rock and myosin ii control the polarized distribution of endocytic clathrin structures at the uropod of moving t lymphocytes, *Journal of cell science*, *120*(20), 3534–3543.

Scita, G., and P. P. Di Fiore (2010), The endocytic matrix, *Nature*, *463*(7280), 464.

Shao, Y., X. Tan, R. Novitski, M. Muqaddam, P. List, L. Williamson, J. Fu, and A. P. Liu (2013), Uniaxial cell stretching device for live-cell imaging of mechanosensitive cellular functions, *Review of Scientific Instruments*, *84*(11), 114,304.

Shao, Y., J. M. Mann, W. Chen, and J. Fu (2014), Global architecture of the f-actin cytoskeleton regulates cell shape-dependent endothelial mechanotransduction, *Integrative Biology*, *6*(3), 300–311.

Shenoy, S. K., et al. (2006), β-arrestin-dependent, g protein-independent erk1/2 activation by the β2 adrenergic receptor, *Journal of Biological Chemistry*, *281*(2), 1261–1273.

Sigismund, S., E. Argenzio, D. Tosoni, E. Cavallaro, S. Polo, and P. P. Di Fiore (2008), Clathrin-mediated internalization is essential for sustained egfr signaling but dispensable for degradation, *Developmental cell*, *15*(2), 209–219.

Sinha, B., et al. (2011), Cells respond to mechanical stress by rapid disassembly of caveolae, *Cell*, *144*(3), 402–413.

Sorkin, A., and M. von Zastrow (2002), Signal transduction and endocytosis: close encounters of many kinds, *Nature reviews. Molecular cell biology*, *3*(8), 600.

Stachowiak, J. C., F. M. Brodsky, and E. A. Miller (2013), A cost-benefit analysis of the physical mechanisms of membrane curvature, *Nature cell biology*, *15*(9).

Stark, C., B.-J. Breitkreutz, T. Reguly, L. Boucher, A. Breitkreutz, and M. Tyers (2006), Biogrid: a general repository for interaction datasets, *Nucleic acids research*, *34*(suppl_1), D535–D539.

Stricker, J., T. Falzone, and M. L. Gardel (2010), Mechanics of the f-actin cytoskeleton, *Journal of biomechanics*, *43*(1), 9–14.

Swaney, K. F., C.-H. Huang, and P. N. Devreotes (2010), Eukaryotic chemotaxis: a network of signaling pathways controls motility, directional sensing, and polarity, *Annual review of biophysics*, *39*, 265–289.

Tan, J. L., J. Tien, D. M. Pirone, D. S. Gray, K. Bhadriraju, and C. S. Chen (2003), Cells lying on a bed of microneedles: an approach to isolate mechanical force, *Proceedings of the National Academy of Sciences*, *100*(4), 1484–1489.

Tan, X., J. Heureaux, and A. P. Liu (2015), Cell spreading area regulates clathrin-coated pit dynamics on micropatterned substrate, *Integrative Biology*, *7*(9), 1033–1043.

Taylor, M. J., D. Perrais, and C. J. Merrifield (2011), A high precision survey of the molecular dynamics of mammalian clathrin-mediated endocytosis, *PLoS biology*, *9*(3), e1000,604.

Taylor, M. J., M. Lampe, and C. J. Merrifield (2012), A feedback loop between dynamin and actin recruitment during clathrin-mediated endocytosis, *PLoS biology*, *10*(4), e1001,302.

Théry, M., V. Racine, M. Piel, A. Pépin, A. Dimitrov, Y. Chen, J.-B. Sibarita, and M. Bornens (2006), Anisotropy of cell adhesive microenvironment governs cell internal organization and orientation of polarity, *Proceedings of the National Academy of Sciences*, *103*(52), 19,771–19,776.

Vedula, S., A. Ravasio, E. Anon, T. Chen, G. Peyret, M. Ashraf, and B. Ladoux (2014), Microfabricated environments to study collective cell behaviors., *Methods in cell biology*, *120*, 235–252.

von Kleist, L., et al. (2011), Role of the clathrin terminal domain in regulating coated pit dynamics revealed by small molecule inhibition, *Cell*, *146*(3), 471–484.

Voskuhl, J., J. Brinkmann, and P. Jonkheijm (2014), Advances in contact printing technologies of carbohydrate, peptide and protein arrays, *Current opinion in chemical biology*, *18*, 1–7.

Wagener, B. M., N. A. Marjon, and E. R. Prossnitz (2016), Regulation of n-formyl peptide receptor signaling and trafficking by arrestin-src kinase interaction, *PloS one*, *11*(1), e0147,442.

Walani, N., J. Torres, and A. Agrawal (2015), Endocytic proteins drive vesicle growth via instability in high membrane tension environment, *Proceedings of the National Academy of Sciences*, *112*(12), E1423–E1432.

Wang, J. G., M. Miyazu, E. Matsushita, M. Sokabe, and K. Naruse (2001), Uniaxial cyclic stretch induces focal adhesion kinase (fak) tyrosine phosphorylation followed by mitogen-activated protein kinase (mapk) activation, *Biochemical and biophysical research communications*, *288*(2), 356–361.

Warren, G., J. Davoust, and A. Cockcroft (1984), Recycling of transferrin receptors in a431 cells is inhibited during mitosis., *The EMBO Journal*, *3*(10), 2217.

Weinberg, Z. Y., A. S. Zajac, T. Phan, D. J. Shiwarski, and M. A. Puthenveedu (2017), Sequence-specific regulation of endocytic lifetimes modulates arrestin-mediated signaling at the μ opioid receptor, *Molecular Pharmacology*, *91*(4), 416–427.

Weiner, O. D., P. O. Neilsen, G. D. Prestwich, M. W. Kirschner, L. C. Cantley, and H. R. Bourne (2002), A ptdlnsp3-and rho gtpase-mediated positive feedback loop regulates neutrophil polarity, *Nature cell biology*, *4*(7), 509.

Willox, A. K., Y. M. Sahraoui, and S. J. Royle (2014), Non-specificity of pitstop 2 in clathrin-mediated endocytosis, *Biology open*, *3*(5), 326–331.

Wolfe, B. L., and J. Trejo (2007), Clathrin-dependent mechanisms of g protein-coupled receptor endocytosis, *Traffic*, *8*(5), 462–470.

Yang, H. W., S. Collins, and T. Meyer (2016), Locally excitable cdc42 signals steer cells during chemotaxis, *Nature cell biology*, *18*(2), 191.

Zoncu, R., R. M. Perera, D. M. Balkin, M. Pirruccello, D. Toomre, and P. De Camilli (2009), A phosphoinositide switch controls the maturation and signaling properties of appl endosomes, *Cell*, *136*(6), 1110–1121.